Atlas and Anatomy of SPECT/CT

E. Edmund Kim, Vanessa Murad, Jin-Chul Paeng,
Hyung-Jun Im, Ji-Young Kim, and Gi-Jeong Cheon

Single-photon emission computed tomography (SPECT) imaging has evolved rapidly during the past decades since the introduction of the Anger camera in 1970, the posterior rotating gantry and dual detectors with better reconstruction processes, and quantitative data analysis. In the late 1990s, hybrid SPECT/CT imaging appeared to improve diagnostic accuracy with precise anatomical location and image quality with attenuation correction. In the last 10 years, the improvements in this equipment and the evolution in radiopharmaceuticals have allowed us to improve in the evaluation of physiological processes and in the characterization of pathologies based on morphological patterns [1]. Conventional analog technologies have advanced to multidetector devices with direct conversion digital detectors that improve efficiency, resolution and image quality, resulting in faster studies with lower doses and even the ability to image multiple radionuclides simultaneously. This includes the last generation cadmium-zinc-telluride (CZT) scanners, which bring more possibilities in research and clinical practice, especially in nuclear cardiology [2–4]. There is no denying that SPECT is still the go-to choice for most cardiologists.

There are multiple SPECT/CT applications, and in this chapter, we introduce most of them with demonstrative examples. In tumor pathology, its best-known applications are the evaluation of bone tumors, especially osteoblastic metastases, neuroendocrine tumors, and parathyroid adenomas [5, 6]. However, there are other multiple uses such as the evaluation of hepatocellular carcinoma, liver metastasis, neuroblastoma, paraganglioma, and thyroid cancer. In non-tumor bone pathology, it is indicated in trauma, degenerative disease, and infection, for example – also in the evaluation of benign thyroid pathology, gastrointestinal bleeding, lymphatic system pathology, and pulmonary physiology, among others [5, 7–9]. SPECT systems as well as radiopharmaceuticals are more available and probably cost-effective than PET, so they remain and will remain at the forefront.

E. E. Kim
Department of Radiological Sciences, University of California, Irvine, School of Medicine, Orange, CA, USA

Department of Nuclear Medicine and Department of Molecular Medicine, Graduate School of Convergence Science and Technology, Seoul National University College of Medicine, Seoul, Republic of Korea

V. Murad (✉)
Department of Nuclear Medicine, Seoul National University College of Medicine, Seoul, Republic of Korea

Department of Diagnostic Imaging, Fundacion Santa Fe de Bogotá University Hospital, Bogota, Colombia

J.-C. Paeng · G.-J. Cheon
Department of Nuclear Medicine, Seoul National University College of Medicine, Seoul, Republic of Korea

H.-J. Im
Departments of Applied Bioengineering, Molecular Medicine, and Biopharmaceutical Sciences, Graduate School of Convergence Science and Technology, Seoul National University, Seoul, Republic of Korea

J.-Y. Kim
Department of Nuclear Medicine, Bundang Seoul National University Hospital, Seoul Korea, Radiation Health Research Institute, Korea Hydro & Nuclear Power Co., Ltd., Seoul, Republic of Korea

E. E. Kim et al. (eds.), *Atlas and Anatomy of PET/MRI, PET/CT and SPECT/CT*, https://doi.org/10.1007/978-3-030-92349-5_3

1 Tumors

1.1 Hepatocellular Carcinoma

1.1.1 Case 1

A 51-year-old man with a diagnosis of hepatocellular carcinoma. Selected SPECT (*top*) and SPECT/CT (*bottom*) of the liver with ^{99m}Tc-MAA particles injected into a hepatic arterial catheter showed several focal areas of slightly to moderately increased activity in the right and left hepatic lobes corresponding to multicentric hepatoma. Only 50% of hepatomas can be imaged with FDG-PET, mainly because of the high levels of phosphatase that dephosphorylate FDG and allow it to diffuse out of cells (Fig. 1) [10].

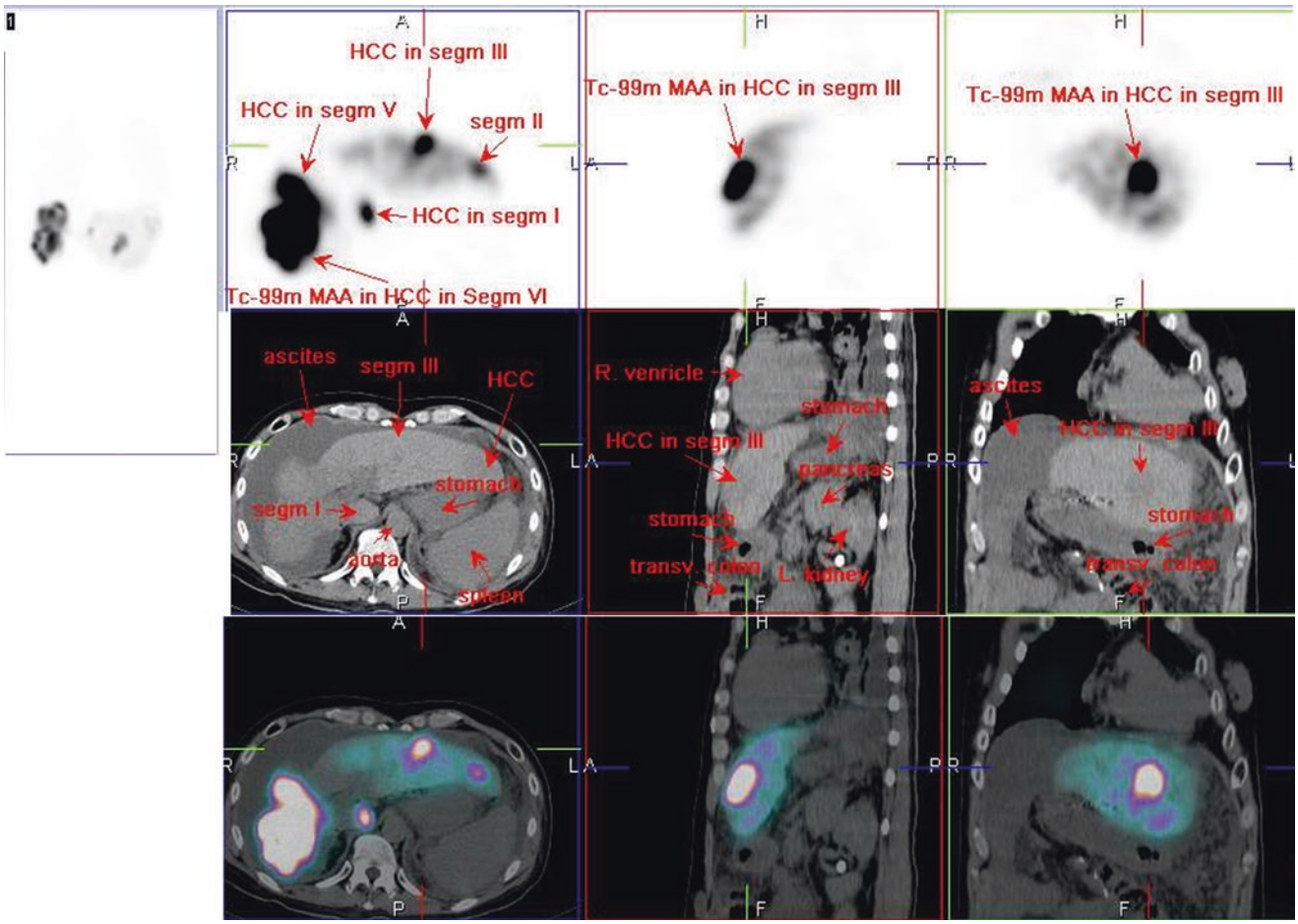

Fig. 1 ^{99m}Tc-MAA SPECT/CT

1.2 Liver Metastases

1.2.1 Case 1

A 68-year-old female patient with liver metastasis from breast cancer. Selected SPECT (*top*) and SPECT/CT (*bottom*) of the liver with ^{99m}Tc-MAA into the hepatic arterial catheter showed markedly heterogeneous activity in the liver caused by known metastases. There was no extra hepatic activity (Fig. 2) [11].

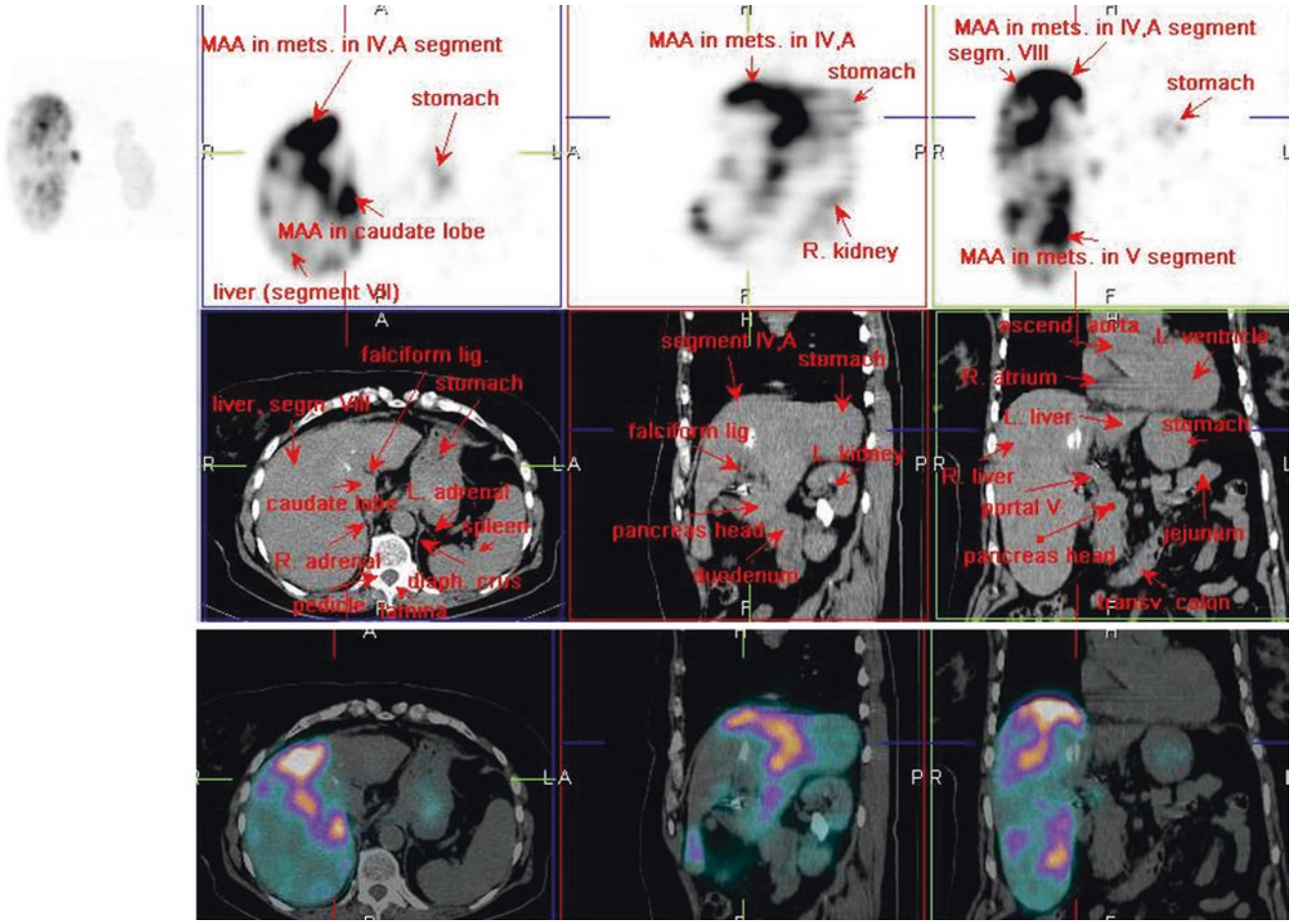

Fig. 2 ^{99m}Tc-MAA SPECT/CT

1.2.2 Case 2

Selected SPECT (*top*) and SPECT/CT (*bottom*) of the upper abdomen with ^{99m}Tc-MAA particles into a hepatic arterial catheter showed curvilinear activity along the gastric wall, indicating the suboptimal position of the hepatic arterial catheter (Fig. 3) [12].

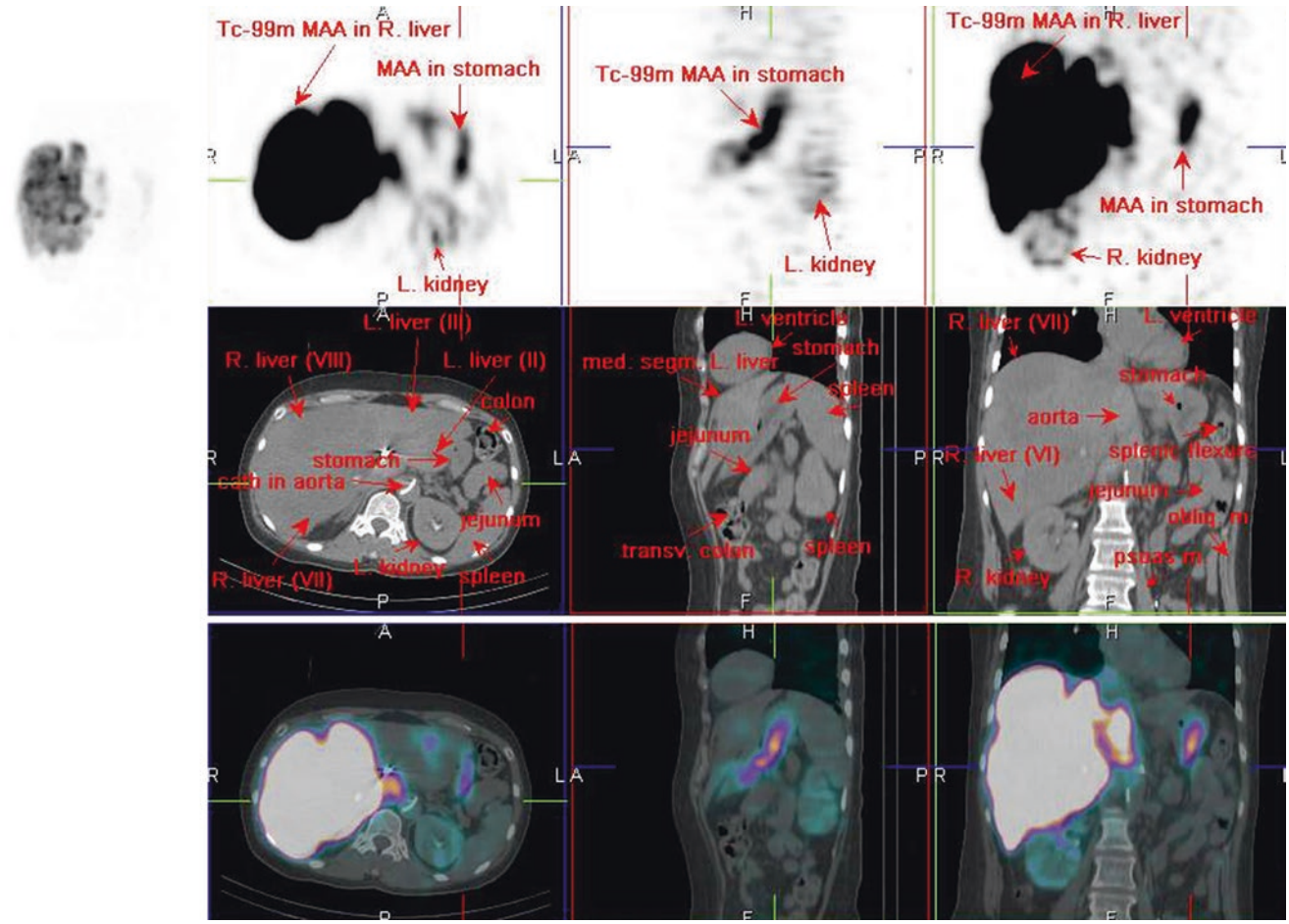

Fig. 3 ^{99m}Tc-MAA SPECT/CT

1.2.3 Case 3

A 57-year-old female patient with hepatic metastasis of breast cancer. Selected SPECT (*top*) and SPECT/CT (*bottom*) images of the liver with ^{90}Y microspheres injected into a hepatic arterial catheter showed increased activity in the right and left hepatic lobes, corresponding to metastatic lesions (Fig. 4) [13].

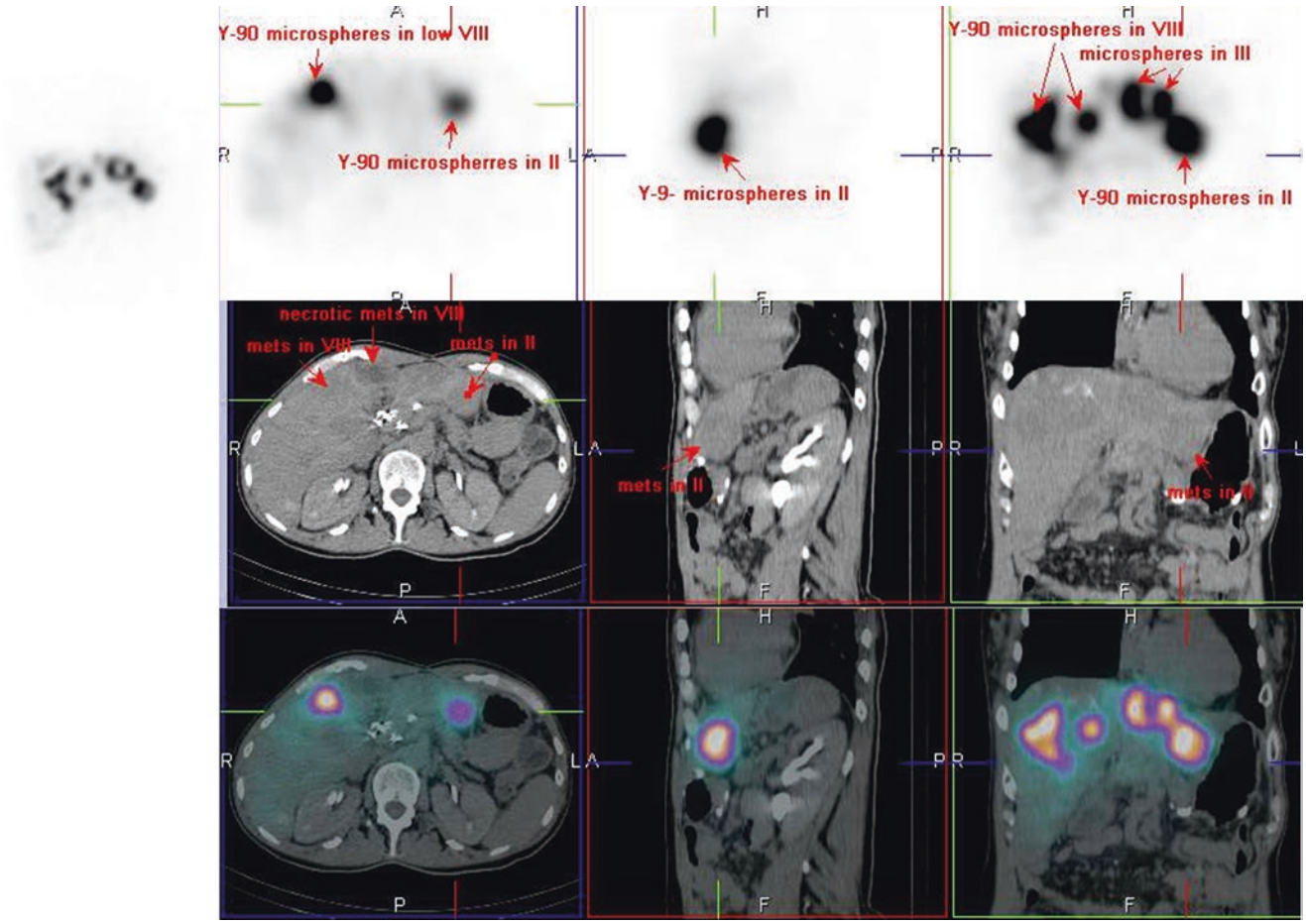

Fig. 4 ^{90}Y SPECT/CT

1.3 Neuroendocrine Tumors

1.3.1 Case 1

A 51-year-old male patient with chest tightness and dyspnea. He had prior history of a pancreatic neuroendocrine tumor, so ^{111}In-octreotide SPECT/CT was done. Images showed focal increased activity in a soft tissue mass at the pericardium, which was posteriorly confirmed to be a metastatic lesion (Fig. 5) [14].

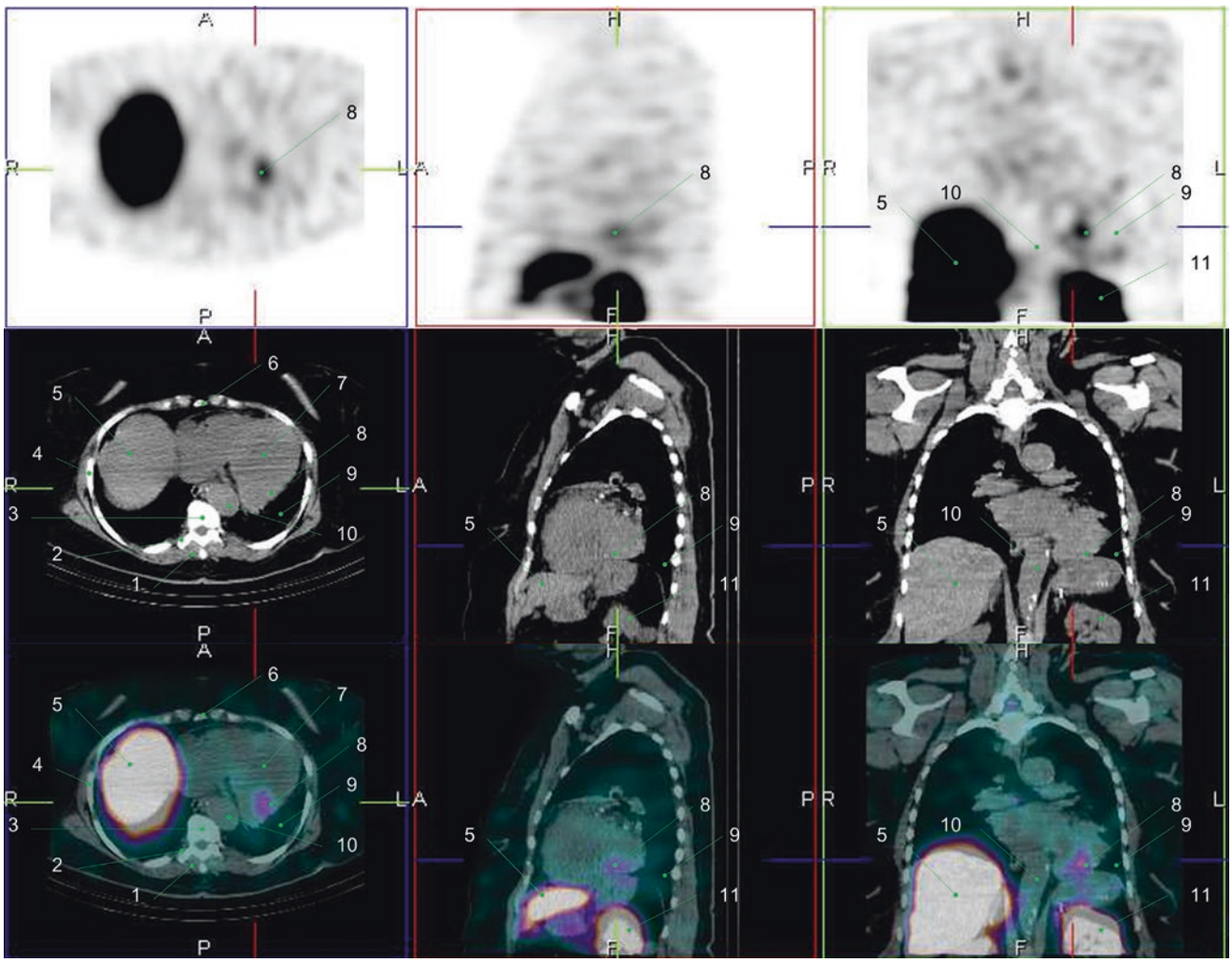

Fig. 5 1. Paraspinalis muscle
2. Transverse process
3. Vertebral body
4. Rib
5. Liver
6. Sternum
7. Left ventricle
8. Metastasis in pericardium
9. Left lower lobe of lung
10. Descending aorta
11. Left kidney

1.3.2 Case 2

A 72-year-old male patient with a history of midgut carcinoid. He attended with right shoulder and abdominal pain. ^{111}In-octreotide SPECT/CT was performed, finding focal increased activity in the right glenoid at a slerotic lesion and the right hepatic lobe at a large necrotic mass. Posterior biopsy confirmed the diagnosis of metastatic neuroendocrine tumor (Fig. 6) [15].

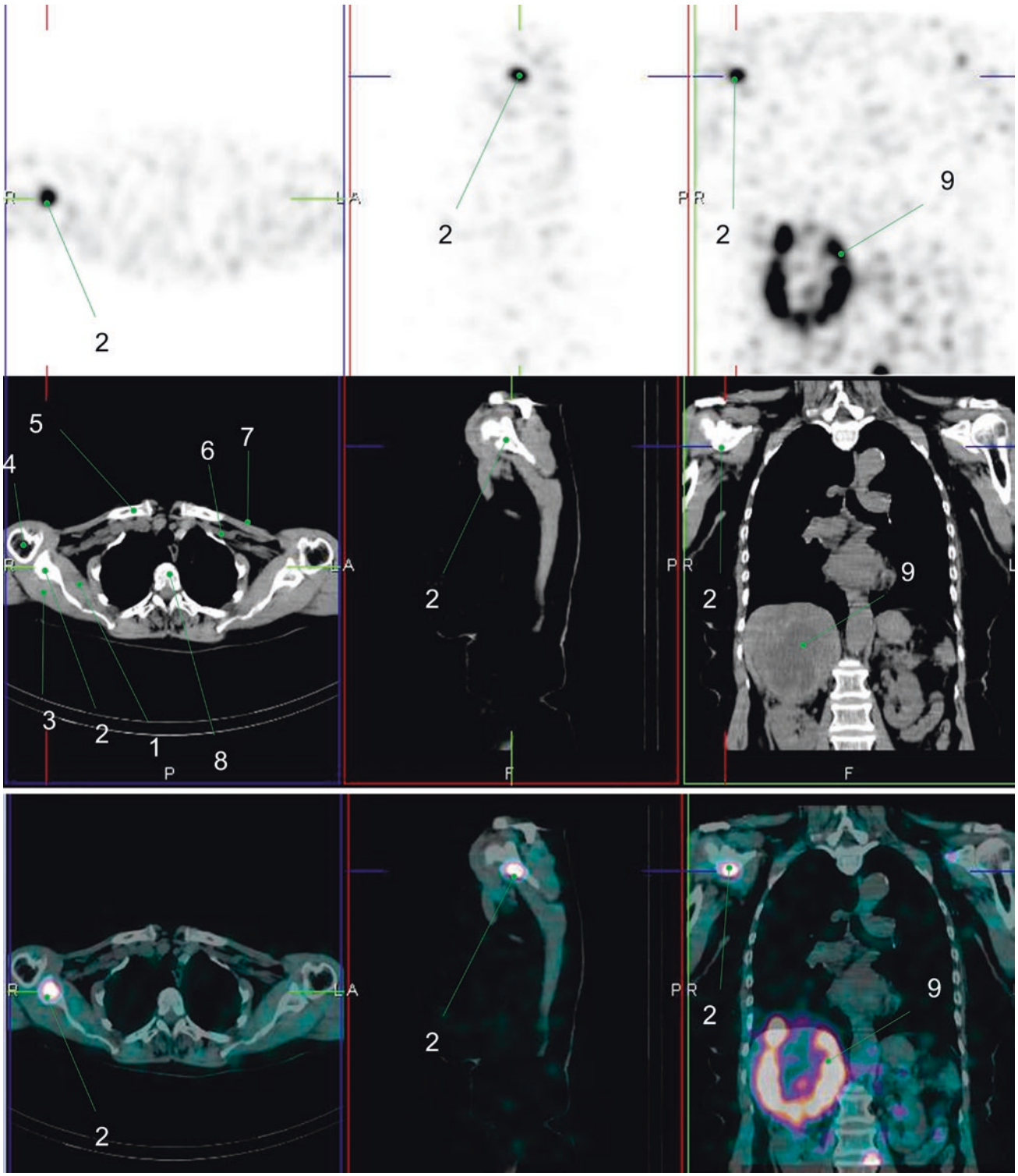

Fig. 6 1. Right subscapularis muscle
2. Metastasis in right scapula neck
3. Right supraspinatus muscle
4. Right humerus
5. Right clavicle
6. Left pectoralis minor muscle
7. Left pectoralis major muscle
8. Vertebral body
9. Liver metastasis with central necrosis

1.3.3 Case 3

A 71-year-old male patient with abdominal pain, diarrhea, and elevated chromogranin A. ^{111}In-octreotide SPECT/CT was performed, finding marked increased activity in a large pancreatic tail mass, as well as diffuse, increased activity in the portal vein. Surgical resection confirmed the diagnosis of a pancreatic neuroendocrine tumor with portal vein invasion (Fig. 7) [16].

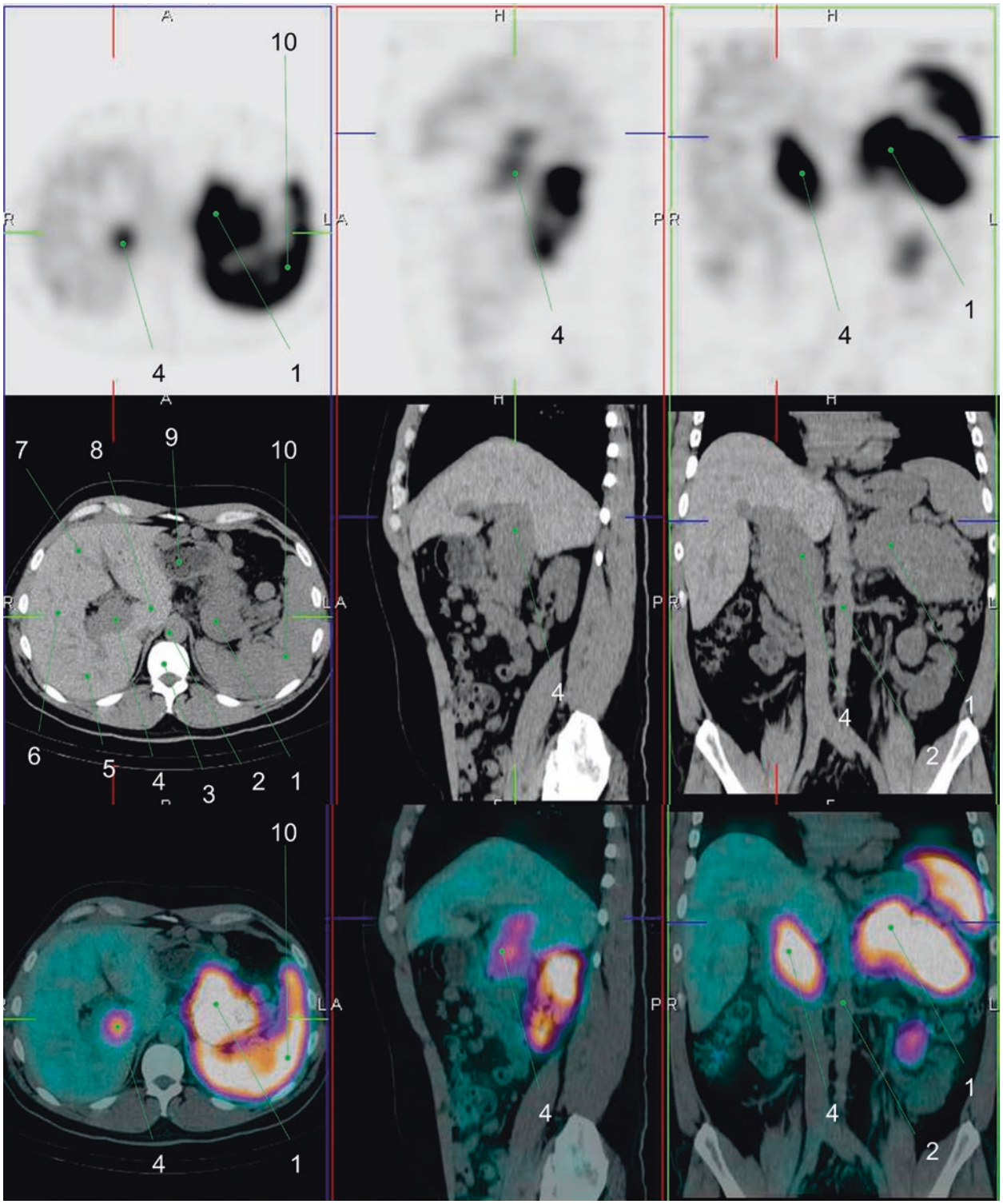

Fig. 7 1. Neuroendocrine tumor in the pancreatic tail
2. Abdominal aorta
3. Vertebral body
4. Neuroendocrine tumor in the portal vein
5. Liver, S6
6. Liver, S5
7. Liver, S4
8. Liver, S1
9. Stomach
10. Spleen

1.3.4 Case 4

A 62-year-old female patient with a history of midgut carcinoid. She presented with cough, dyspnea, and abdominal pain, so ^{111}In-octreotide SPECT/CT was done. Images showed a large mass in the right adrenal gland without abnormal increased activity. Also, diffuse, increased activity was noted in a consolidation at the right upper lung. Posterior biopsy of both lesions confirmed a right adrenal carcinoma and a metastatic neuroendocrine tumor in the right upper lung (Fig. 8) [17].

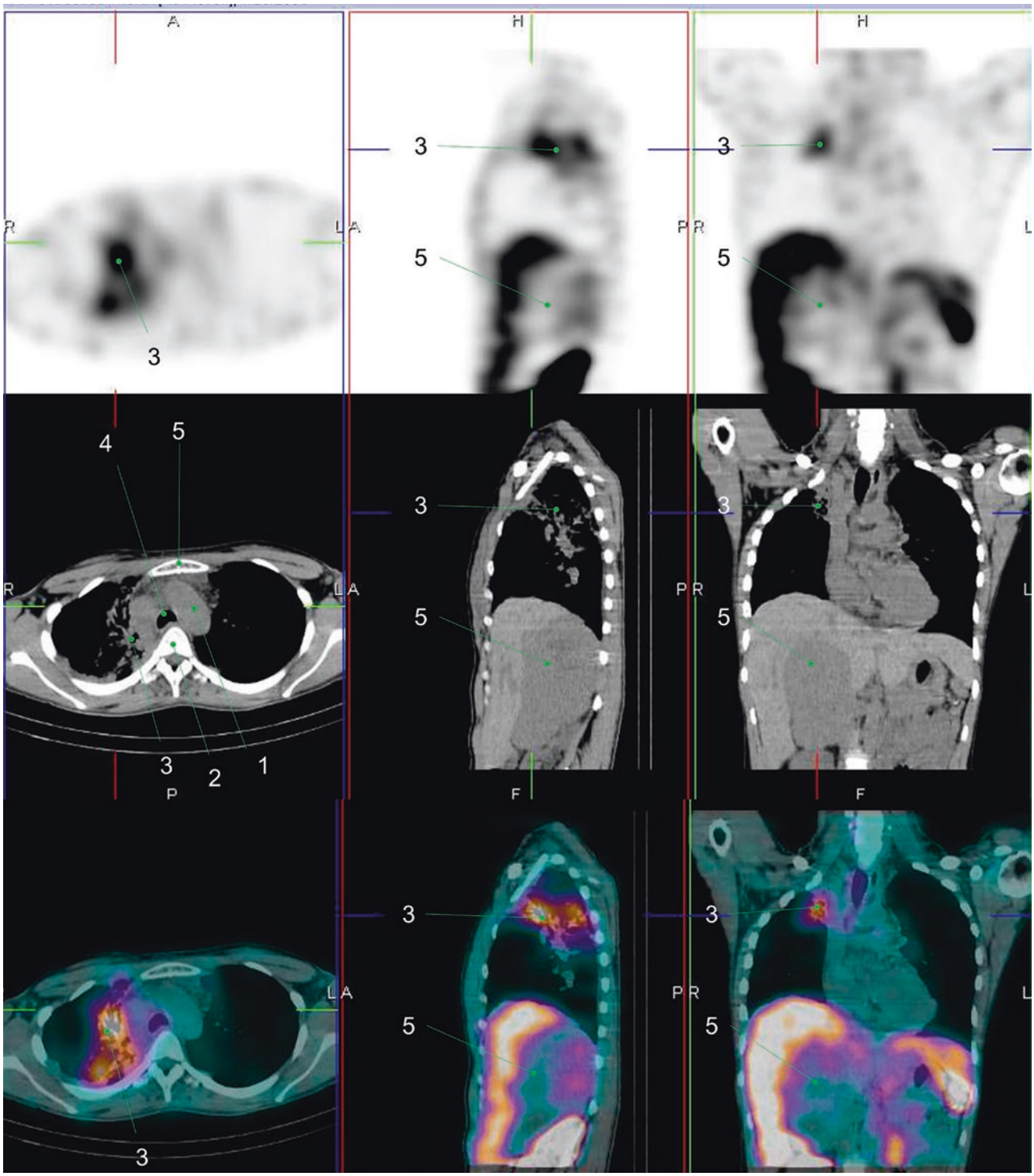

Fig. 8 1. Aortic arch
2. Vertebral body
3. Neuroendocrine tumor in RUL
4. Trachea
5. Right adrenal cancer

1.3.5 Case 5

A 54-year-old female patient with a history of rectal carcinoid. She developed abdominal pain and elevated serum levels of chromogranin A were found. ^{111}In-octreotide SPECT/CT was performed, finding multifocal increased uptake in the right hepatic lobe at several biopsy confirmed metastasis (Fig. 9) [18].

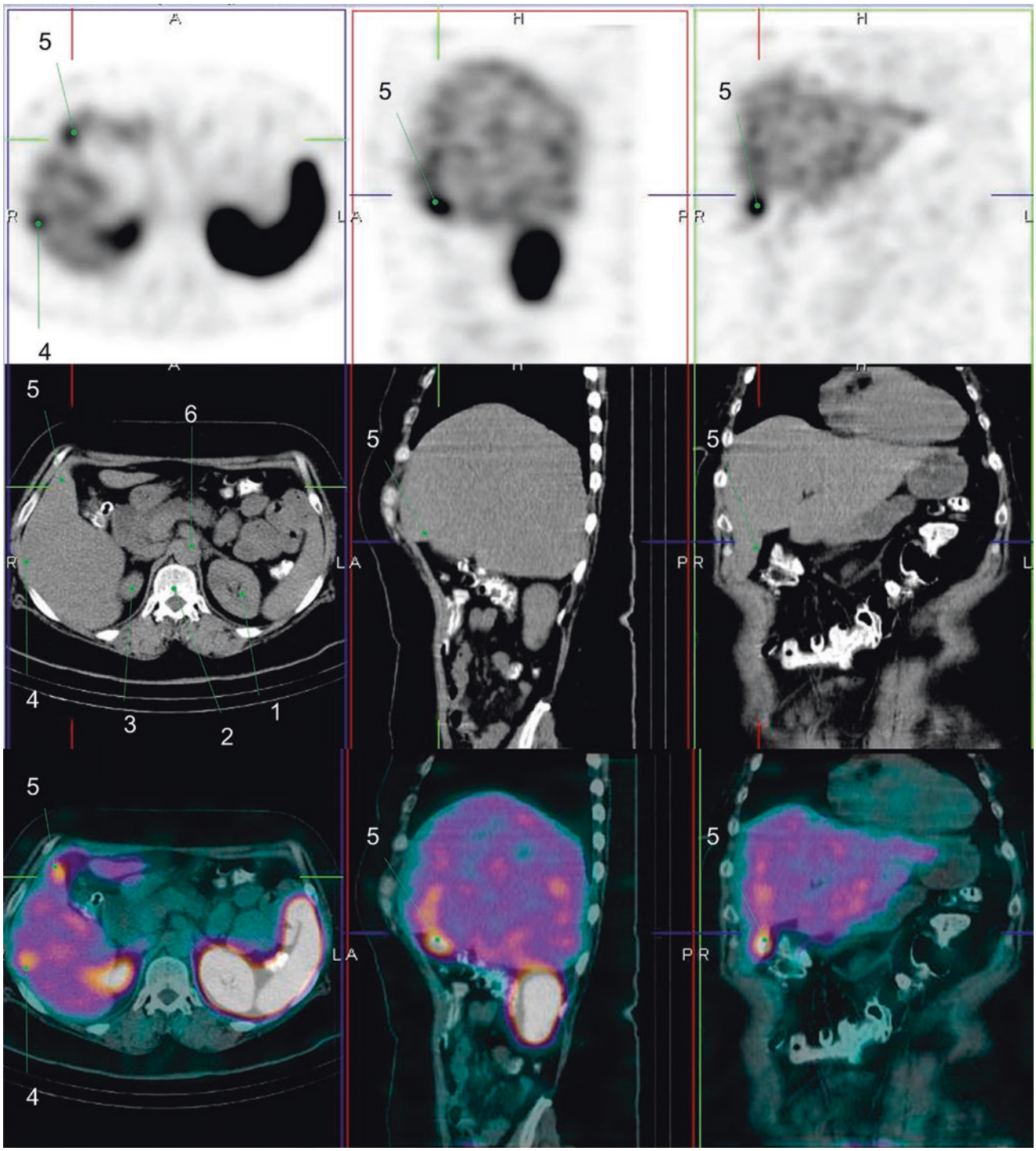

Fig. 9 1. Left kidney
2. Vertebral body
3. Right kidney
4. NE tumor in liver S6
5. NE tumor in liver S5
6. Abdominal aorta

1.3.6 Case 6

A 74-year-old female patient with abdominal pain and diarrhea. ^{111}In-octreotide SPECT/CT was done, finding focal increased activity in the pancreatic head. The surgical diagnosis was a pancreatic neuroendocrine tumor (Fig. 10) [21].

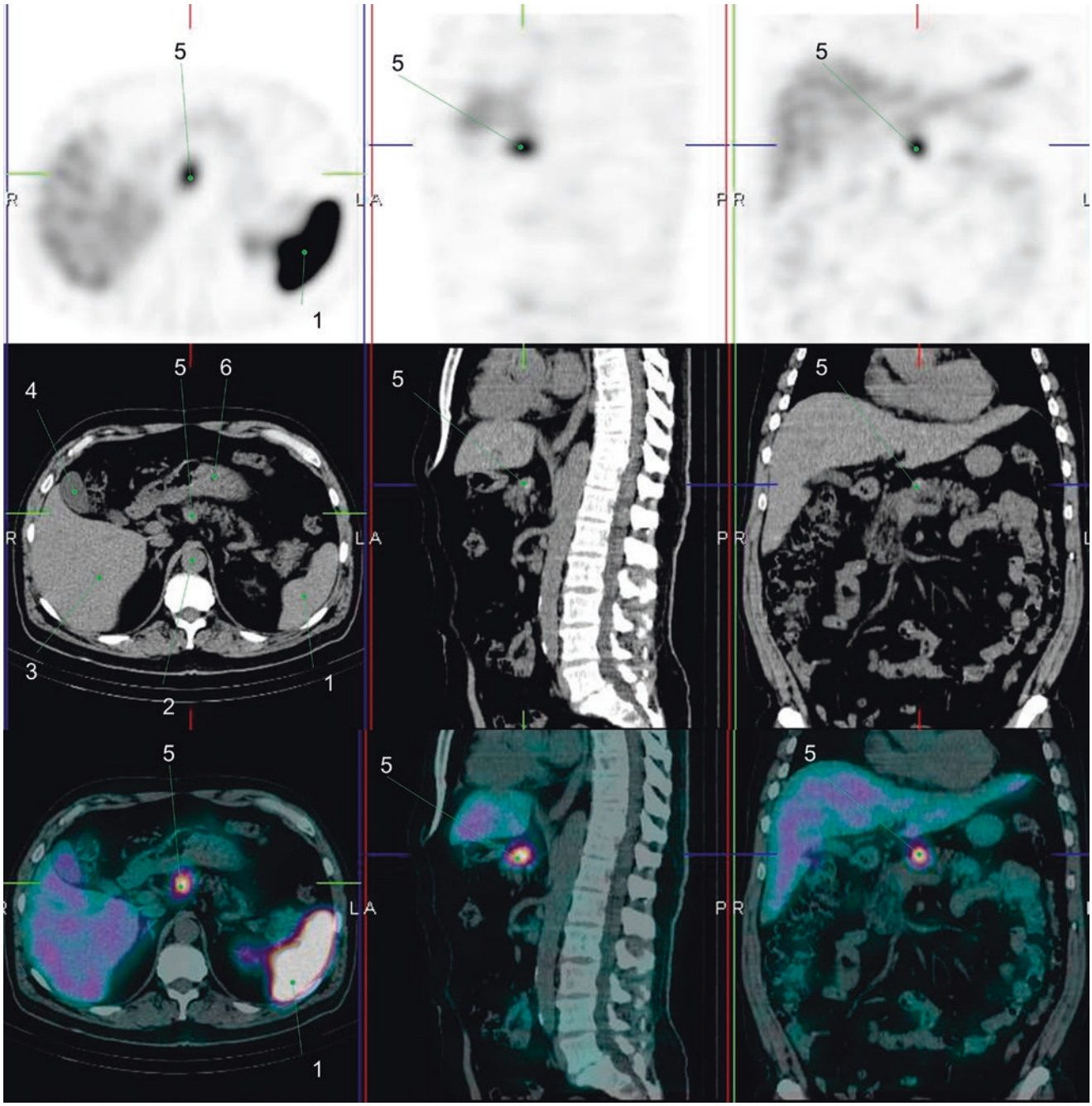

Fig. 10 1. Spleen
2. Abdominal aorta
3. Liver
4. Gallbladder
5. NE tumor in pancreatic body
6. Stomach

1.3.7 Case 7

A 67-year-old male patient with hypertension, abdominal pain, and palpitations. Elevated urinary catecholamines were found, so ^{123}I-MIBG SPECT/CT was performed. Images showed focal increased uptake in a left adrenal mass which was confirmed as a pheochromocytoma (Fig. 11) [22].

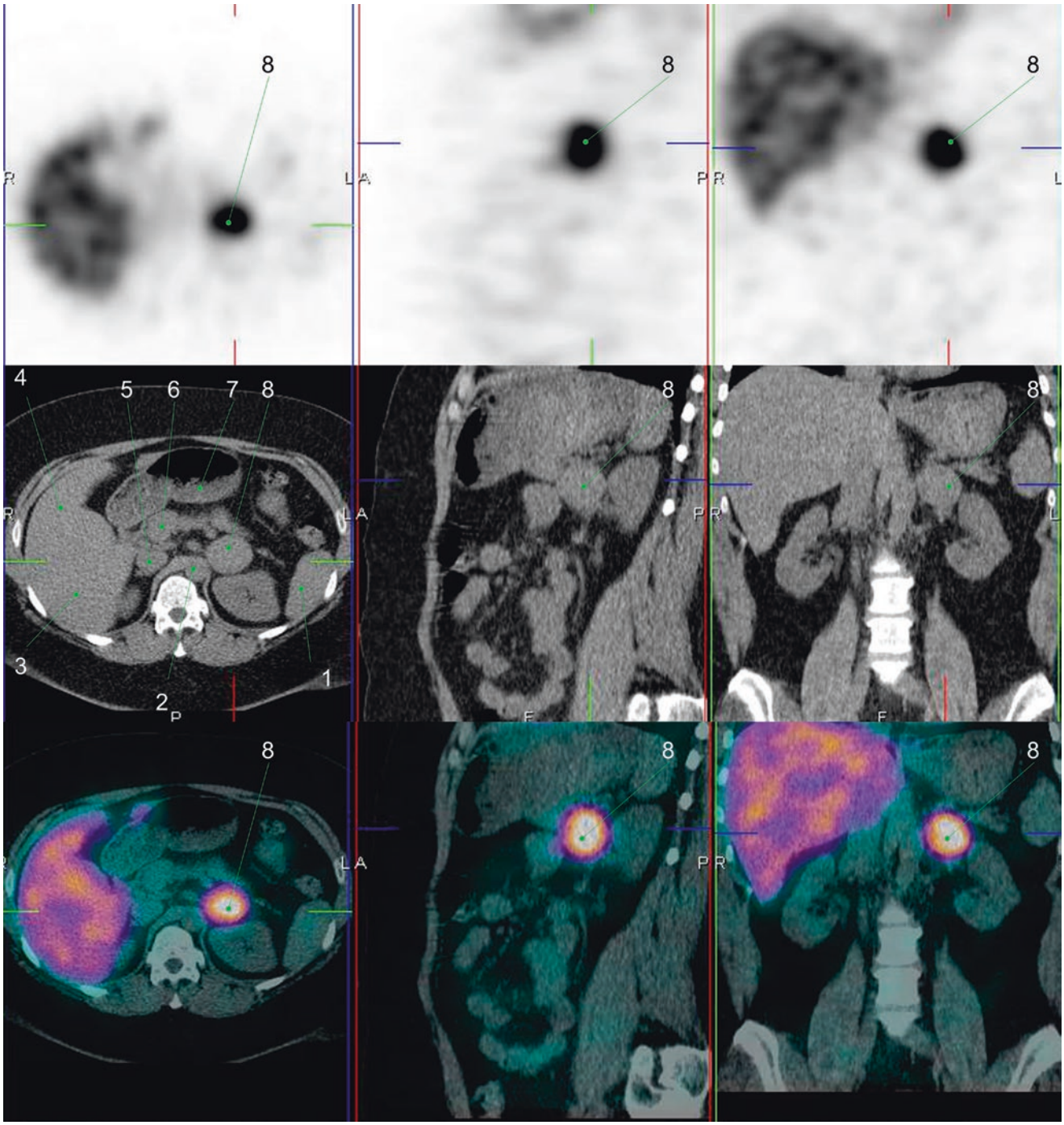

Fig. 11 1. Spleen
2. Abdominal aorta
3. Liver, S6
4. Liver, S5
5. IVC
6. Portal vein
7. Stomach
8. Left adrenal pheochromocytoma

1.3.8 Case 8

A 68-year-old female patient with a history of midgut carcinoid developed chest pain and dyspnea. Chest X-ray showed a newly developed lung nodulex nodule and she had elevated serum levels of chromogranin A, so ^{111}In-octreotide SPECT/CT was done. Images showed focal increased uptake in the right upper lung nodule, which was confirmed to be a metastatic neuroendocrine tumor (Fig. 12) [25].

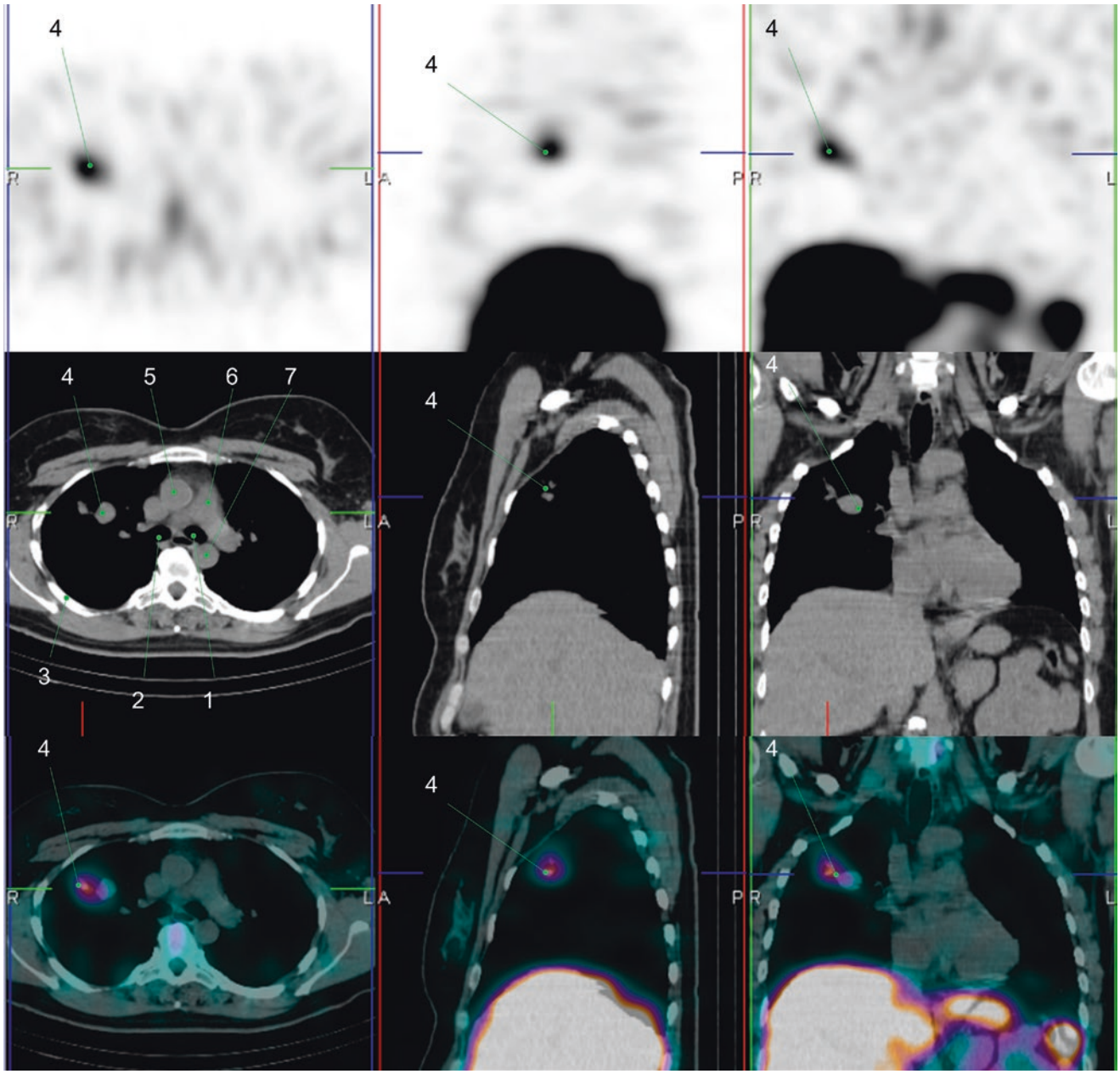

Fig. 12 1. Left main bronchus
2. Right main bronchus
3. Rib
4. Neuroendocrine tumor metastasis in right lung
5. Ascending aorta
6. Pulmonary trunk
7. Descending aorta

1.3.9 Case 9

A 64-year-old female patient with a neuroendocrine tumor in the pancreatic tail. Selected SPECT (*top*) and SPECT/CT (*bottom*) images of the upper abdomen with ^{111}In-octreotide showed a focal area of slightly increased activity in the pancreatic tail. No other lesions were observed (Fig. 13) [27].

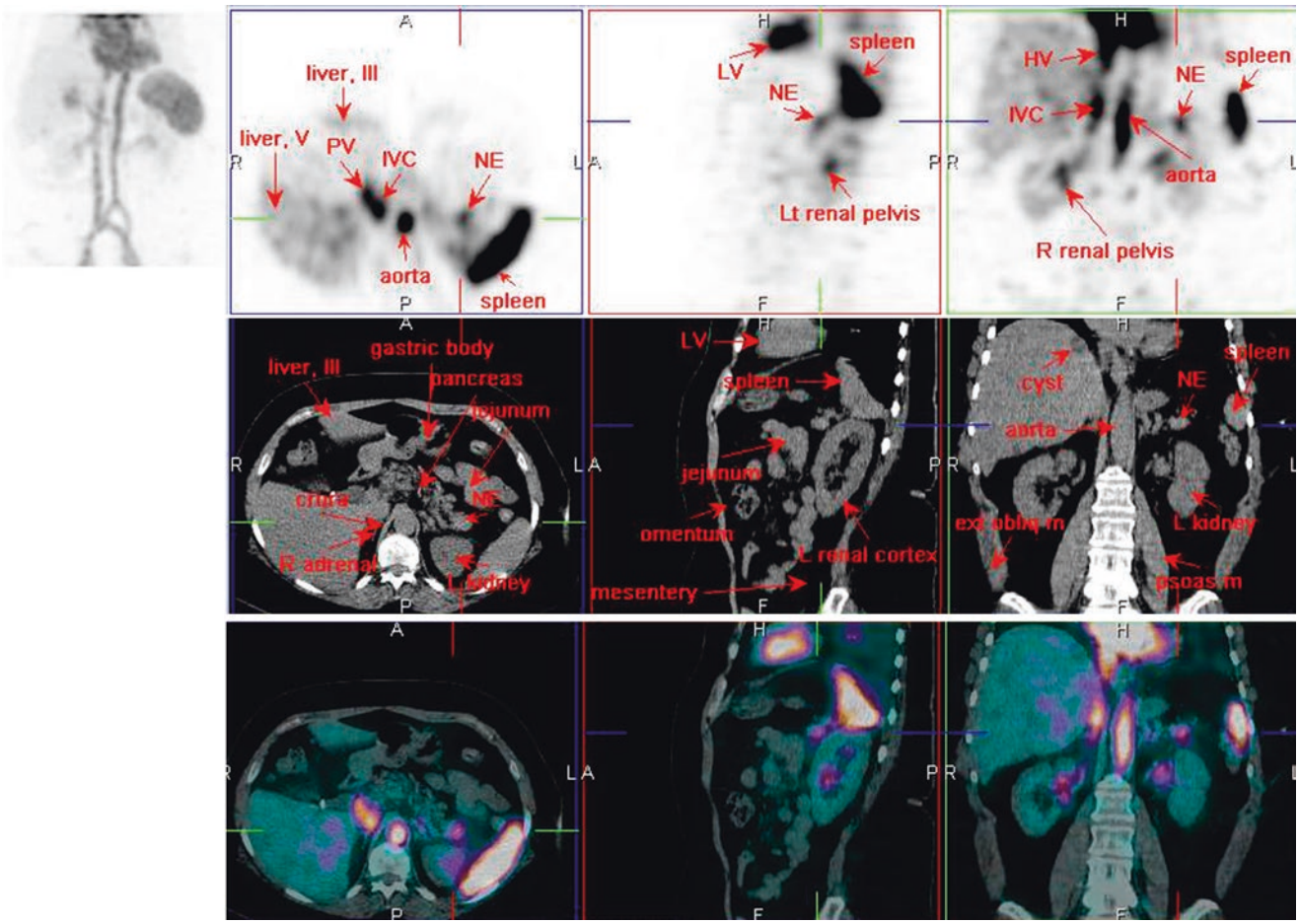

Fig. 13 ^{111}In-octreotide SPECT/CT

1.3.10 Case 10

A 41-year-old male patient with a history of carcinoid tumor, who attended for a regular check-up. ^{111}In-octreotide SPECT/CT was done, finding focal increased activity in the middle to lower abdomen corresponding to mesenteric lymph node metastases, as well as in two metastatic lesions in the right hepatic lobe (Fig. 14) [30].

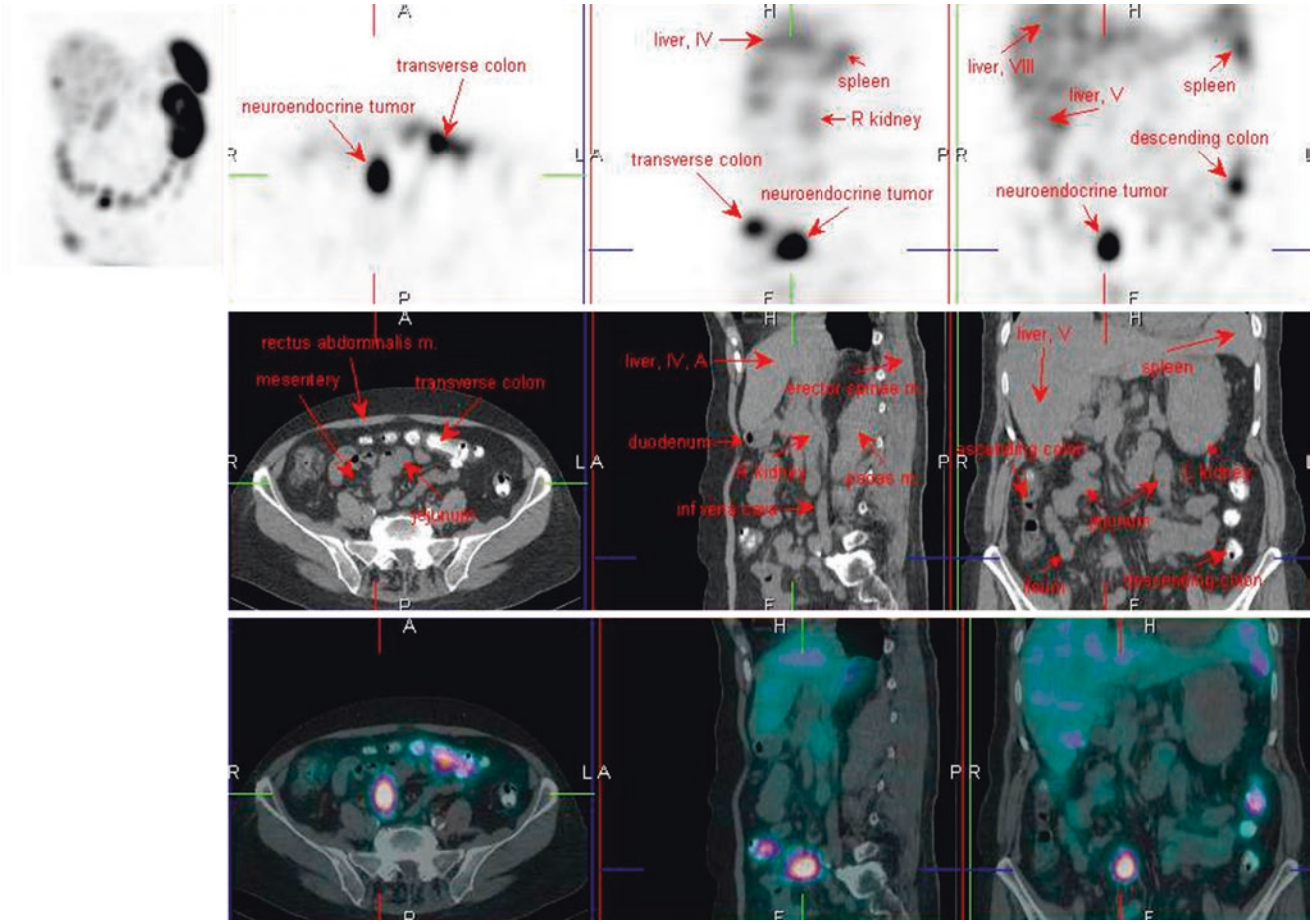

Fig. 14 ^{111}In-octreotide SPECT/CT

1.3.11 Case 11

A 39-year-old male patient with biopsy-proven lung carcinoid, who underwent ^{111}In-octreotide SPECT/CT for staging. Images showed focal increased activity in the right hilum at the primary tumor, without definite uptake in post-obstructive atelectasis (Fig. 15) [32].

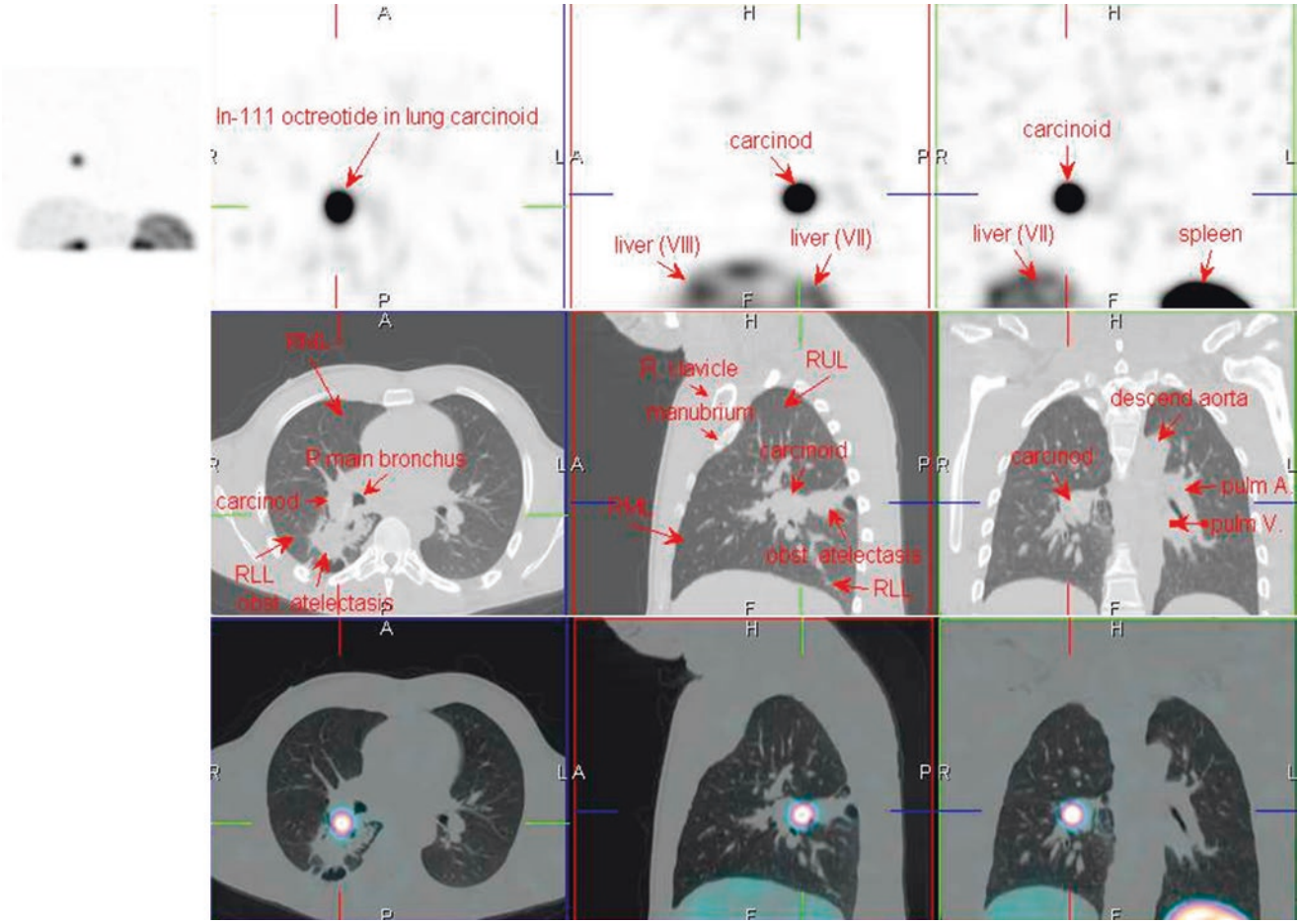

Fig. 15 ^{111}In-octreotide SPECT/CT

1.3.12 Case 12

A 51-year-old female patient with a biopsy confirmed diagnosis of transverse colon neuroendocrine tumor. ^{111}In-octreotide SPECT/CT was performed for staging, finding only focal increased uptake in the primary lesion at the proximal transverse colon (Fig. 16) [33].

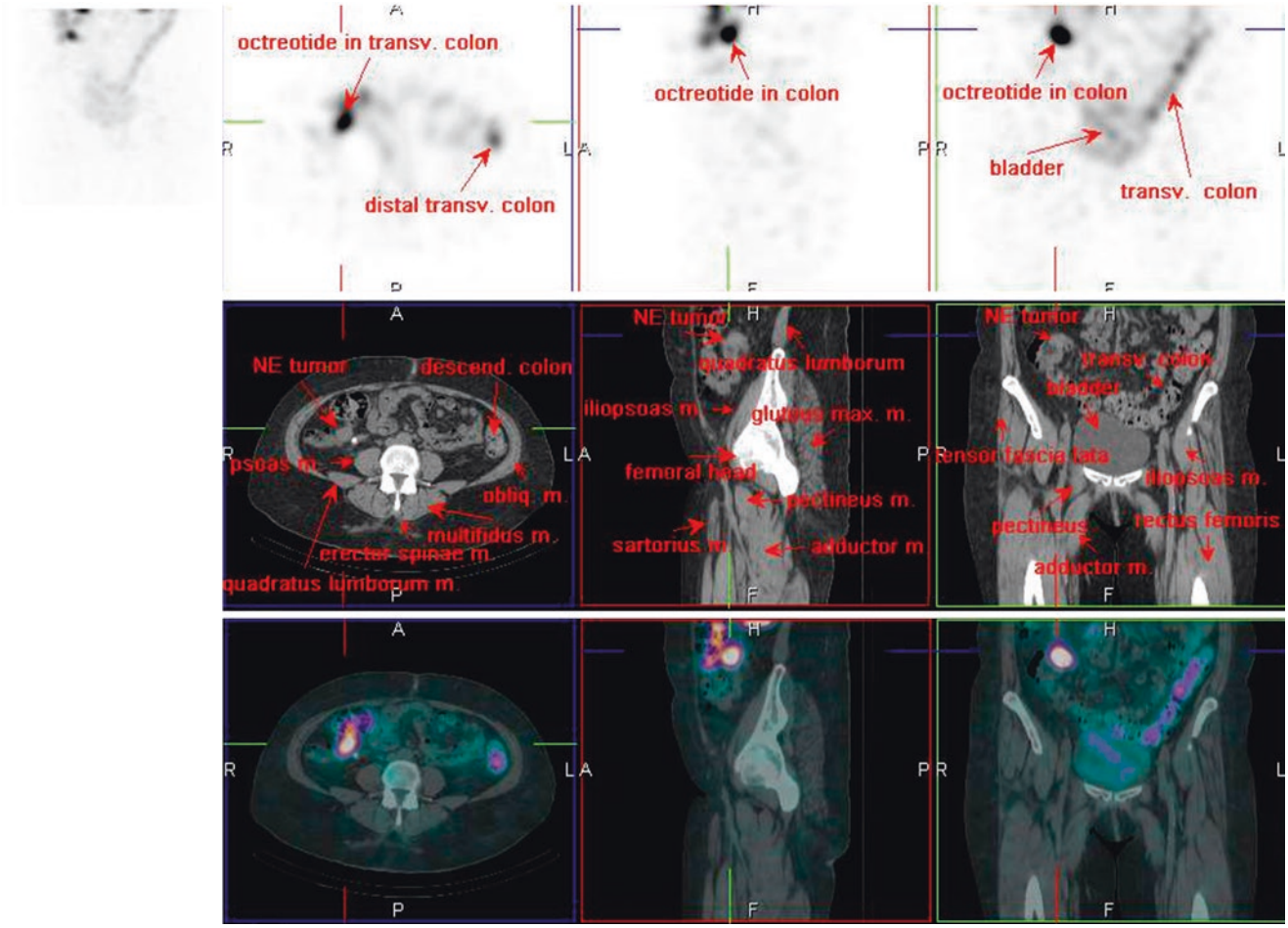

Fig. 16 ^{111}In-octreotide SPECT/CT

1.4 Neuroblastoma

1.4.1 Case 1

A 3-year-old girl with confirmed diagnosis of retroperitoneal neuroblastoma. ^{123}I-MIBG SPECT/CT was performed for further evaluation. Images showed focal increased uptake in a retroperitoneal mass adjacent to the left psoas muscle, corresponding to the primary tumor. Neuroblastoma is a neural crest cell tumor arising from the sympathetic chain, commonly in the adrenal gland, and the mean age at the diagnosis was 2 years. Metastases may be found in 75% of these patients. Meta-iodobenzylguanidine (MIBG) is similar to norepinephrine and is taken up by chromaffin granules that are in neuroblastoma and pheochromocytoma (Fig. 17) [35].

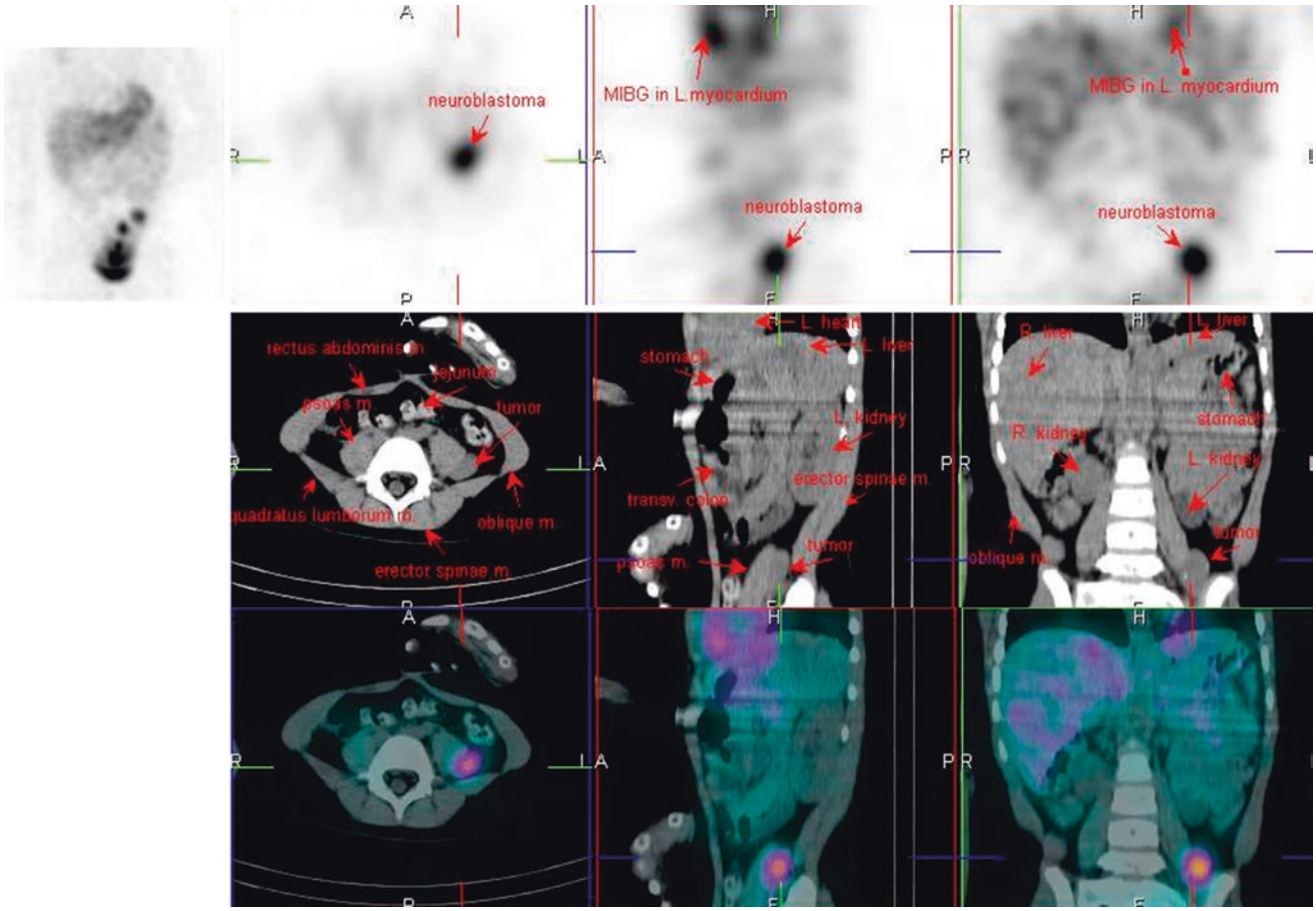

Fig. 17 ^{123}I-MIBG SPECT/CT

1.5 Paraganglioma

1.5.1 Case 1

A 59-year-old male patient, who attended with hypertension and perspiration. Elevated levels of urinary catecholamines were found, so ^{123}I-MIBG SPECT/CT was done for further evaluation. Images showed focal increased activity in a retroperitoneal mass at the aortocaval space, as well as in the left kidney superior pole. The surgical diagnosis confirmed a primary renal paraganglioma with retroperitoneal metastasis (Fig. 18).

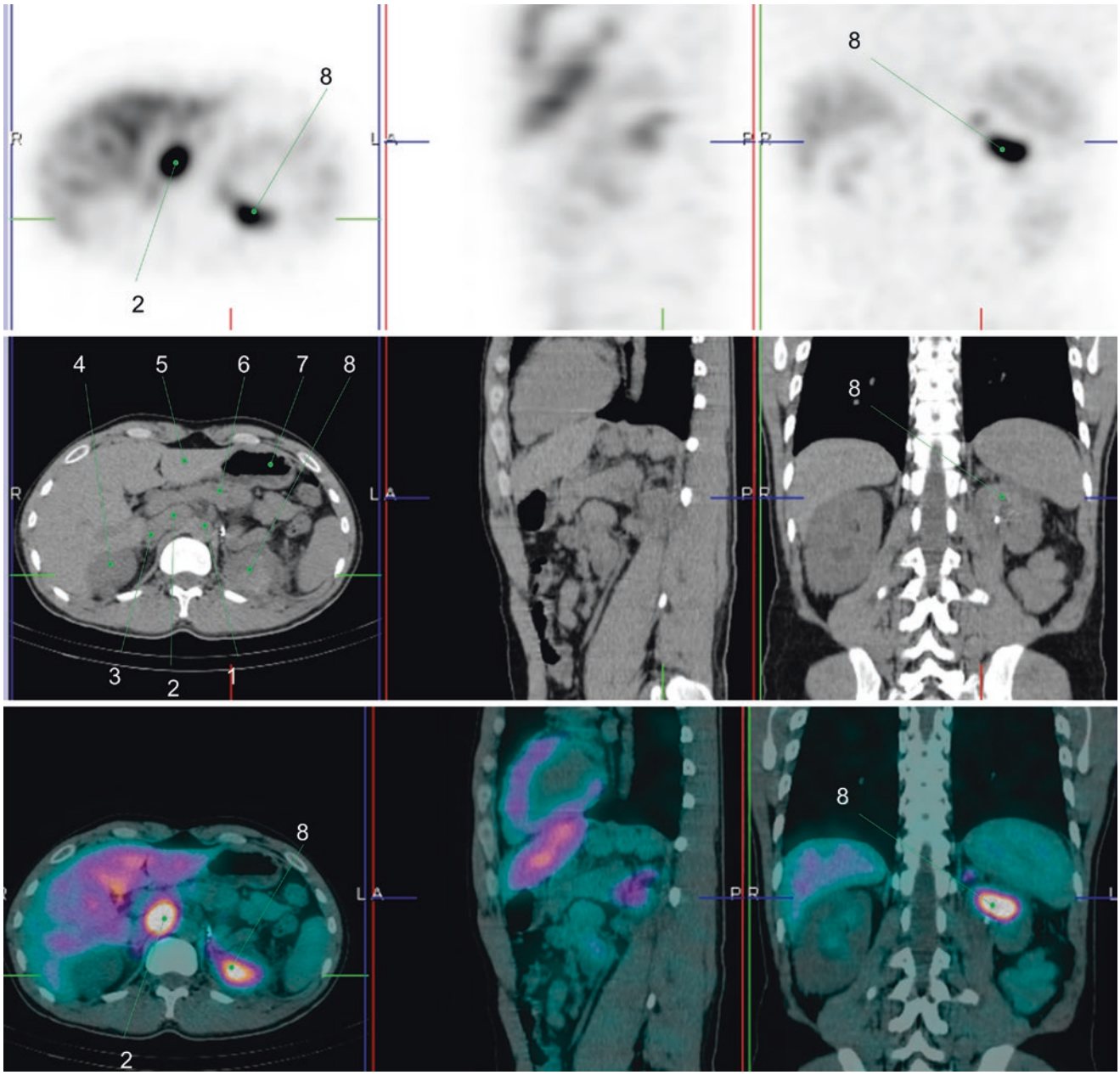

Fig. 18 1. Abdominal aorta
2. Metastatic paraganglioma in aortocaval area
3. IVC
4. Right kidney
5. Liver, left lobe
6. Pancreas
7. Stomach
8. Renal paraganglioma

1.5.2 Case 2

A 57-year-old female patient with a history of left adrenal paraganglioma, who attended for routine check-up. ^{123}I-MIBG SPECT/CT was performed, showing heterogeneous activity in the liver, with a focal nodular increased uptake in segment 5 (V). Heterogeneous activity in the liver is physiologic and related to timing of the imaging and radiotracer metabolism and excretion through the biliary system. However, focal increased uptake is an abnormal finding, and in this case, it corresponded to a metastatic lesion. Also, an active metastasis was found in the T8 vertebral body (Fig. 19) [36].

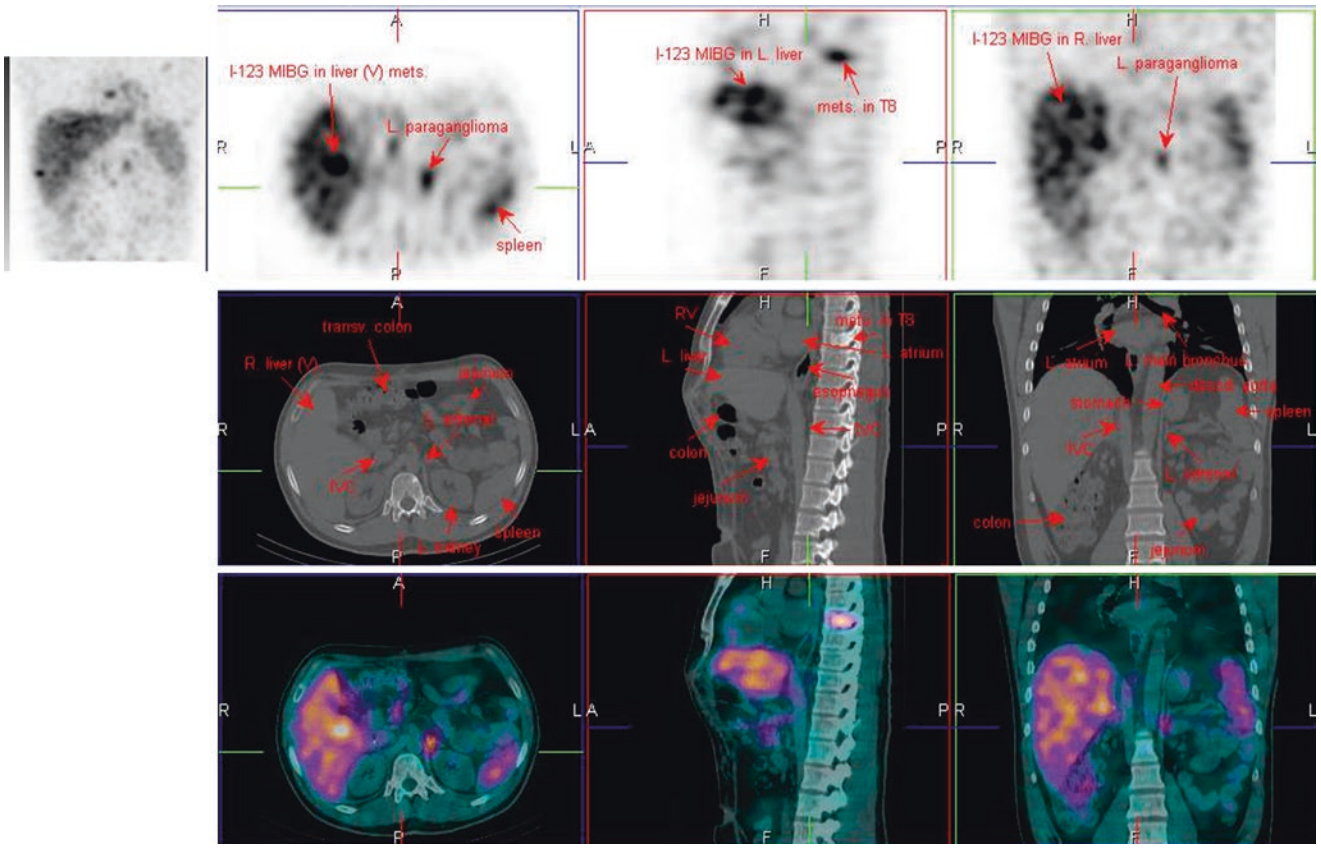

Fig. 19 ^{123}I-MIBG SPECT/CT

1.6 Thyroid Cancer

1.6.1 Case 1

A 59-year-old male patient with a history of thyroid cancer, who underwent coronary CT, finding incidentally multiple lung nodules. ^{131}I SPECT/CT showed moderately to intense increased iodine uptake in the nodules, confirming metastatic disease. Iodine therapy with 200 mCi of ^{131}I was administered (Figs. 20, 21, 22 and 23) [37].

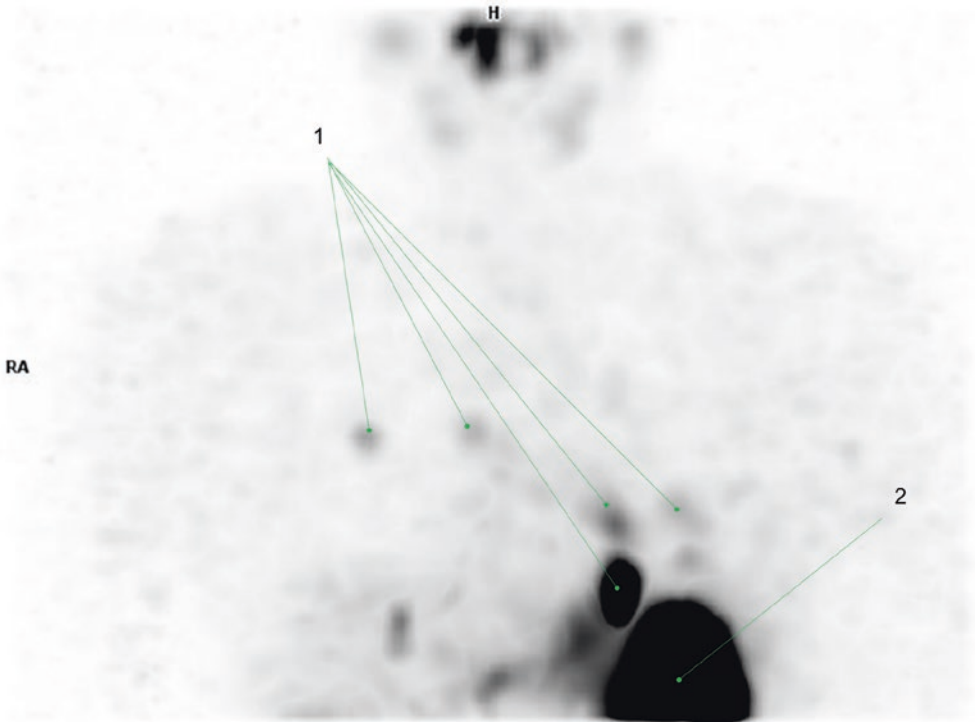

Fig. 20 1. Lung metastases
2. Physiologic colonic uptake

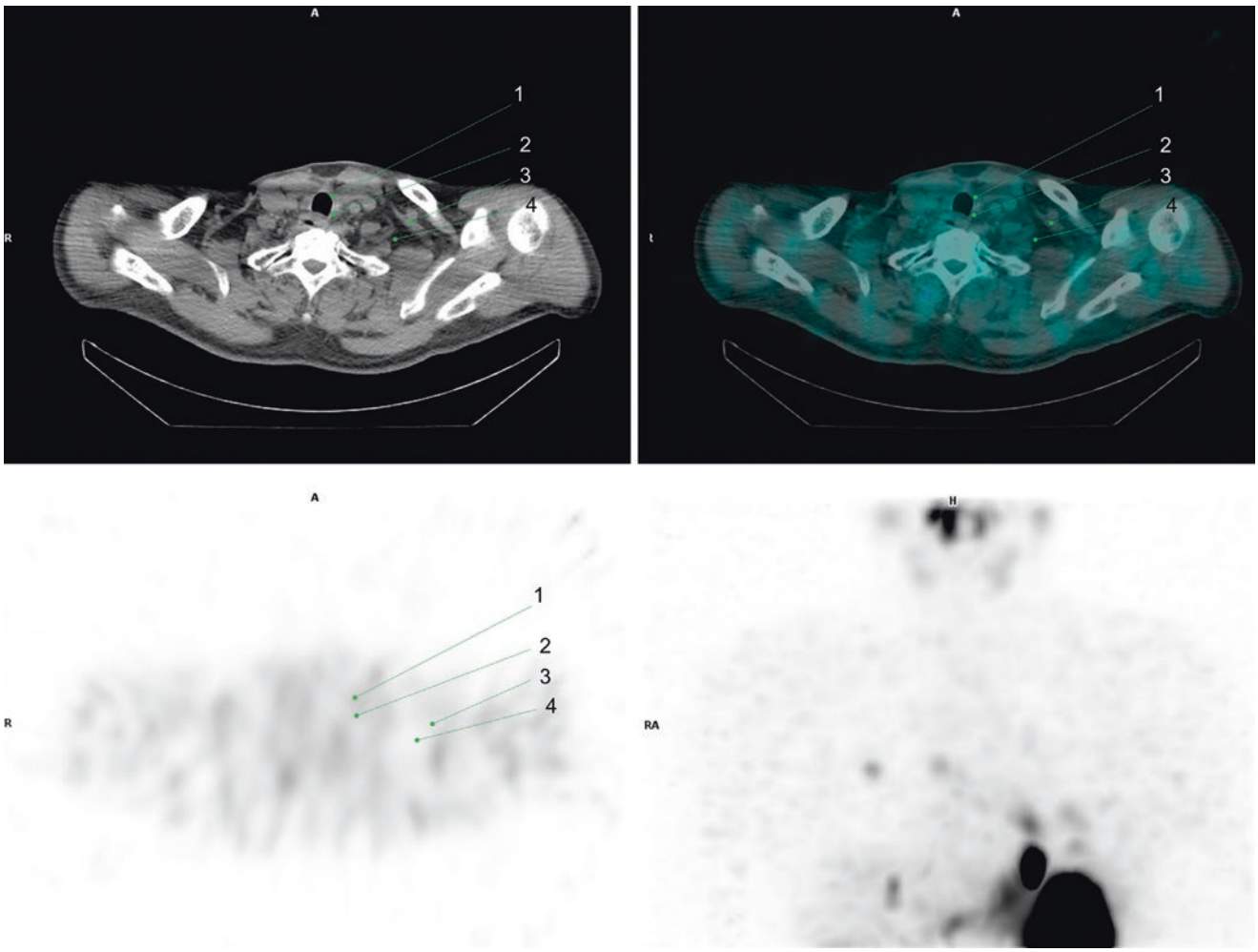

Fig. 21 1. Thyroid bed
2. Left neck, level VI
3. Left sternocleidomastoid muscle
4. Left neck, level IV

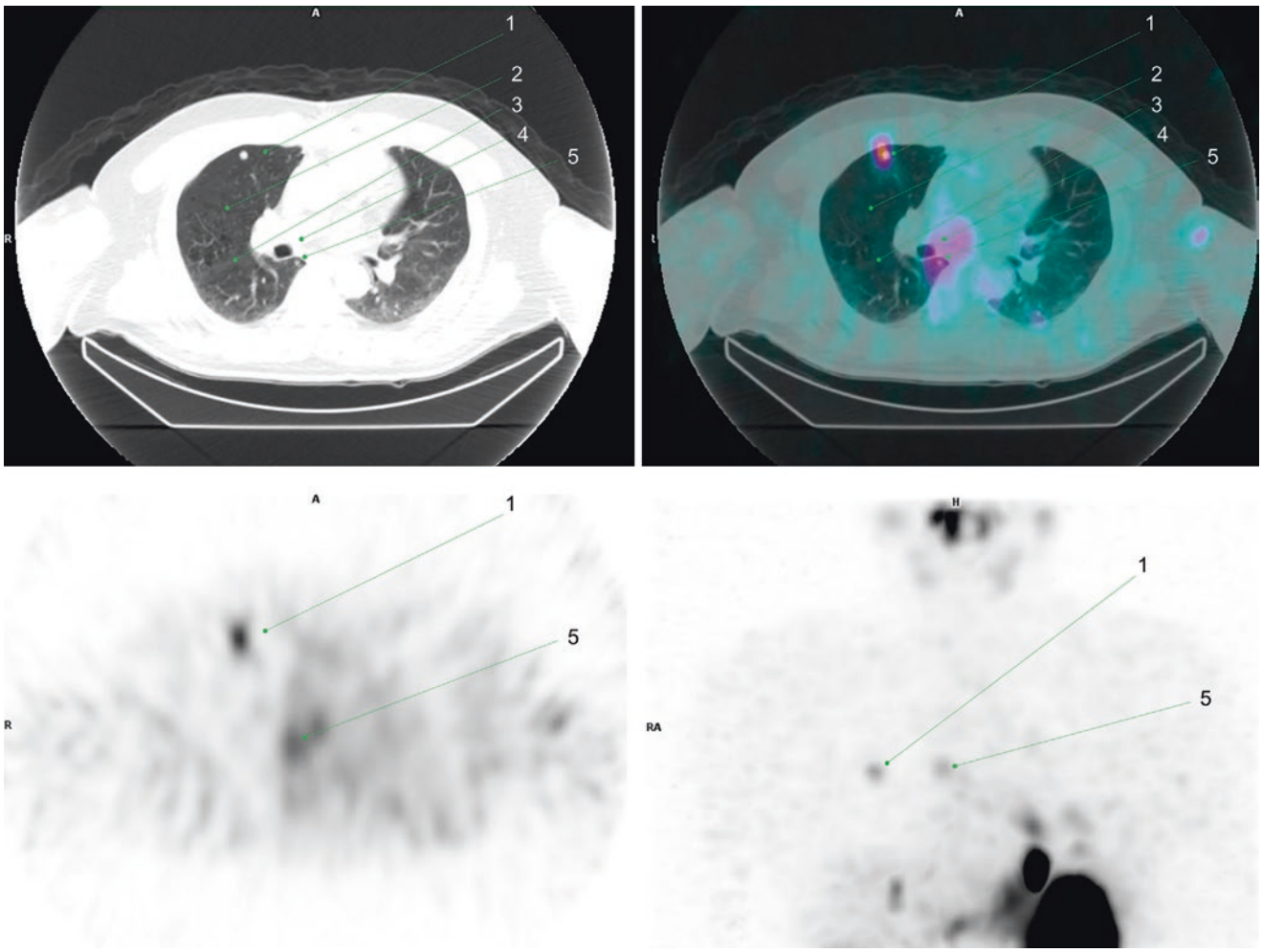

Fig. 22 1. Right middle lobe (RML) anterior segment metastatic nodule
2. Right lung minor fissure
3. Right lung major fissure
4. Right bronchus intermedius
5. Right lower lobe (RLL) superior segment metastatic nodule

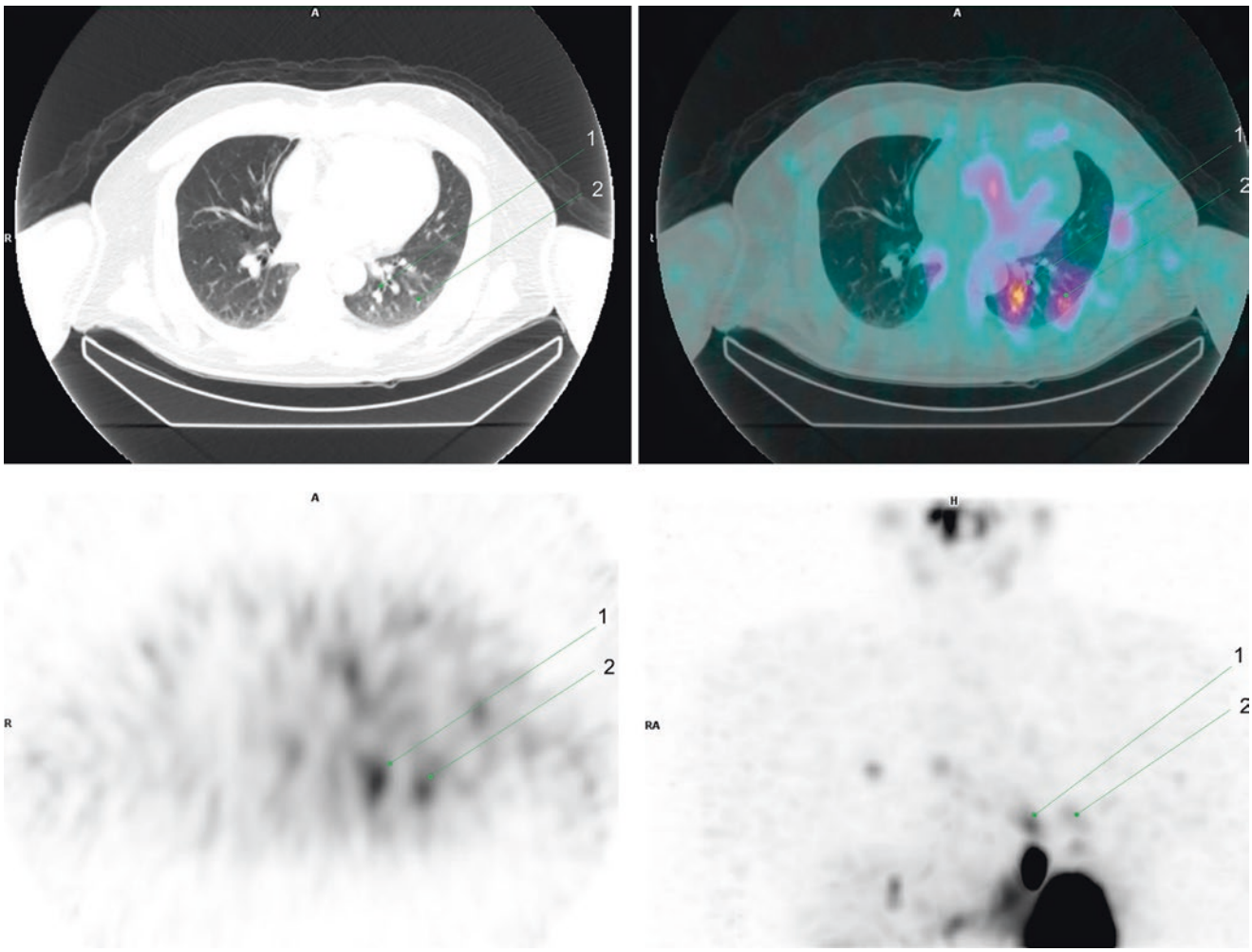

Fig. 23 1. Left lower lung lobe superior segment metastatic nodule
2. Left lower lung lobe lateral basal segment metastatic nodule

1.6.2 Case 2

A 34-year-old female patient with thyroid cancer, who underwent total thyroidectomy with central neck dissection. On ^{131}I ablation scan, bone metastases were found, which were treated with 250 mCi of ^{131}I. Post-treatment iodine scan and SPECT/CT were taken, showing intense focal iodine uptakes at T4 and T6, confirming iodine-avid bone metastases (Figs. 24, 25, 26, 27, 28, and 29) [38].

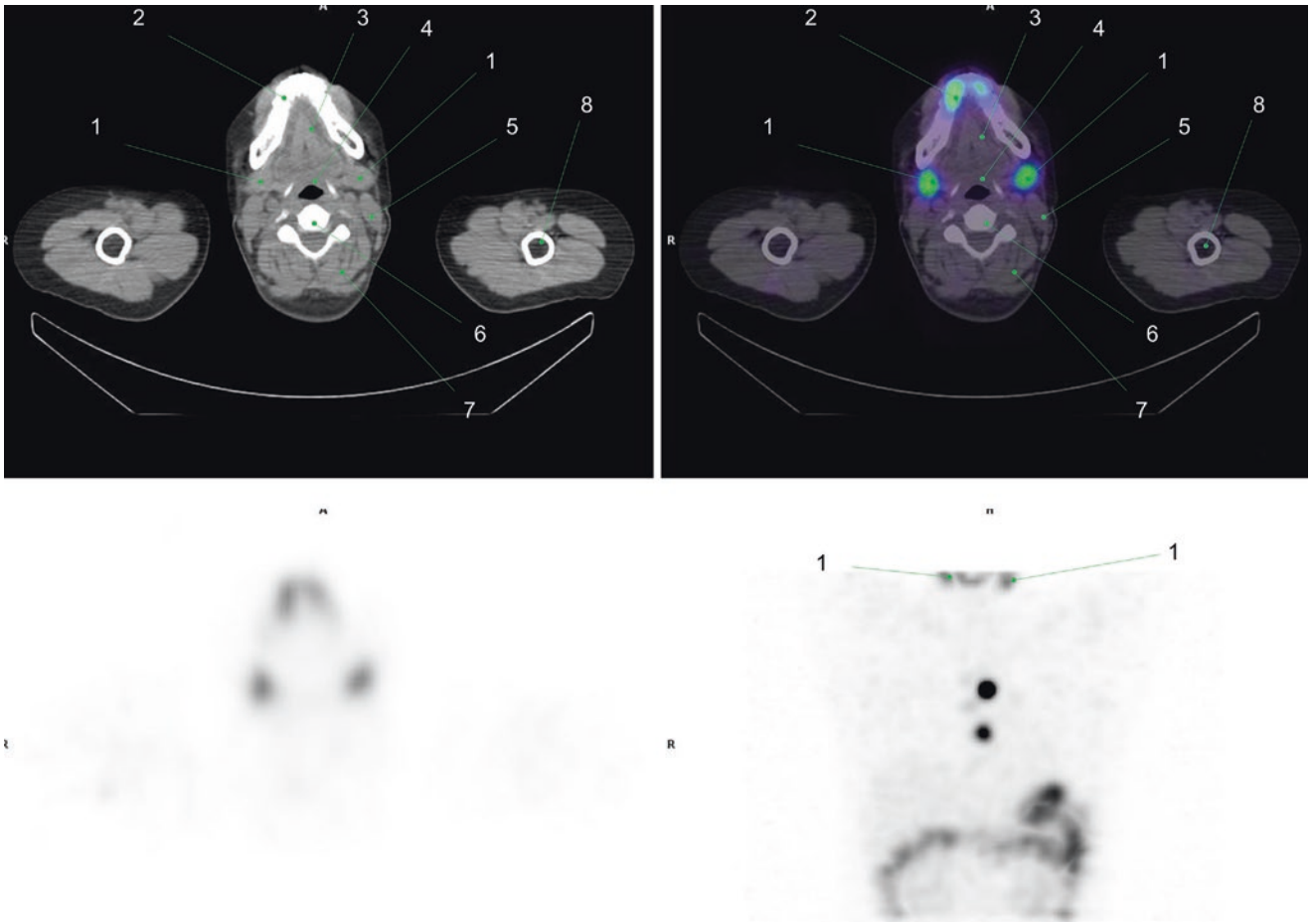

Fig. 24 1. Submandibular glands
2. Body of mandible
3. Genioglossus
4. Trachea
5. Sternocleidomastoid muscle
6. C2 spine
7. Obliquus capitis inferior muscle

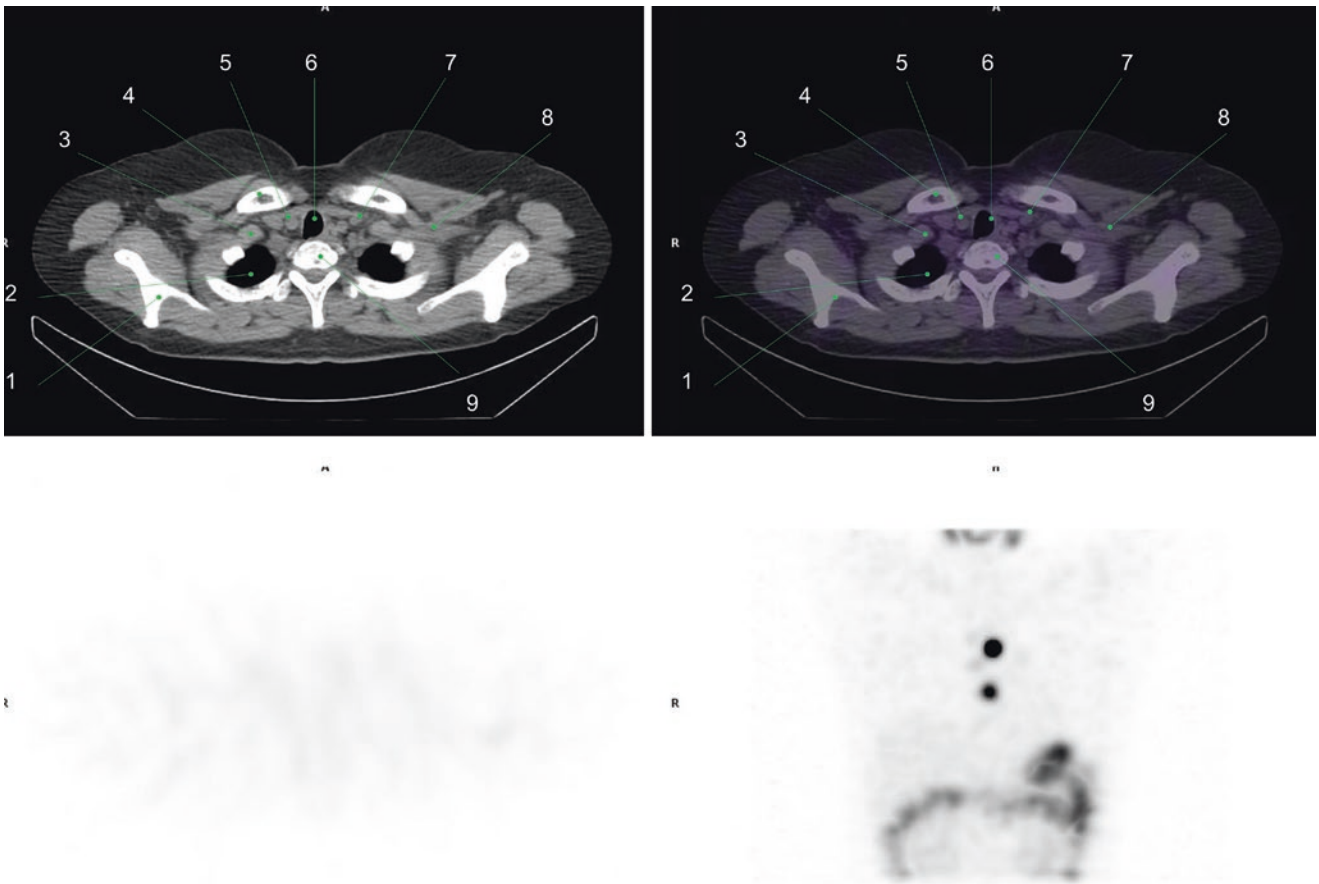

Fig. 25 1. Right scapula
2. Right lung apex
3. Right subclavian artery
4. Right clavicle
5. Right common carotid artery
6. Trachea
7. Left internal jugular vein
8. Left subclavian vein
9. T2 spine

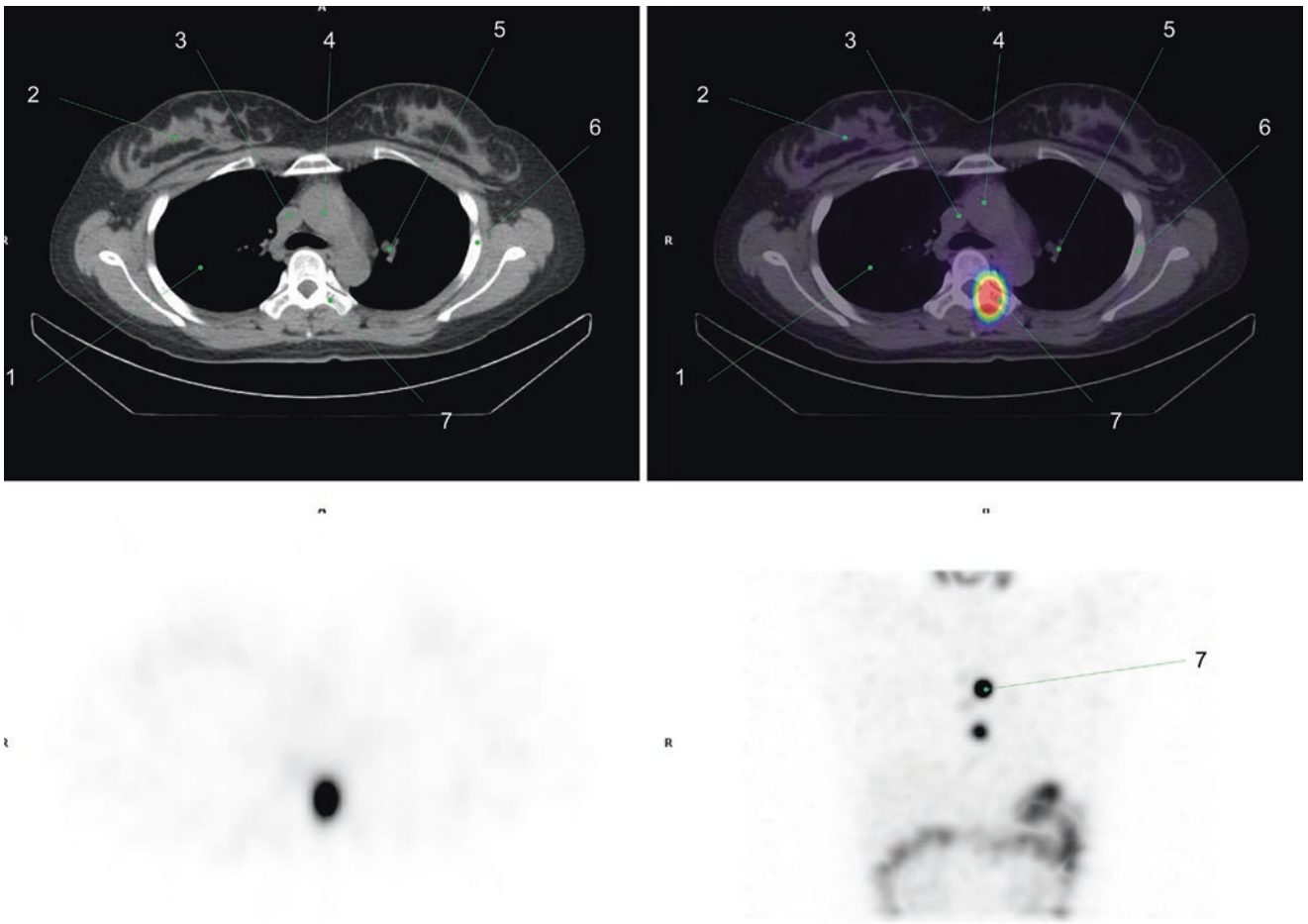

Fig. 26 1. Lung
2. Breast
3. Superior vena cava
4. Ascending aorta
5. Left pulmonary artery
6. Left fourth rib
7. Vertebral arch of T4 spine (metastasis)

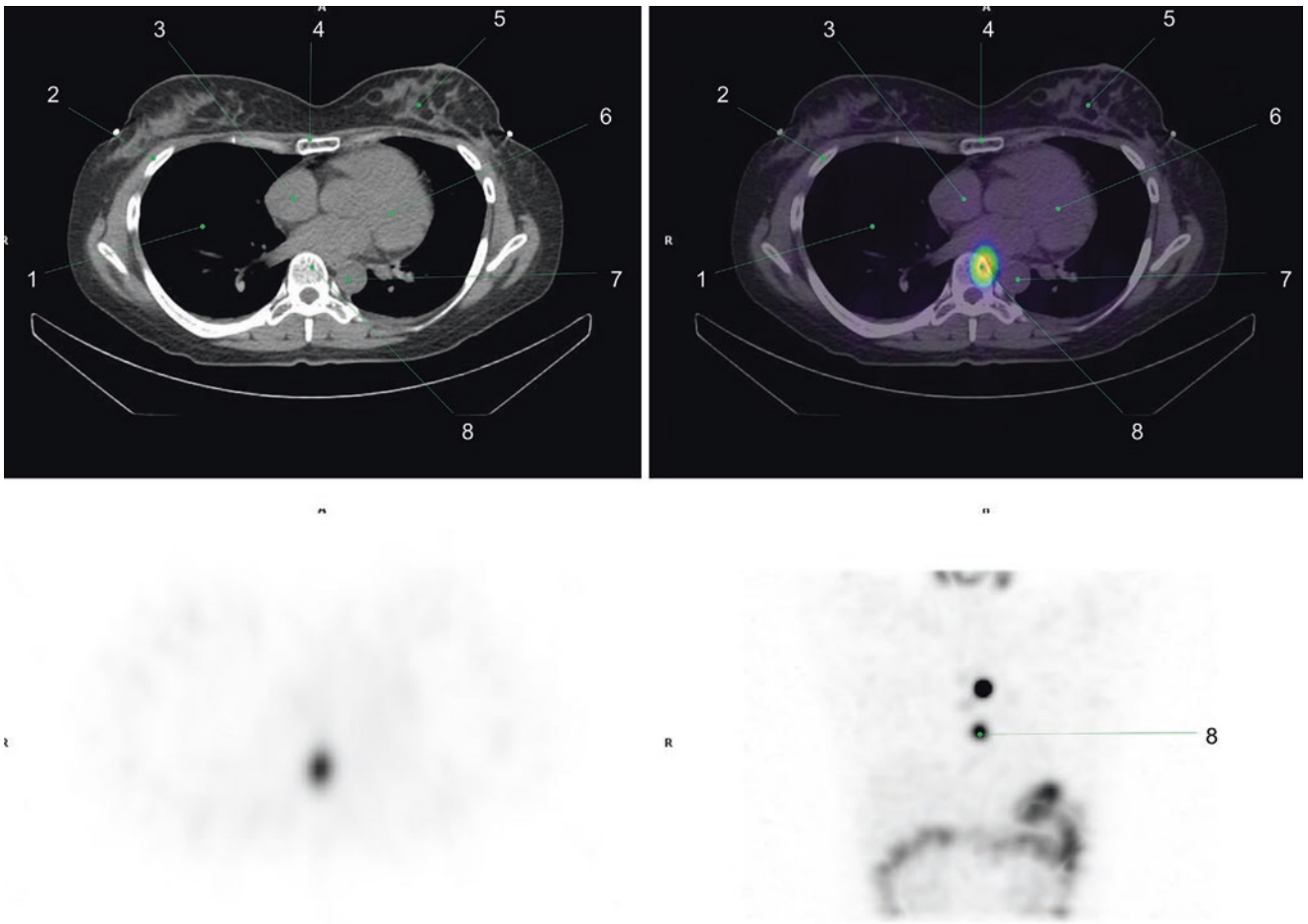

Fig. 27 1. Lung parenchyma
2. Right fourth rib
3. Right atrium
4. Sternum
5. Left breast parenchyma
6. Left ventricle
7. Descending aorta
8. Vertebral body of T6 (metastasis)

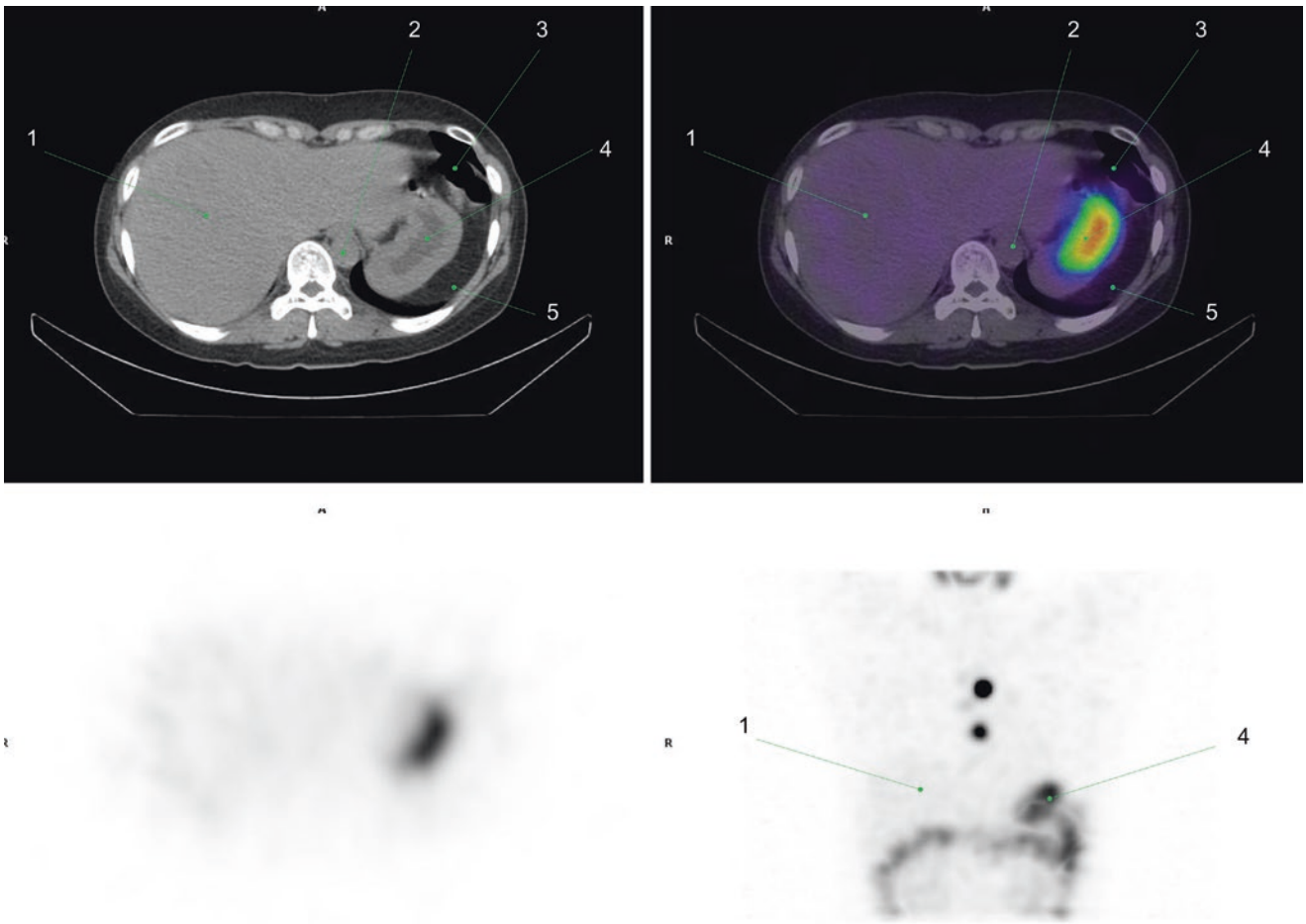

Fig. 28 1. Liver
2. Descending aorta
3. Transverse colon
4. Stomach
5. Diaphragm

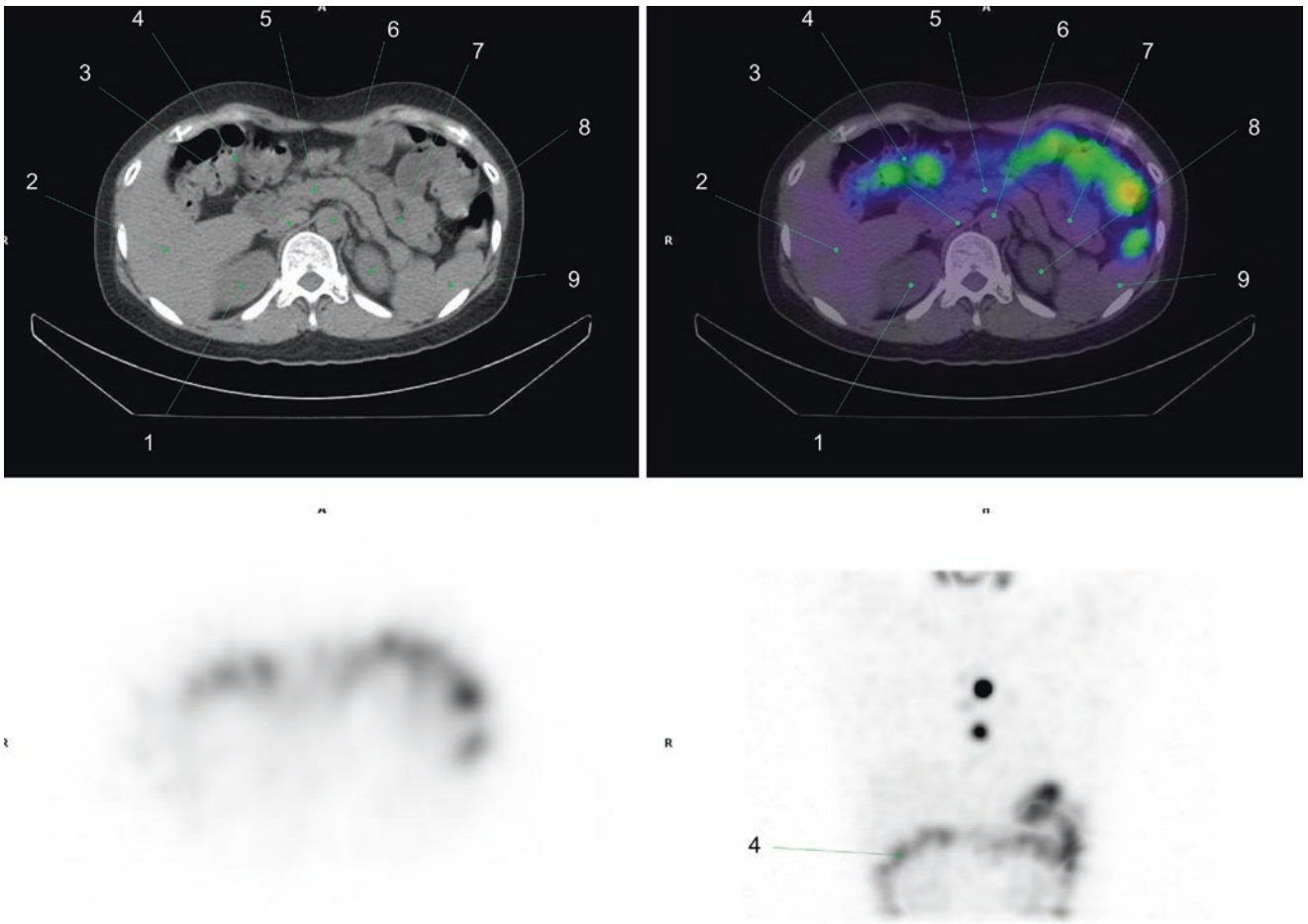

Fig. 29 1. Right kidney
2. Liver
3. Inferior vena cava
4. Transverse colon
5. Body of pancreas
6. Descending aorta
7. Jejunum
8. Left kidney
9. Spleen

1.6.3 Case 3

A 62-year-old female patient with thyroid cancer history, who was treated with thyroidectomy 6 months earlier. She attended a routine follow-up without symptoms and normal serum levels of thyroglobulin. Selected SPECT (*top*) and SPECT/CT (*bottom*) with ^{131}I demonstrated a focal area of moderately increased activity in the left thyroid bed, which was confirmed to be residual functioning thyroid tissue (Fig. 30).

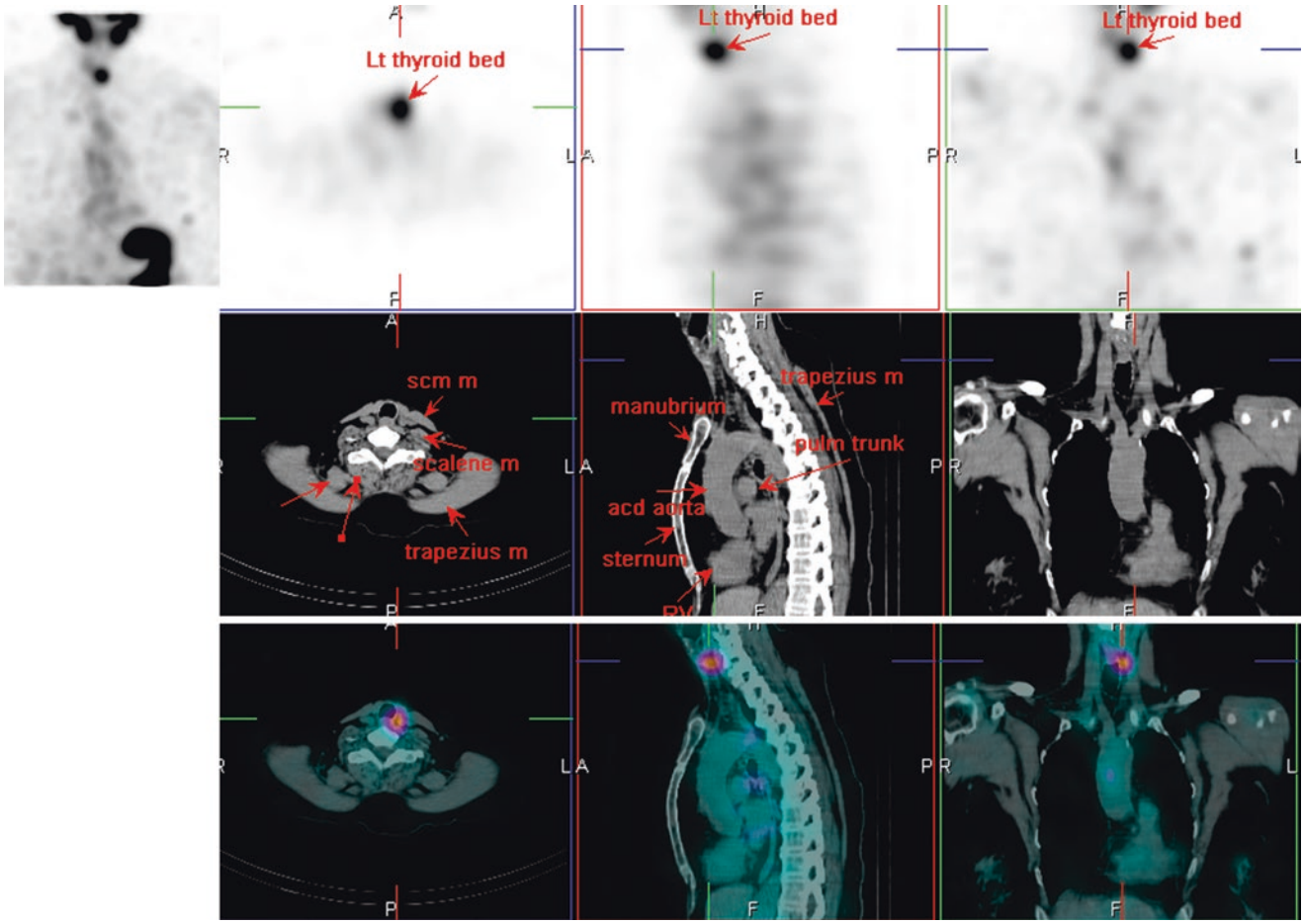

Fig. 30 ^{131}I SPECT/CT

1.7 Parathyroid Adenoma

1.7.1 Case 1

A 63-year-old male patient with hypercalcemia and weight loss. Laboratory tests showed abnormal serum calcium, phosphorus, and parathyroid hormone levels, so primary hyperparathyroidism was suspected. ^{99m}Tc-MIBI SPECT/CT was performed finding focal delayed uptake in the lower aspect of the right thyroid lobe, corresponding to a parathyroid adenoma, type E (Figs. 31, 32, 33, 34, and 35) [40, 41].

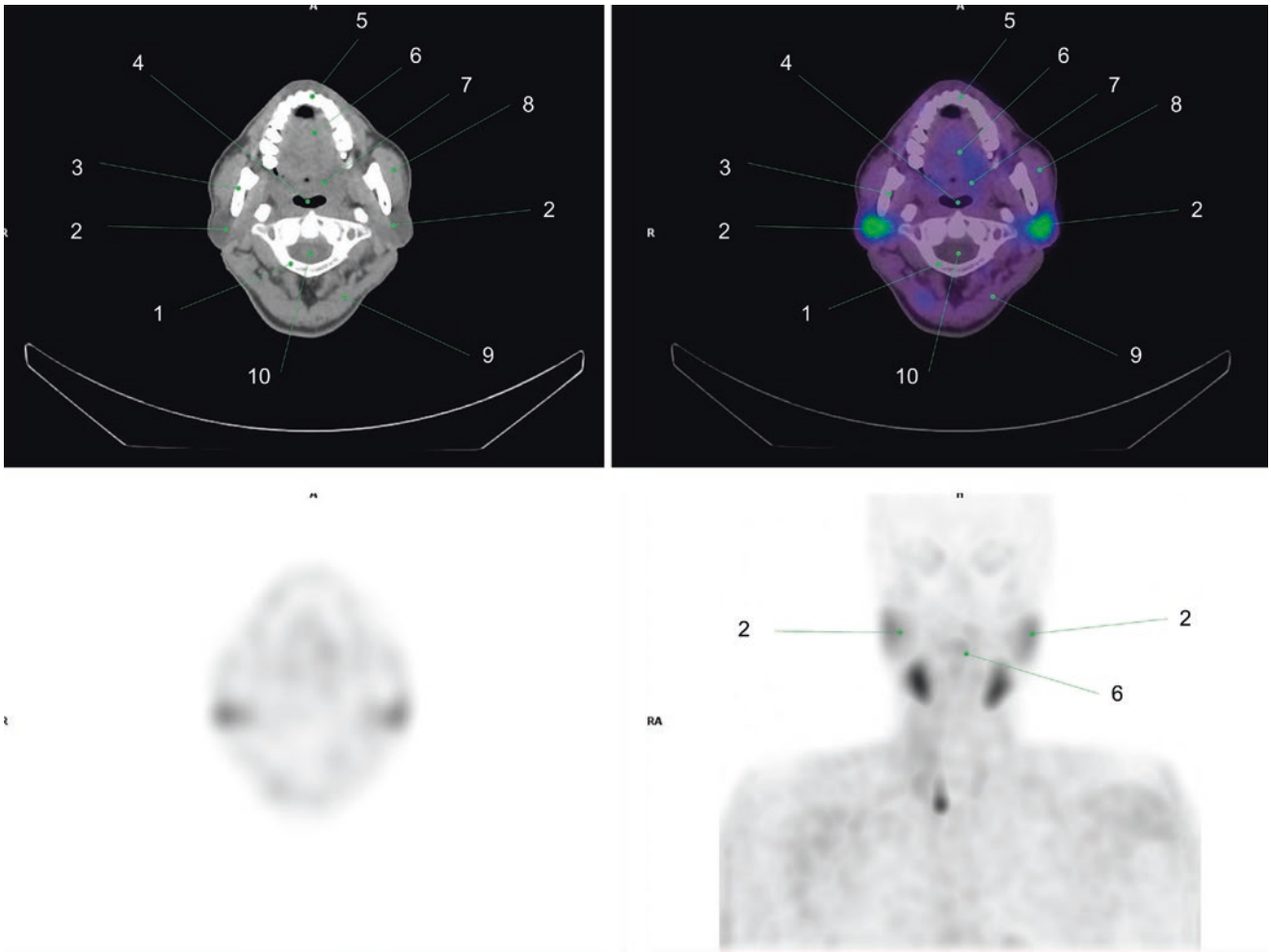

Fig. 31 1. Posterior arch of C1 spine
2. Parotid glands
3. Mandibular ramus
4. Pharyngeal space
5. Body of mandible
6. Body of tongue
7. Palatine tonsil
8. Masseter muscle (superficial part)
9. Trapezius muscle
10. Spinal cord

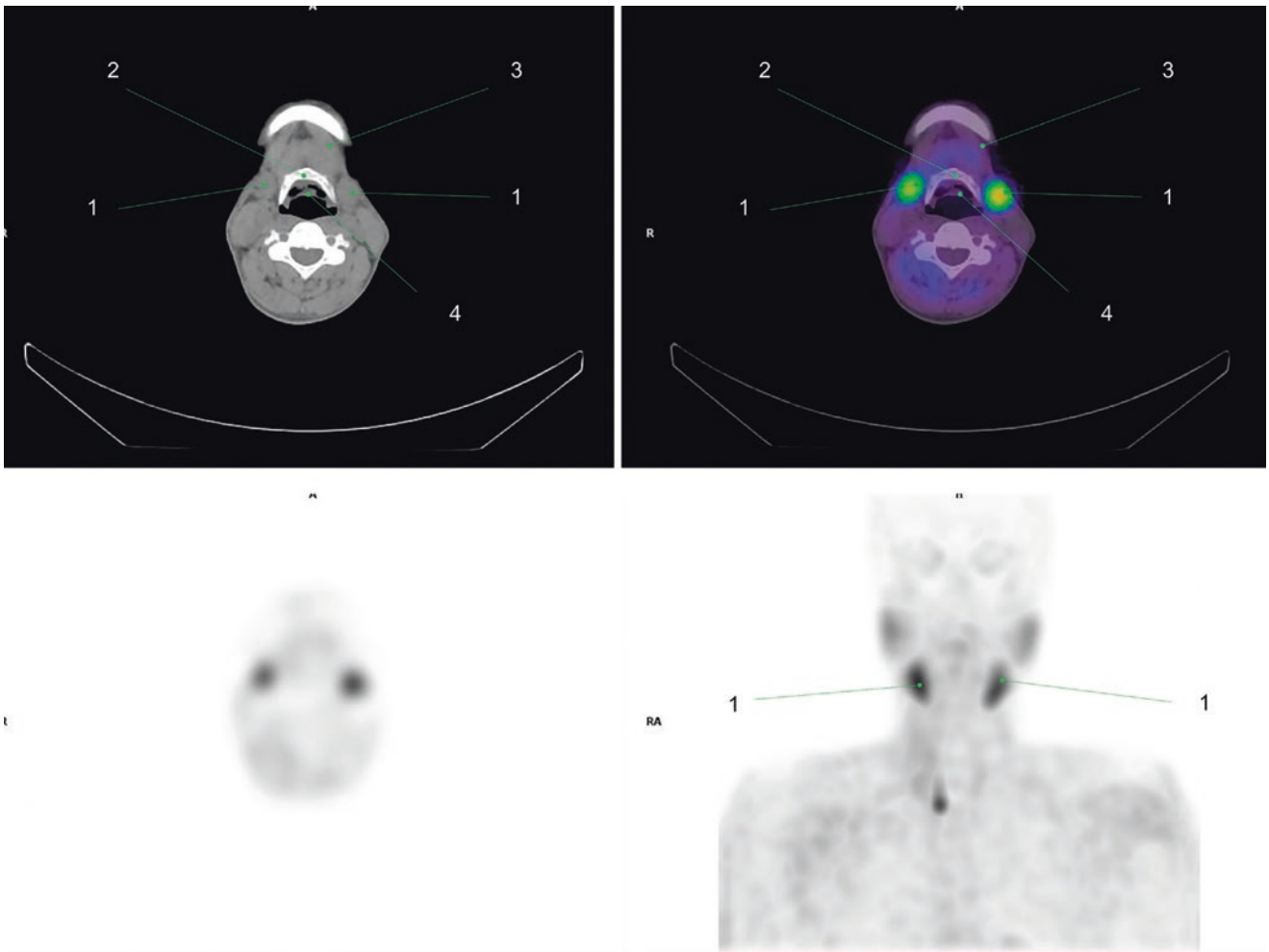

Fig. 32 1. Submandibular glands
2. Body of hyoid bone
3. Digastric muscle anterior belly
4. Epiglottis

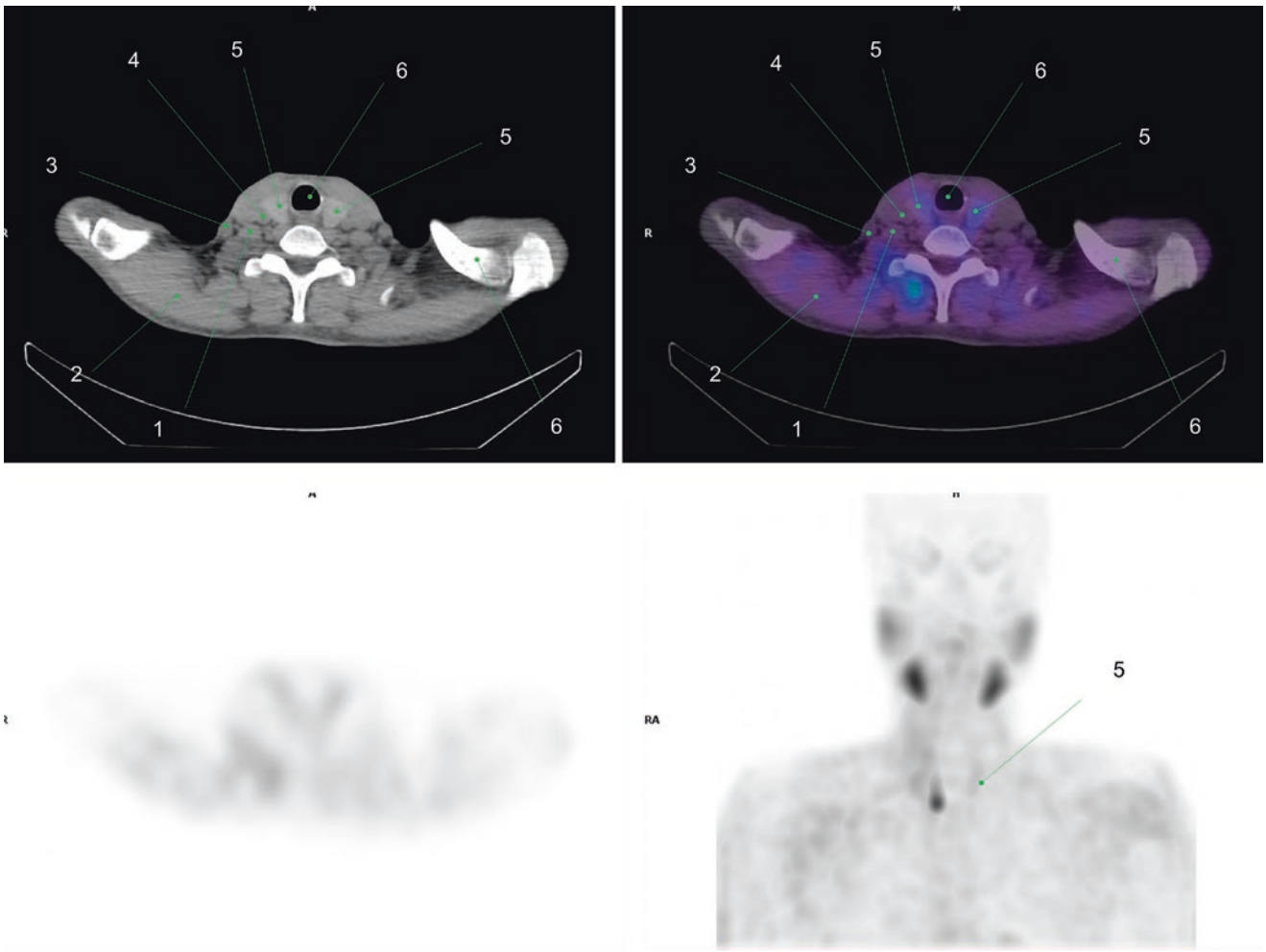

Fig. 33 1. Internal jugular vein
2. Trapezius muscle
3. External jugular vein
4. Common carotid artery
5. Thyroid gland
6. Trachea

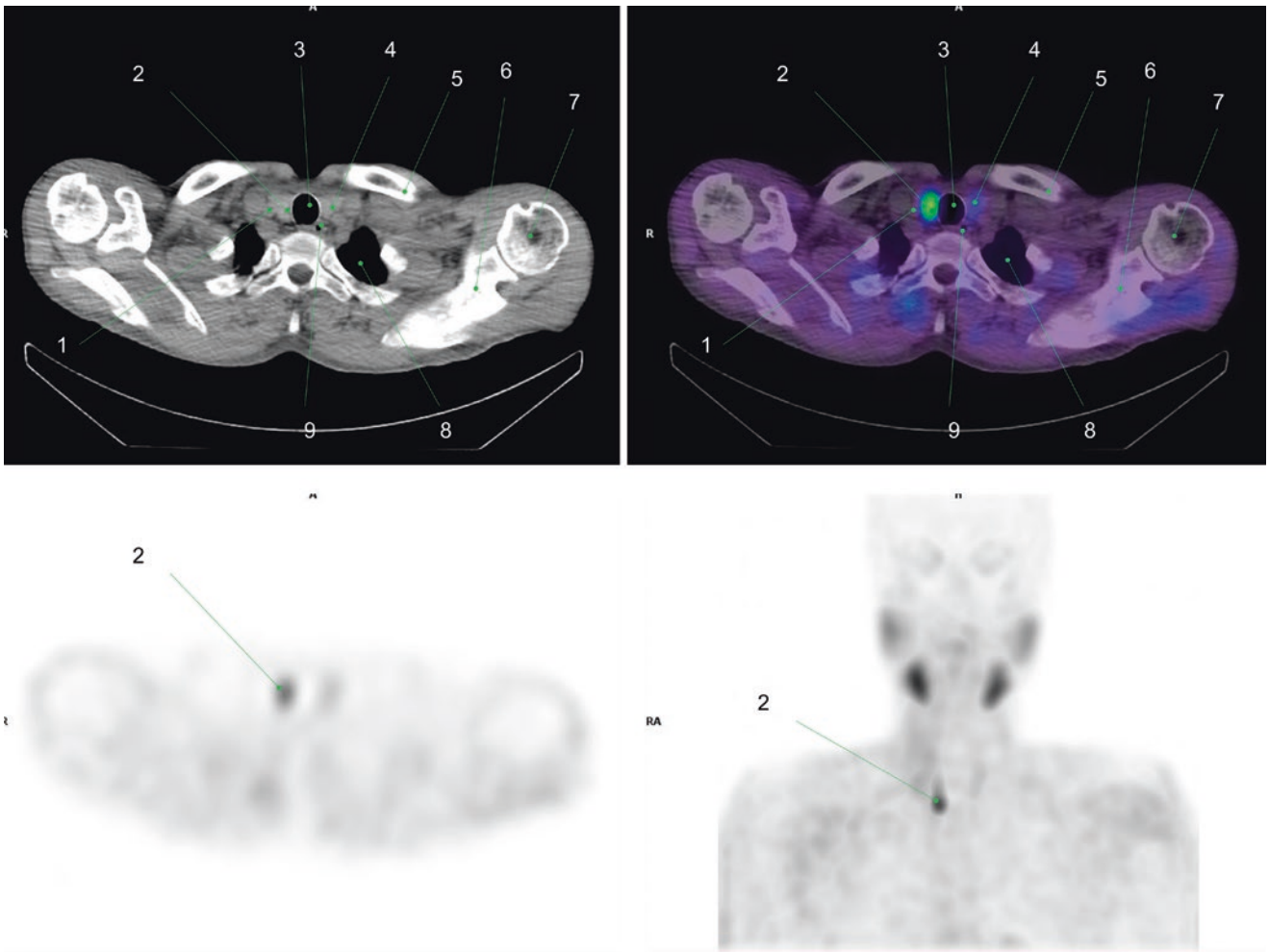

Fig. 34 1. Right common carotid artery
2. Parathyroid gland
3. Trachea
4. Thyroid Left lobe
5. Left clavicle
6. Left scapular
7. Head of left humerus
8. Left lung apex
9. Esophagus

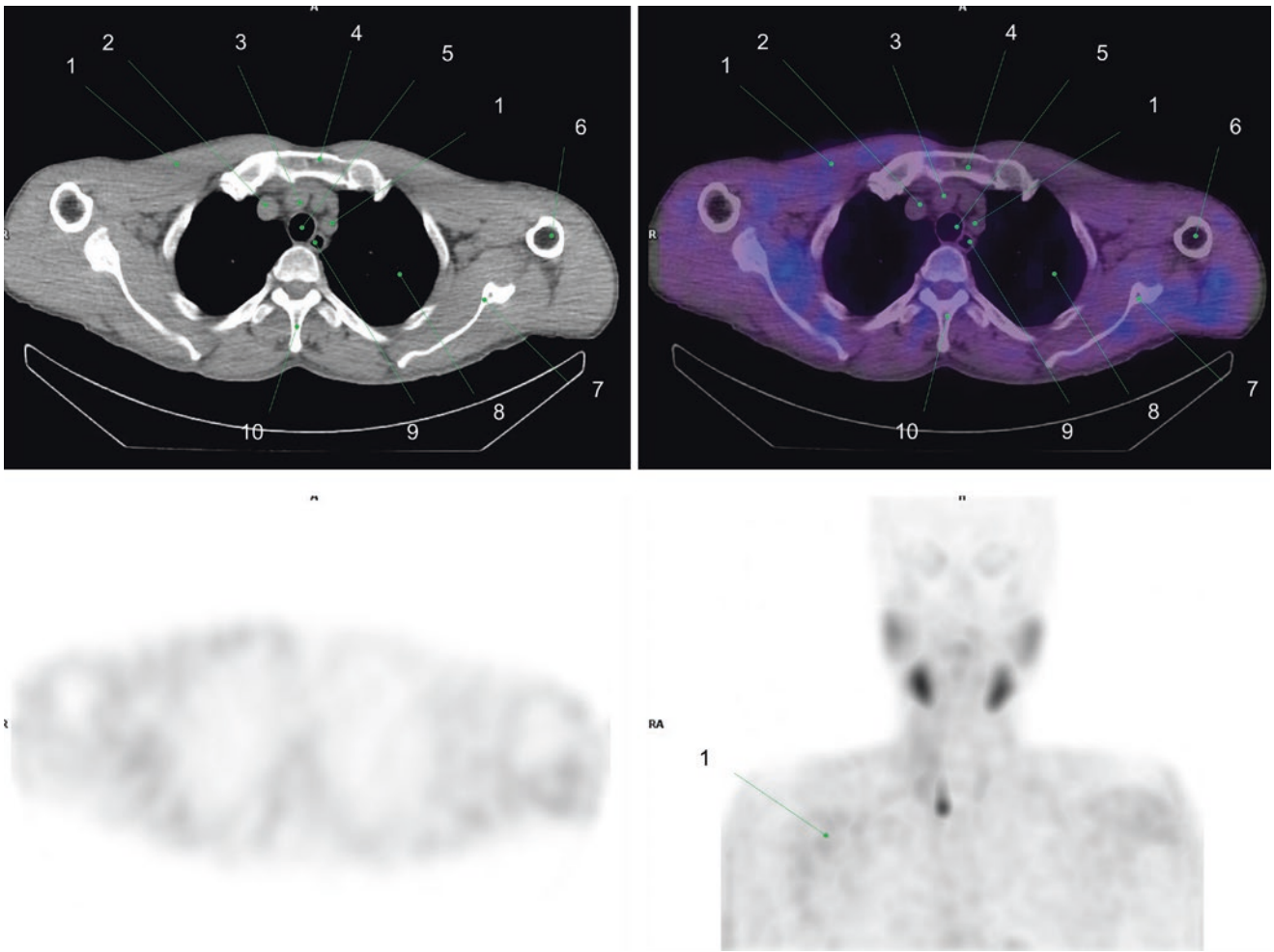

Fig. 35 1. Right pectoralis major muscle
2. Subclavian artery
3. Common carotid artery
4. Sternum
5. Trachea
6. Humeral shaft
7. Scapular
8. Left Lung
9. Esophagus
10. Spinous process of T3 spine

1.7.2 Case 2

A 63-year-old female patient with suspicion of parathyroid adenoma, who underwent ^{99m}Tc-MIBI SPECT/CT. Images showed a focal area of moderately increased activity in the right lower anterior mediastinum, which was confirmed as a parathyroid adenoma, type F (Fig. 36) [42].

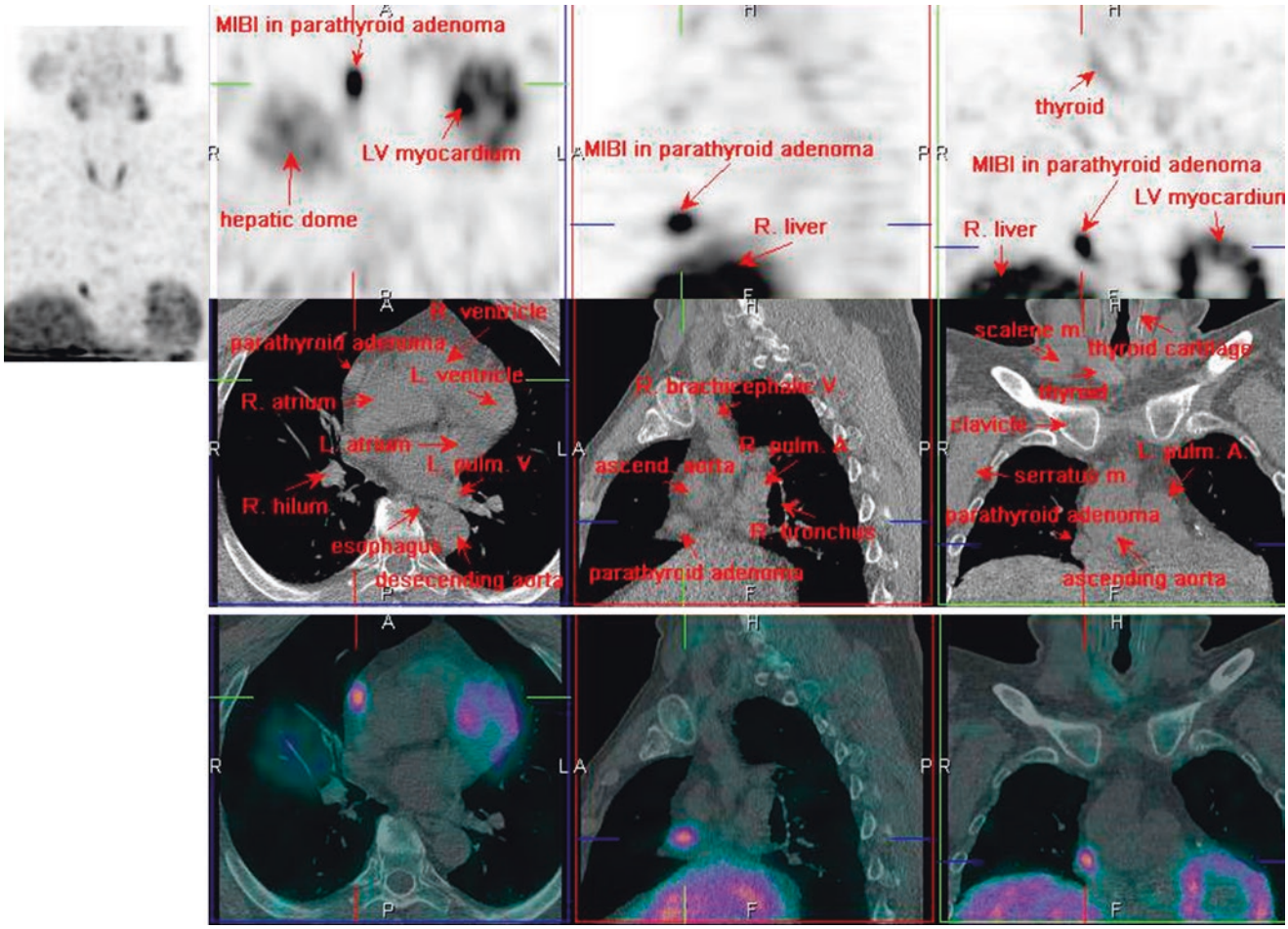

Fig. 36 ^{99m}Tc-MIBI SPECT/CT

1.7.3 Case 3

A 71-year-old female patient with primary hyperparathyroidism, who underwent ^{99m}Tc-MIBI SPECT/CT. Images showed a focal moderately increased activity in the right paraesophageal area at the level of the thoracic inlet, which corresponded to a parathyroid adenoma, type F (Fig. 37) [42].

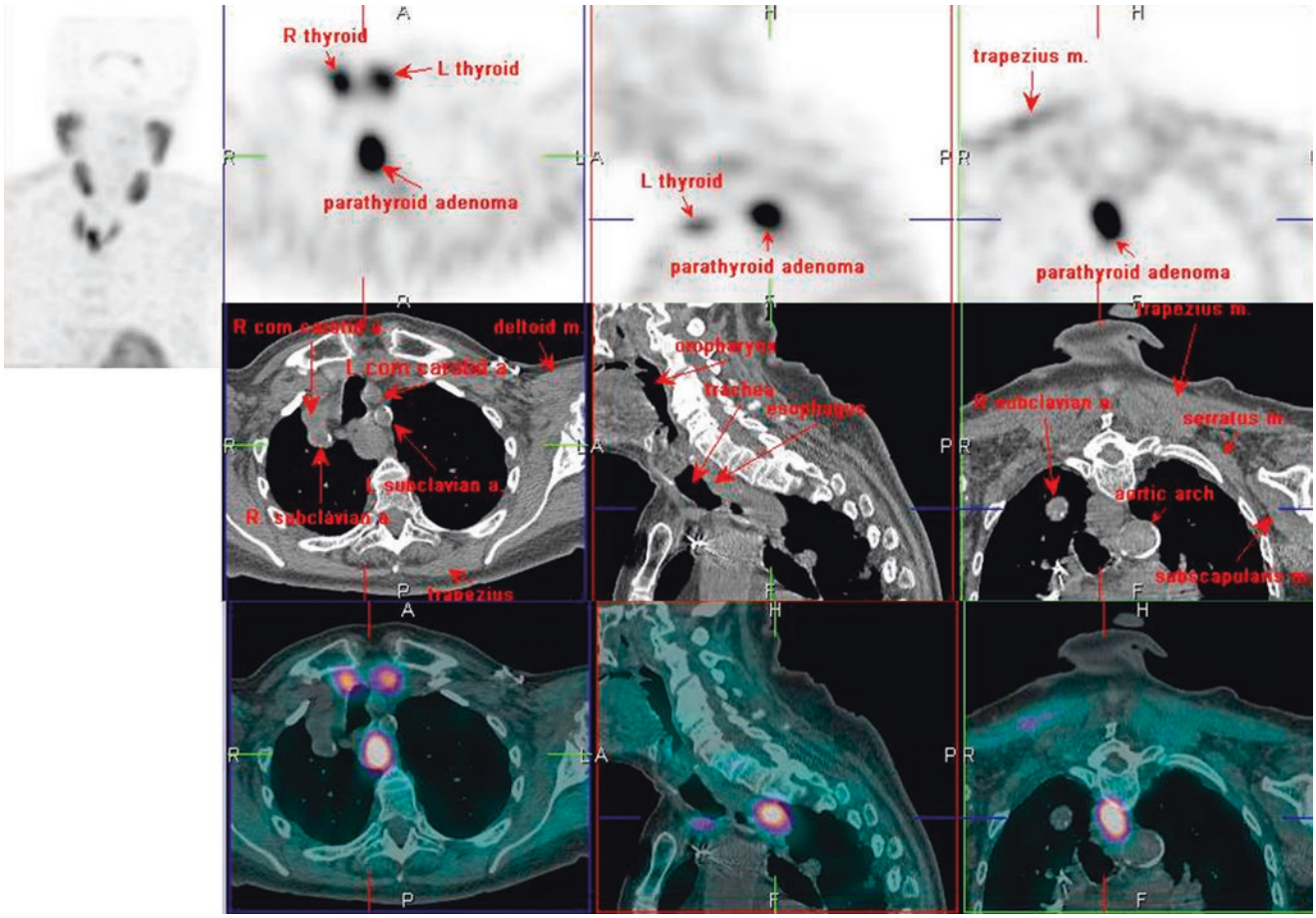

Fig. 37 ^{99m}Tc-MIBI SPECT/CT

1.7.4 Case 4

A 56-year-old male patient with confirmed diagnosis of a parathyroid adenoma (type E). Selected SPECT (*top*) and SPECT/CT (*bottom*) of the neck and chest with ^{99m}Tc-MIBI were performed. Images showed a focal moderately increased activity in the right paratracheal area at the level of the right inferior thyroid bed (Fig. 38) [42].

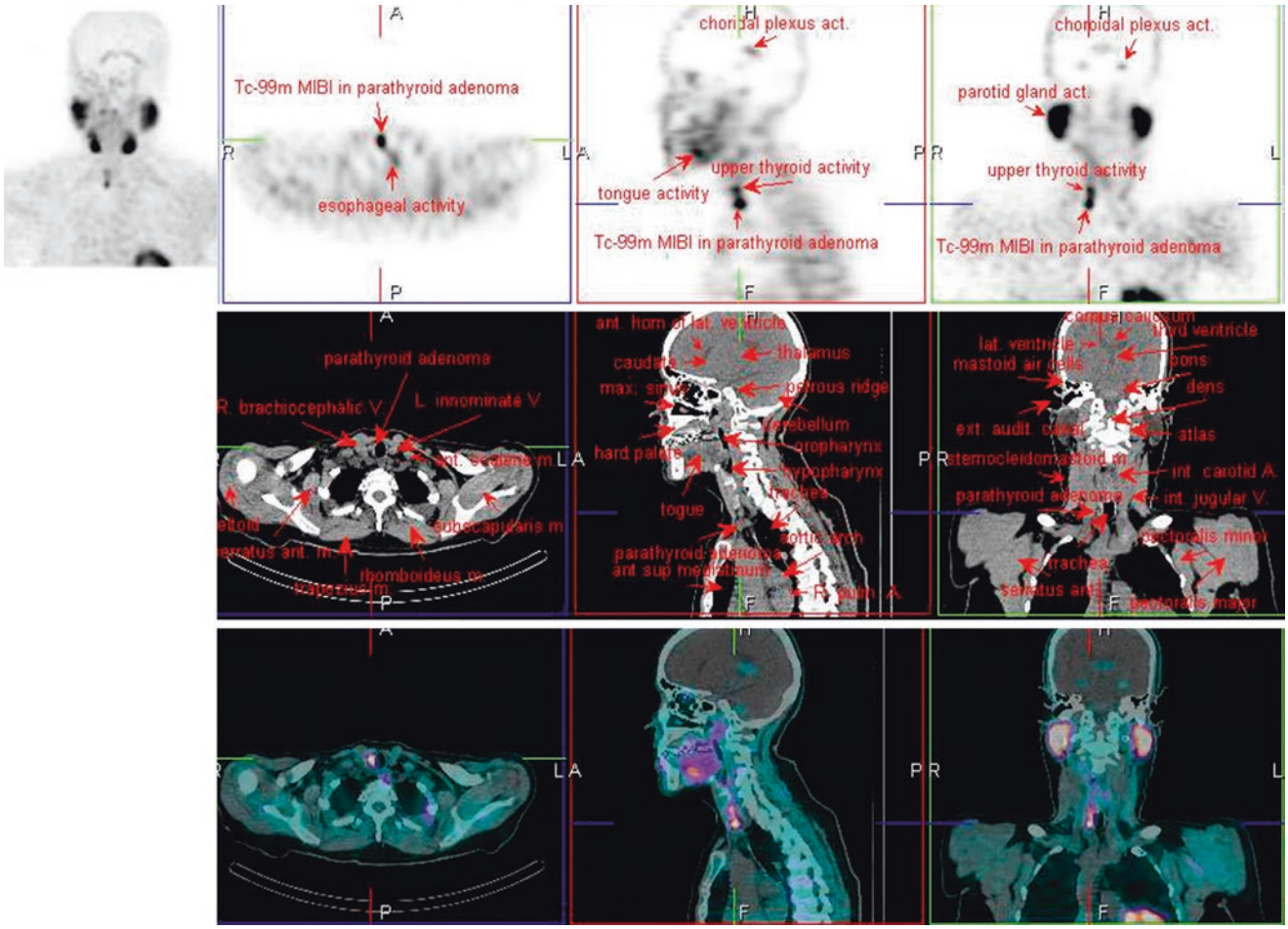

Fig. 38 ^{99m}Tc-MIBI SPECT/CT

1.7.5 Case 5

A 63-year-old female patient with suspicion of a parathyroid adenoma (type C). Selected SPECT (top) and SPECT/CT images of the neck and chest with ^{99m}Tc-MIBI showed a focal moderately increased activity in the right paraesophageal area, confirming the diagnosis (Fig. 39) [42].

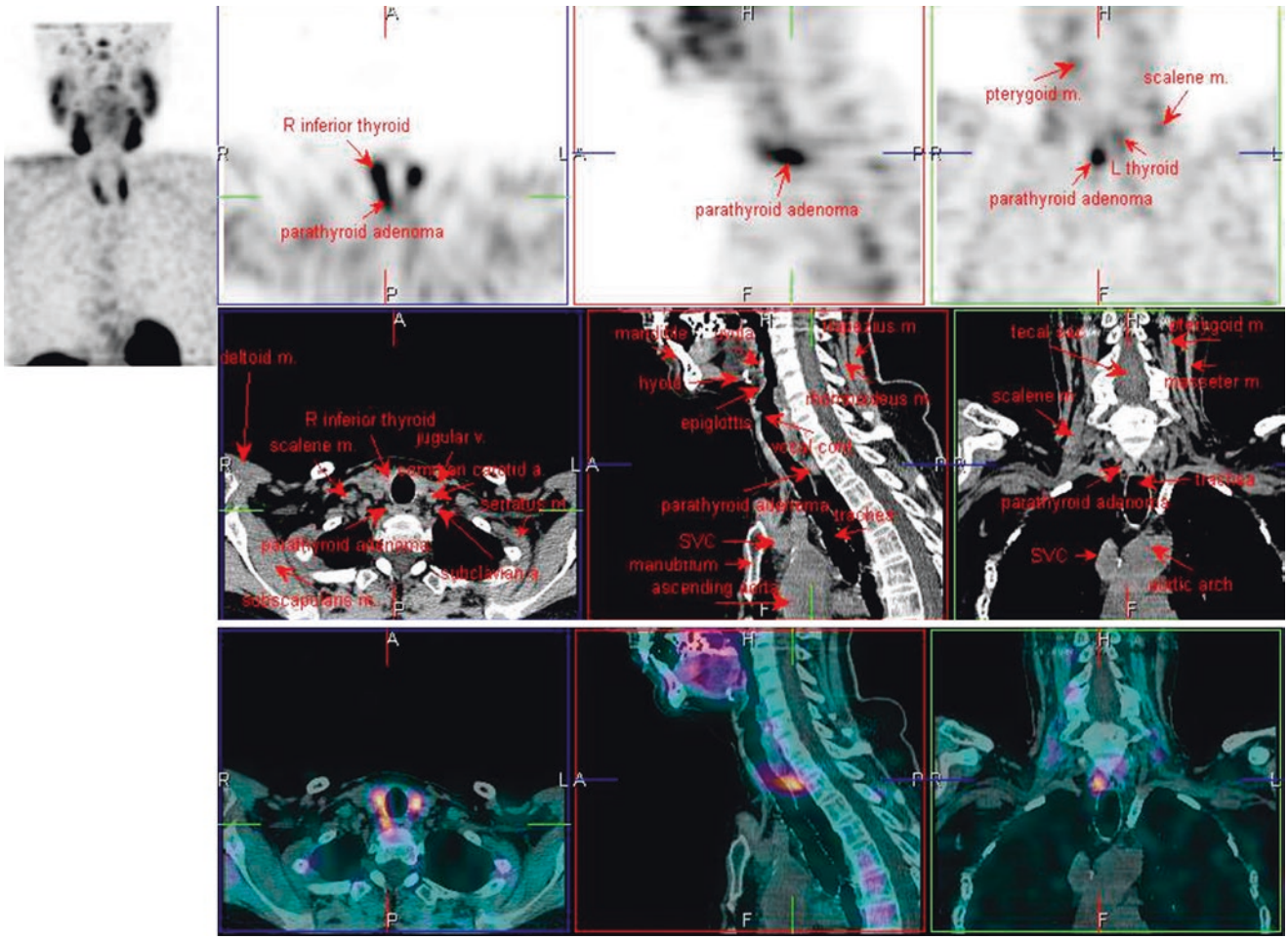

Fig. 39 ^{99m}Tc-MIBI SPECT/CT

1.8 Mesothelioma

1.8.1 Case 1

A 69-year-old male patient with chest pain and dyspnea. The diagnosis of a mesothelioma was confirmed and ^{99m}Tc-MAA SPECT/CT was performed during staging. Images showed slightly decreased activity in the right upper and middle lobes as well as moderately decreased activity in the right lower lobe. Also noted were perfusion defects along the posterolateral periphery of the right lower lobe owing to nodular pleural lesions (Fig. 40) [43].

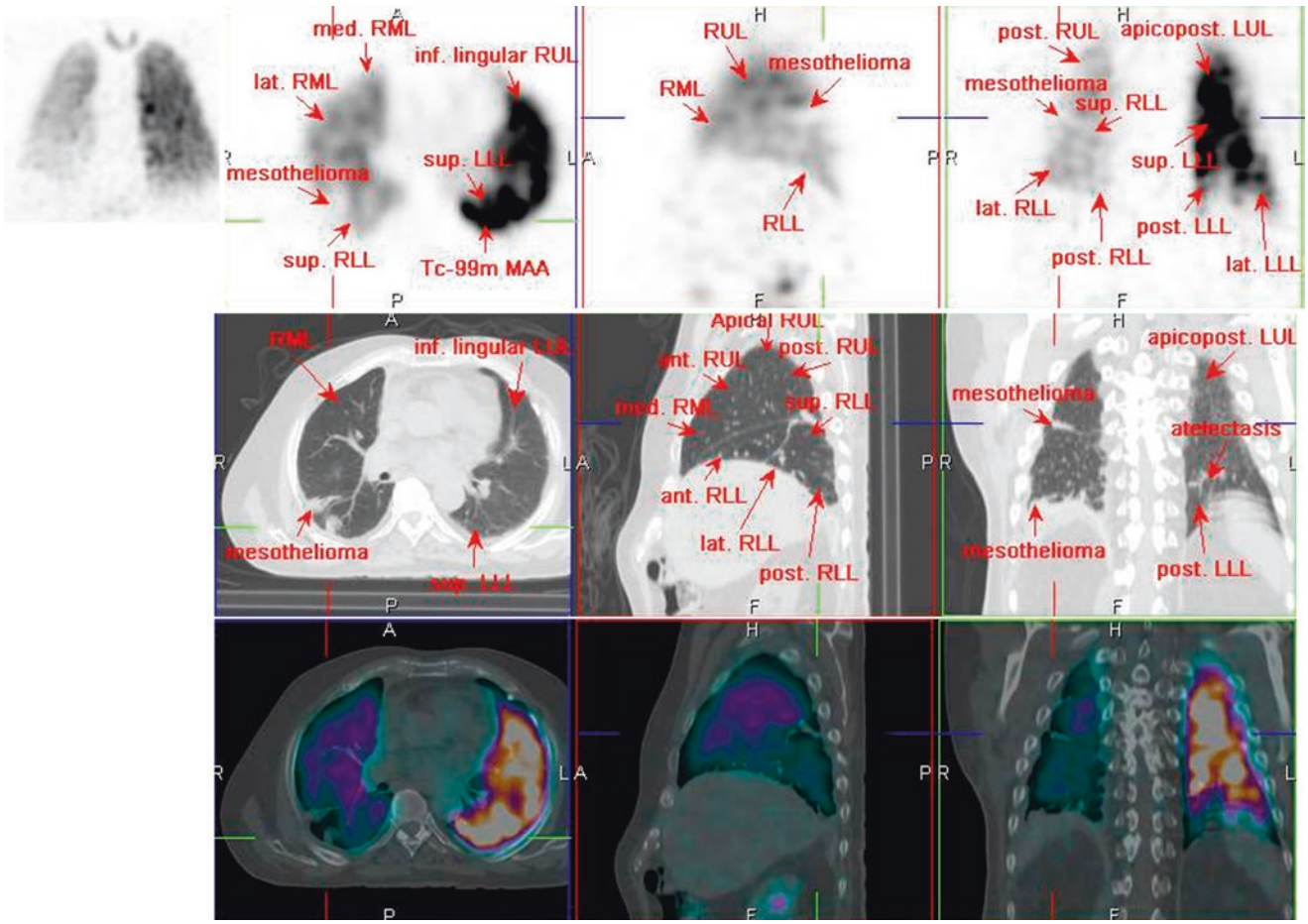

Fig. 40 ^{99m}Tc-MAA SPECT/CT

1.9 Bone Tumors

1.9.1 Case 1

A 10-year-old girl with a history of ossifying fibroma, who underwent ^{99m}Tc-methylene diphosphonate (MDP) SPECT/CT during a follow-up. Images showed moderately increased activity in the bilateral maxillary sinuses and right mandible at expansile bone lesions with fibrous matrix and peripheral sclerotic rim. Ossifying fibromas are benign bone tumors and occur often in children under 10 years in the tibia, femur, mandible, maxilla, and nasal areas (Fig. 41) [45].

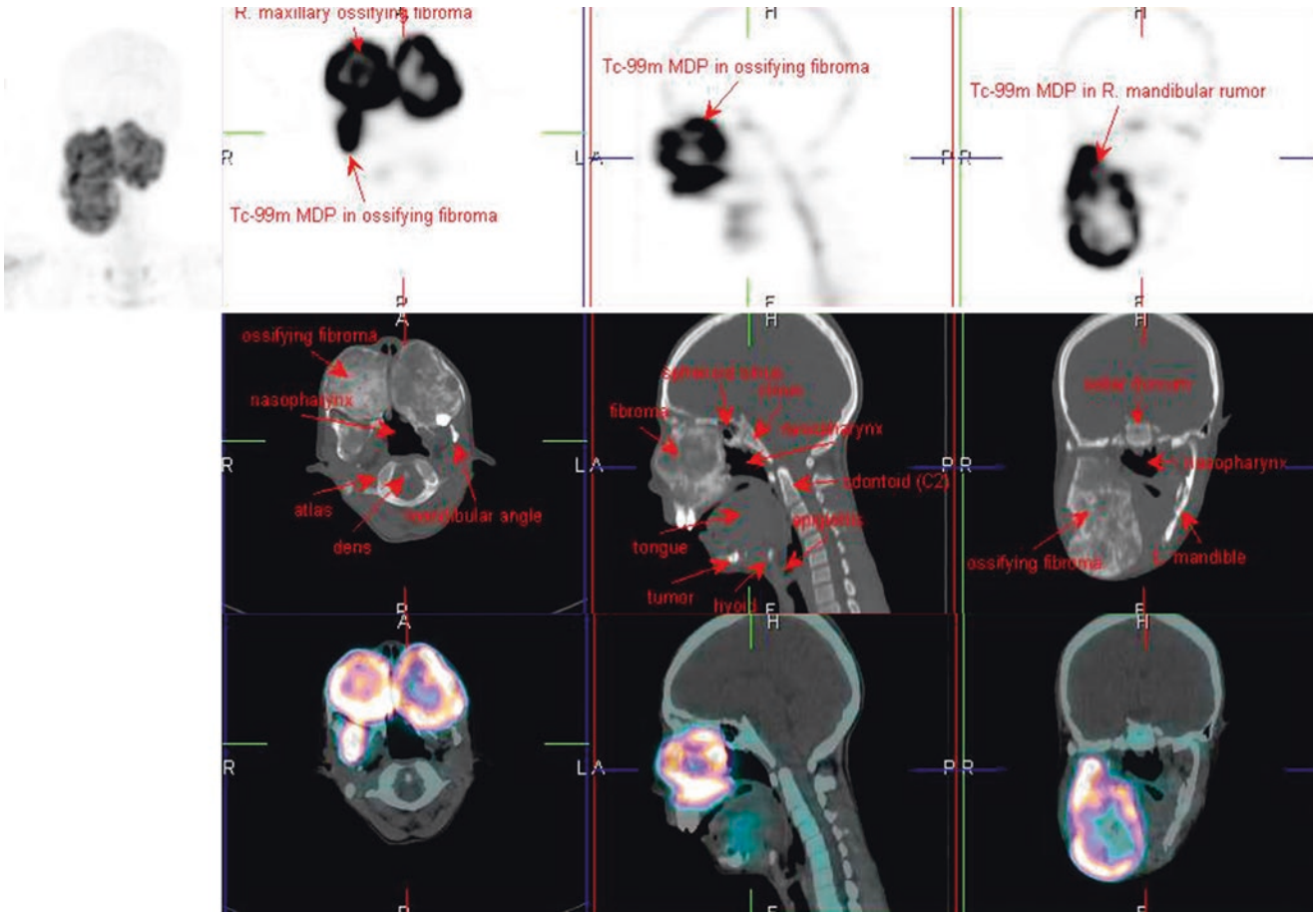

Fig. 41 ^{99m}Tc-MDP SPECT/CT

1.9.2 Case 2

A 76-year-old male patient with lower back pain. ^{99m}Tc-MDP SPECT/CT showed focal increased uptake at bilateral L5-S1 facet joints, with degenerative changes. Additionally, a focal increased uptake was noted at the superior aspect of the left iliac bone, corresponding to a non-aggressive bone lesion with a central hipodense nidus surrounded by sclerotic bone changes, which was confirmed to be an osteoid osteoma (Fig. 42).

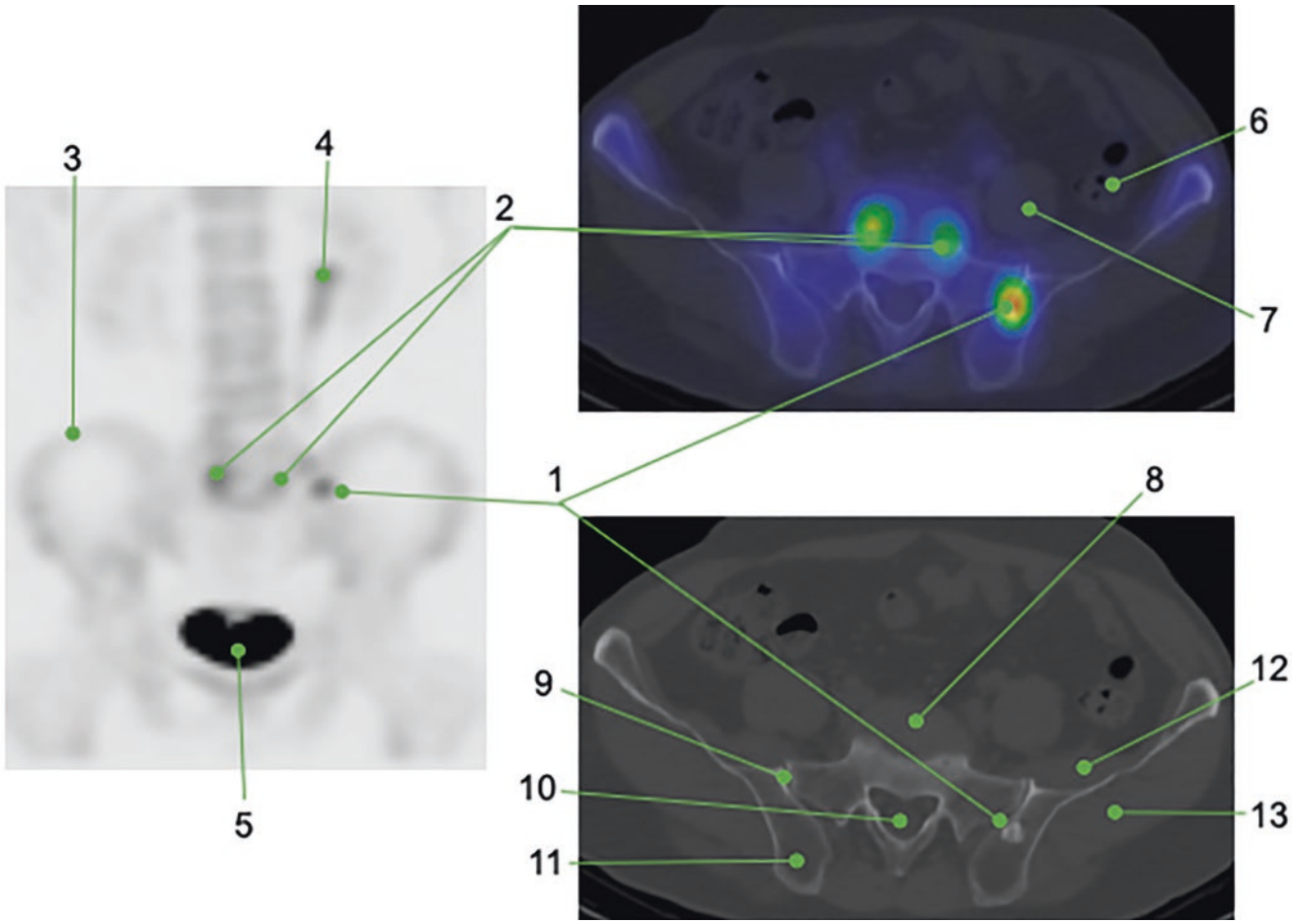

Fig. 42 1. Focal increased uptake at left iliac osteoid osteoma
2. Focal increased uptake at both L5-S1 facet joints degenerative changes
3. Right iliac crest
4. Left renal pelvis and proximal ureter
5. Bladder
6. Descending colon
7. Left psoas muscle
8. L5-S1 intervertebral disc
9. Right sacroiliac joint
10. Sacral canal
11. Right iliac tuberosity
12. Left iliacus muscle
13. Left gluteus maximus muscle

1.10 Bone Metastases

1.10.1 Case 1

A 38-year-old female patient with a history of breast cancer, who attended with right shoulder pain. ^{99m}Tc-MDP SPECT/CT was done, finding focal moderately increased activity in the right scapular body, caused by metastasis. Bone metastases are over ten times more common than primary bone tumors. Most metastases occur in the red bone marrow, most commonly in the axial skeleton. Osteoblastic metastases often occur with prostate cancer, transitional cell carcinoma, mucinous tumor, and carcinoid, whereas lytic metastases mostly occur with lung, thyroid, and renal cancers. Breast, stomach, and colon cancers can show osteolytic or osteoblastic lesions (Fig. 43) [46].

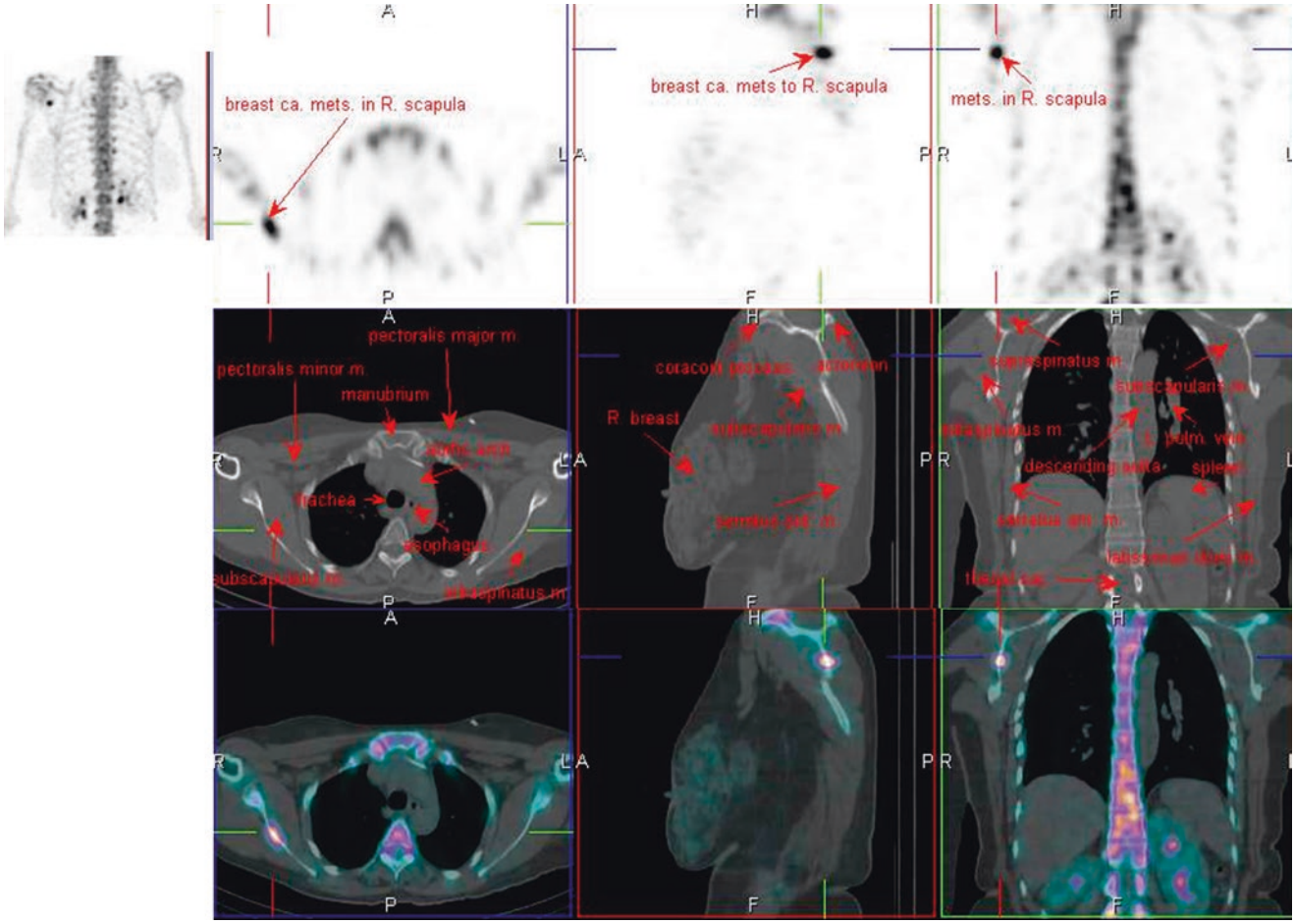

Fig. 43 ^{99m}Tc-MDP SPECT/CT

1.10.2 Case 2

A 65-year-old female patient with a history of breast cancer, who attended due to right knee pain without previous trauma. ^{99m}Tc-MDP SPECT/CT showed markedly increased activity in the lateral posterior condyle of the right distal femur at a mixed lytic and blastic bone lesion, consistent with bone metastasis (Fig. 44).

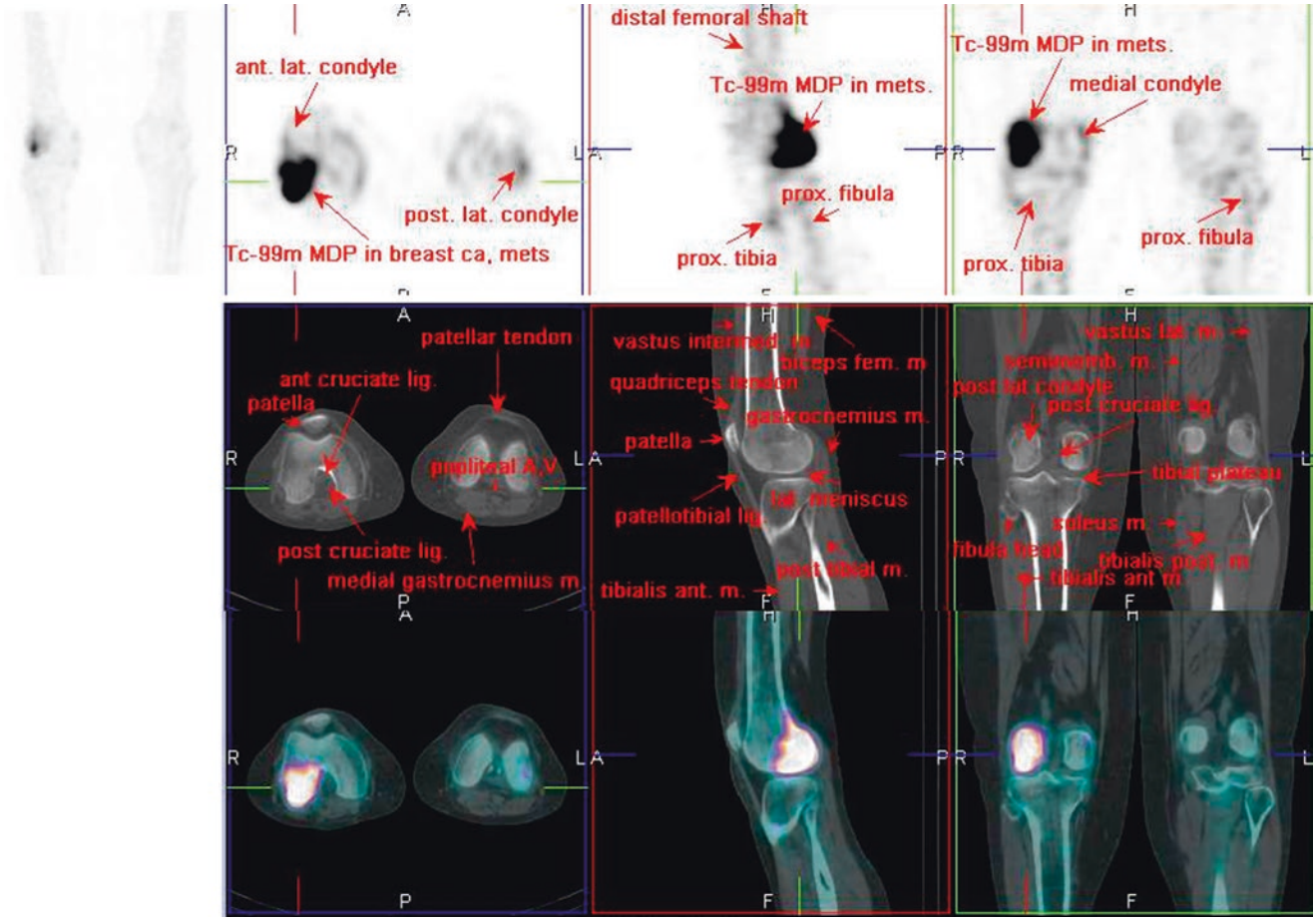

Fig. 44 ^{99m}Tc-MDP SPECT/CT

1.10.3 Case 3

A 47-year-old female patient with a history of breast cancer presented with pain in the lower back. Selected SPECT (*top*) and SPECT/CT (*bottom*) images of the pelvis with ^{99m}Tc-MDP showed markedly increased activity in the left sacral ala, abutting the sacroiliac joint (Fig. 45).

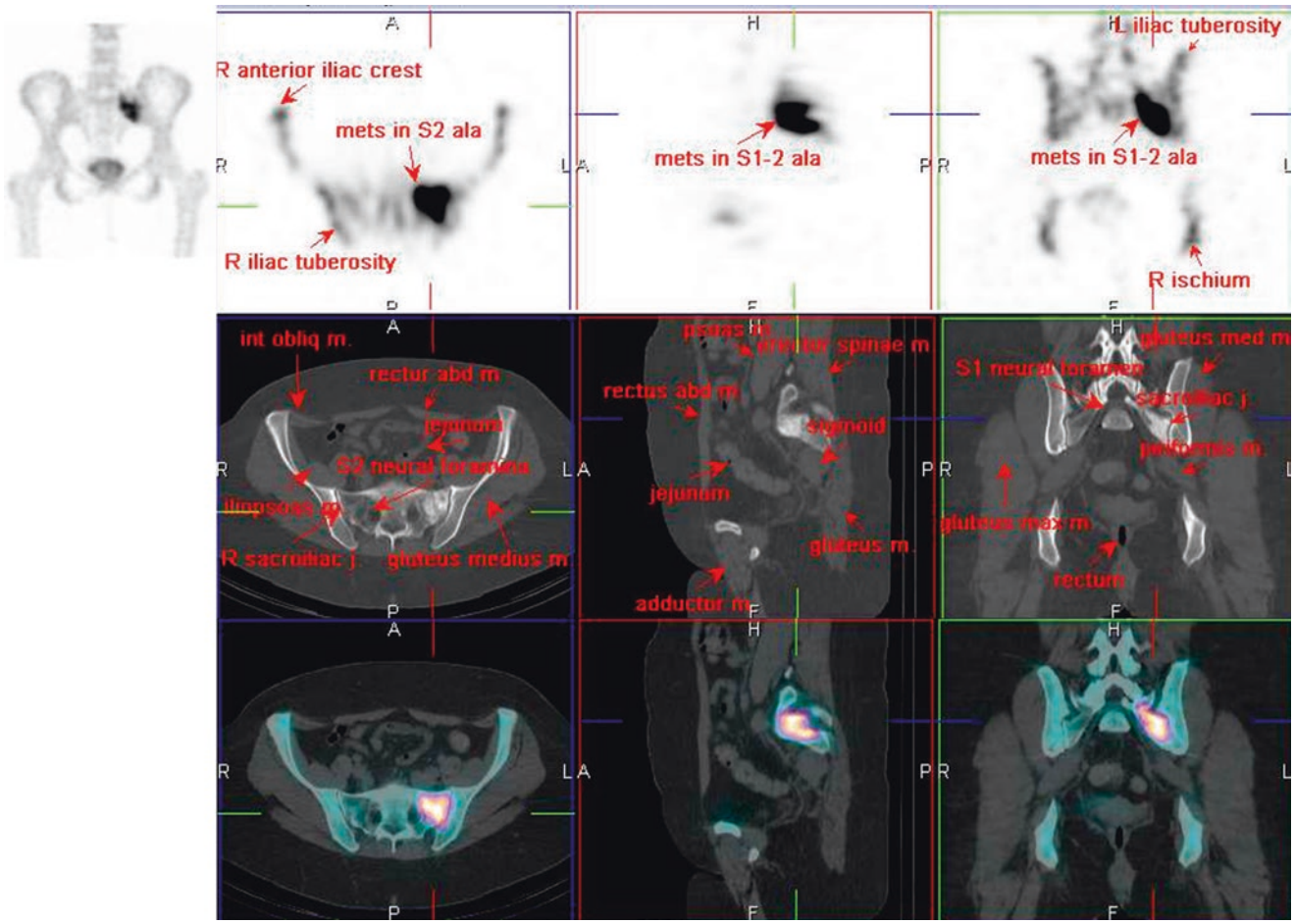

Fig. 45 ^{99m}Tc-MDP SPECT/CT

1.10.4 Case 4

A 66-year-old female patient with a history of non-Hodgkin lymphoma. She attended an early checkup due to lower back pain. ^{99m}Tc-MDP SPECT/CT was performed, finding focal areas of slightly increased activity in the bilateral iliac alae and tuberosities as well as L3-S1 vertebral bodies. Biopsy confirmed active lymphoma involvement (Fig. 46).

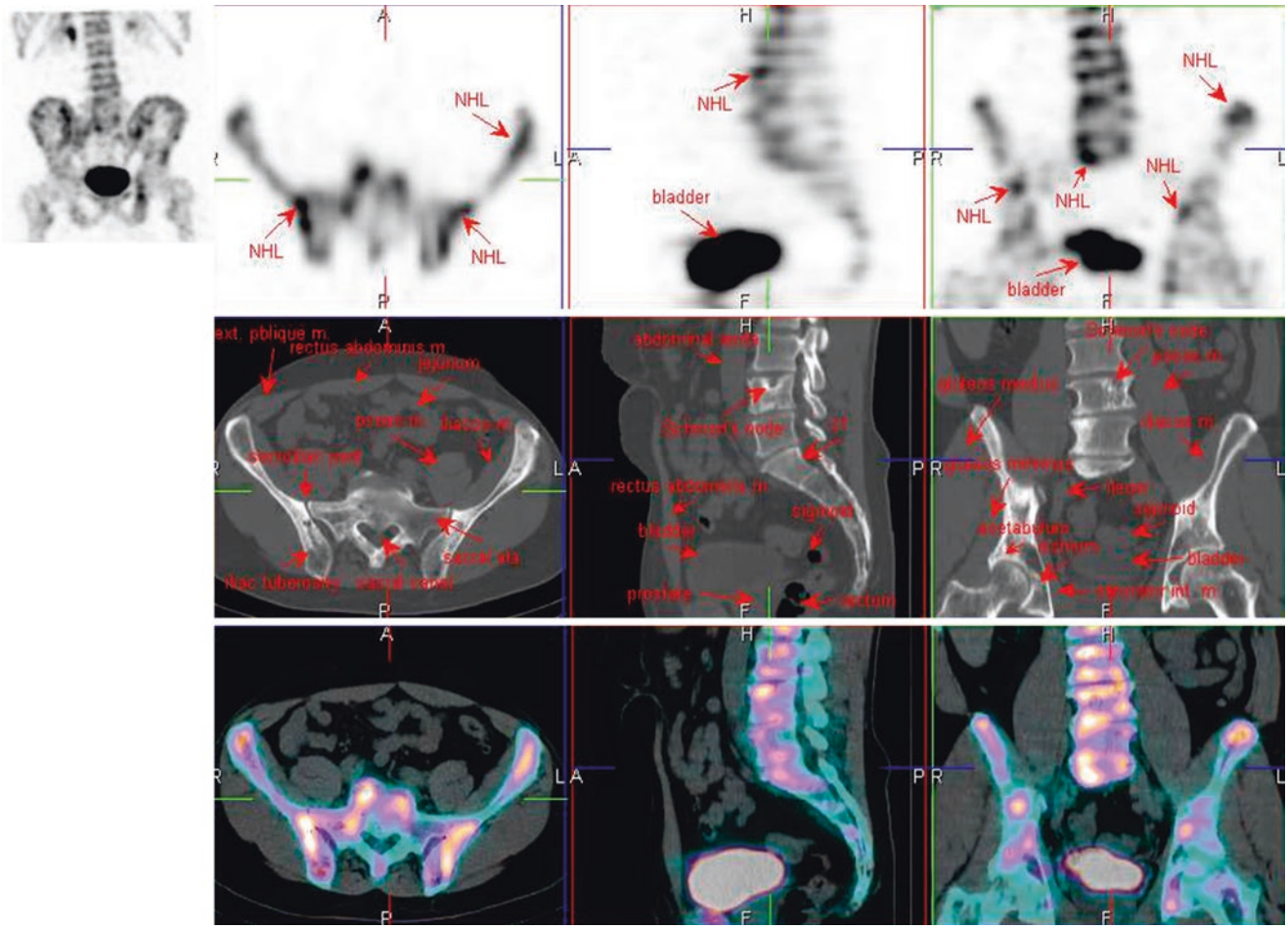

Fig. 46 ^{99m}Tc-MDP SPECT/CT

2 Non-Tumorous Conditions

2.1 Bone

2.1.1 Case 1

A 71-year-old female patient with chronic right knee pain. The clinical diagnosis was a medial meniscus tear in the right knee, and ^{99m}Tc-MDP SPECT/CT was done for further evaluation. Focal increased uptake was found in the right medial meniscus area, confirming the clinical diagnosis and associated changes in the subjacent bone (Figs. 47, 48, 49, and 50) [49].

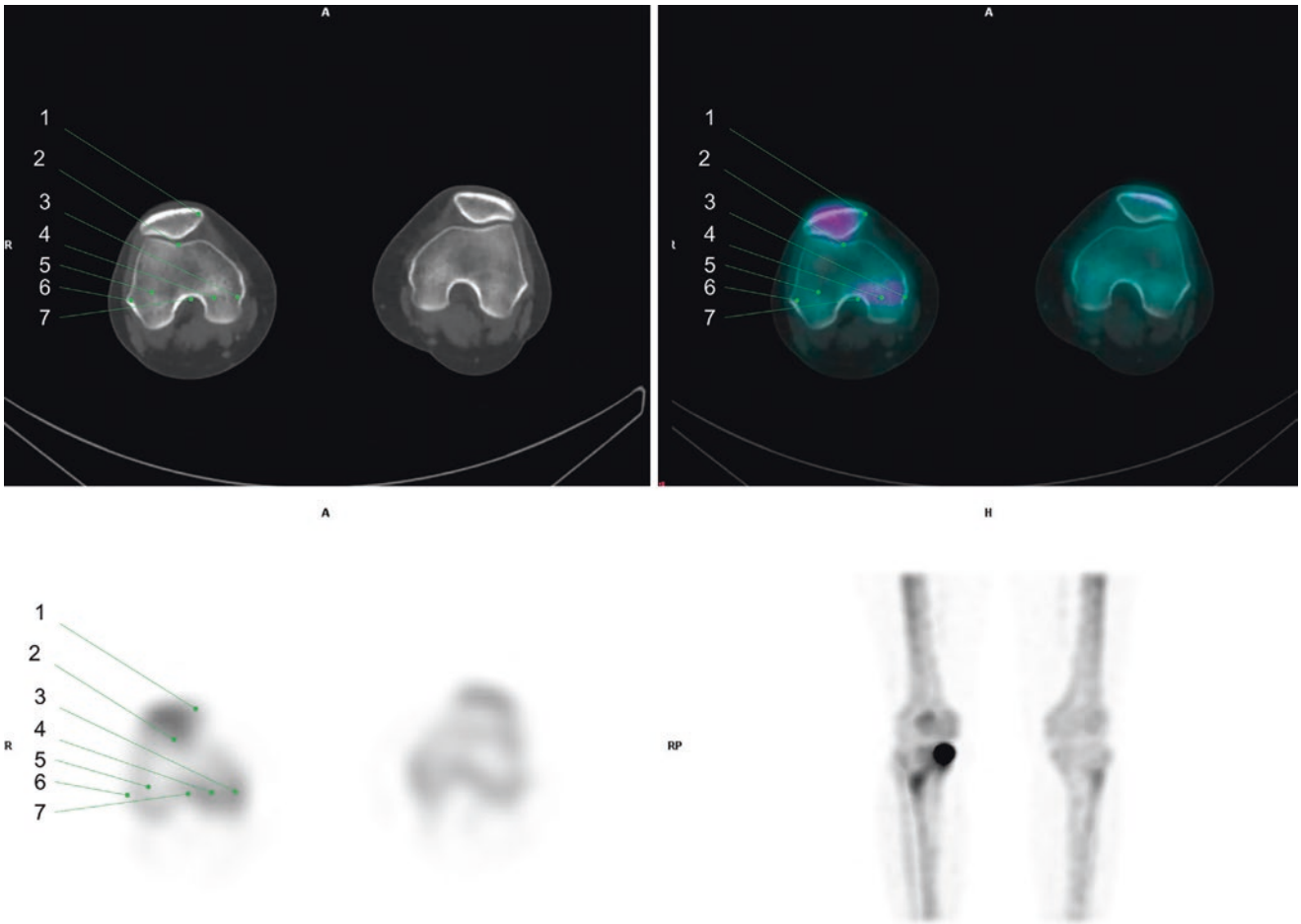

Fig. 47 1. Patella
2. Articular surface
3. Right medial epicondyle
4. Right medial condyle
5. Right lateral condyle
6. Right lateral epicondyle
7. Intercondylar fossa

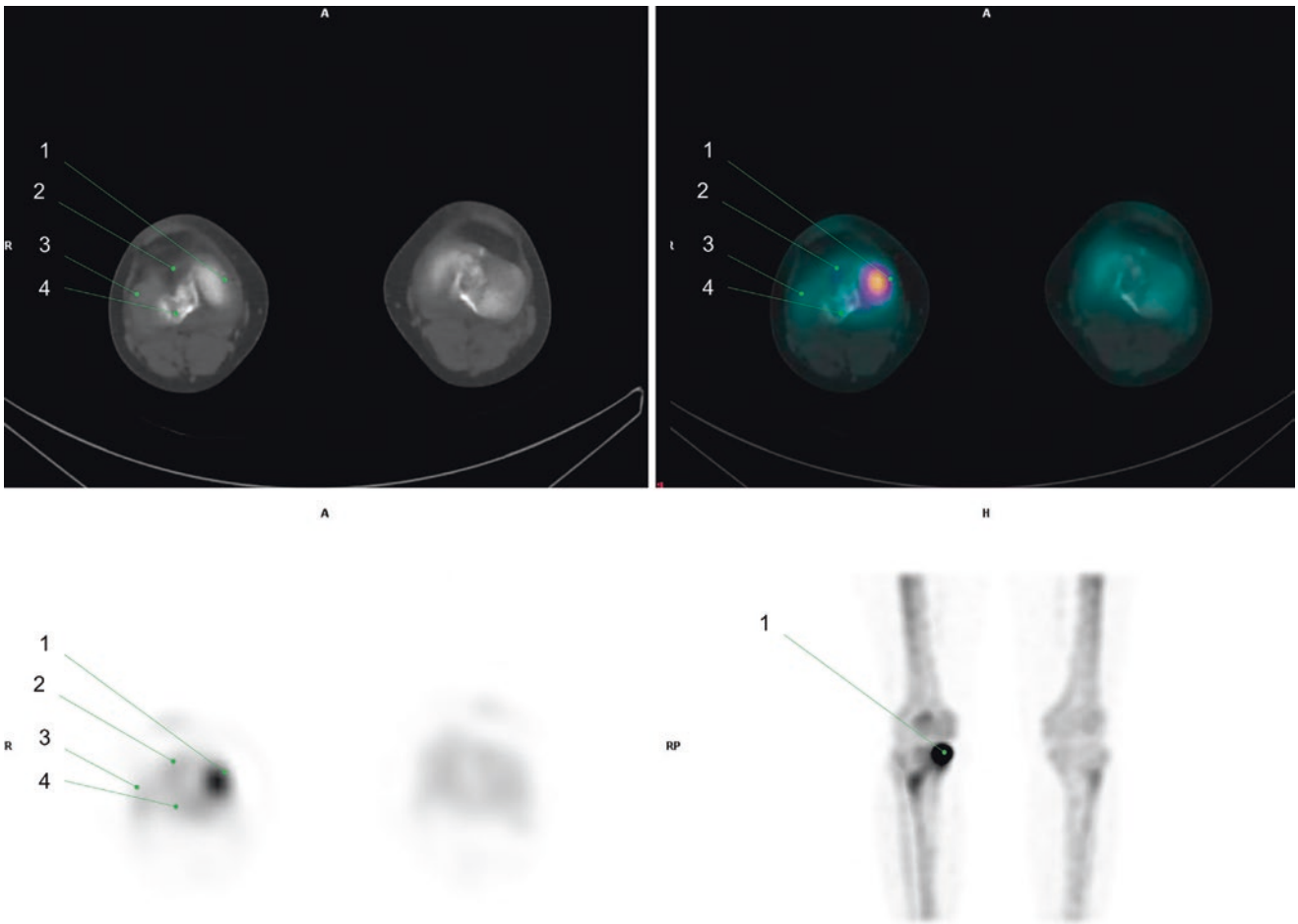

Fig. 48 1. Right medial condyle
2. Anterior intercondylar area
3. Superior articular surface
4. Posterior intercondylar

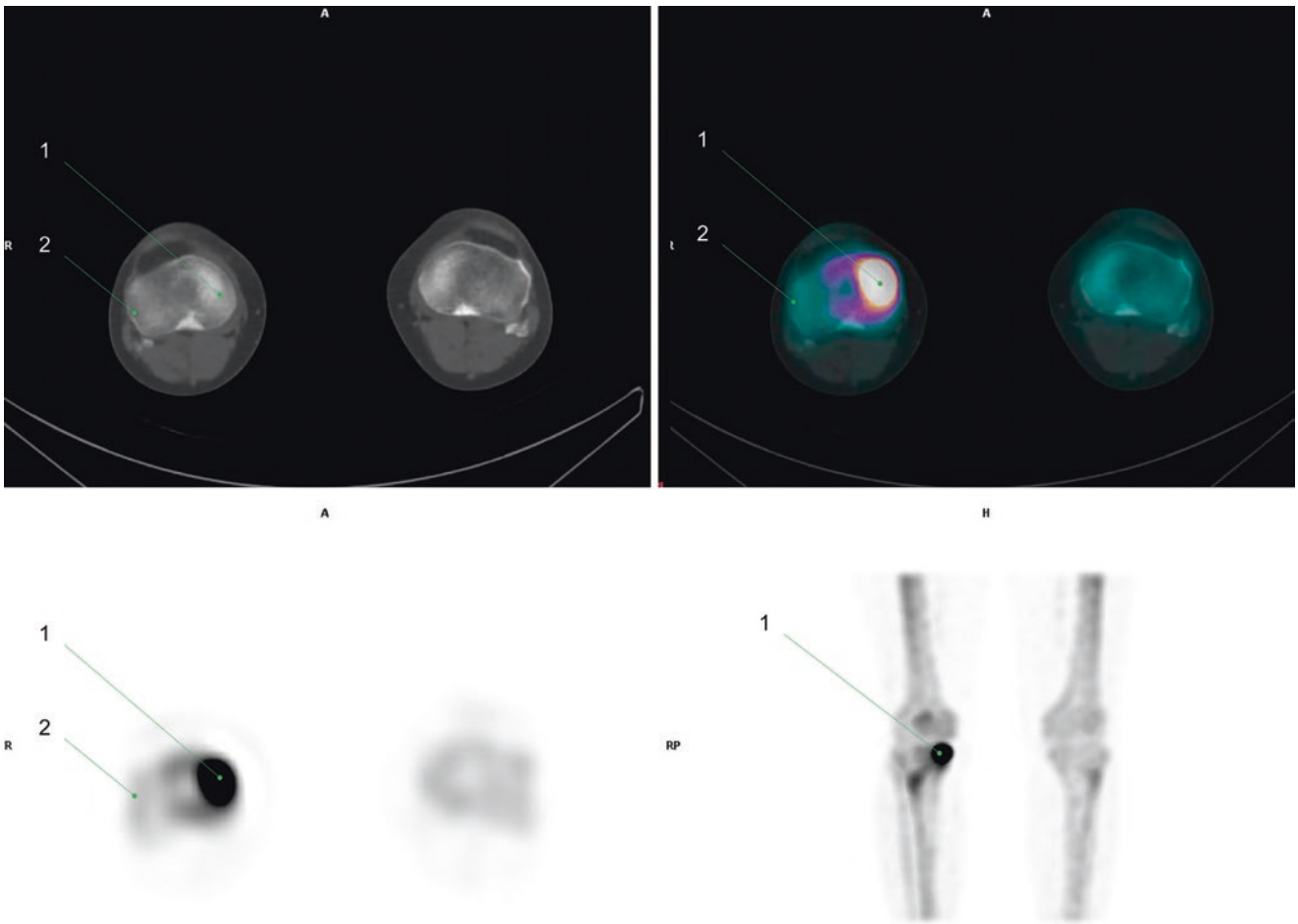

Fig. 49 1. Active lesion at right medial meniscus
2. Right tibial lateral condyle

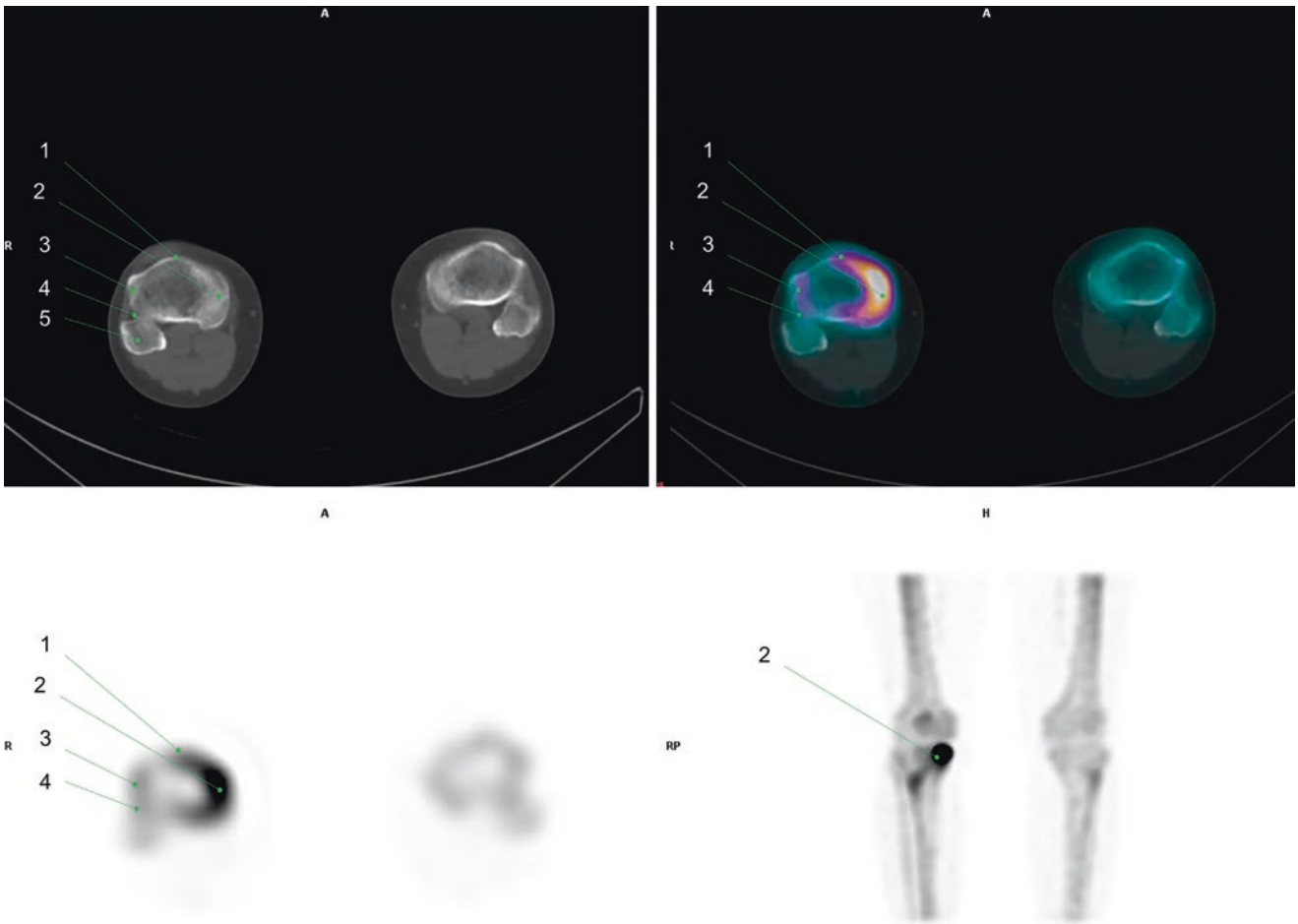

Fig. 50 1. Tibial tuberosity
2. Active lesion at right medial meniscus
3. Tibial lateral condyle
4. Fibular articular facet
5. Fibular head

2.1.2 Case 2

A 56-year-old female with a history of breast cancer complained of pain in her right lower posterior chest after a fall. ^{99m}Tc-MDP SPECT/CT showed focal increased activity in the right posterior 11th rib, corresponding to a callus formation at a fracture seen on CT. An acute fracture (up to 3–4 weeks after initial injury) will show increased radiotracer uptake surrounding the fracture site. Ninety-five percent of fractures are positive in patients under 65 years old, but skull fractures rarely show activity. In the healing phase with a variable time course, there is a gradual decrease in radiotracer activity, but 40% of fractures remain abnormal after 1 year (Fig. 51) [50].

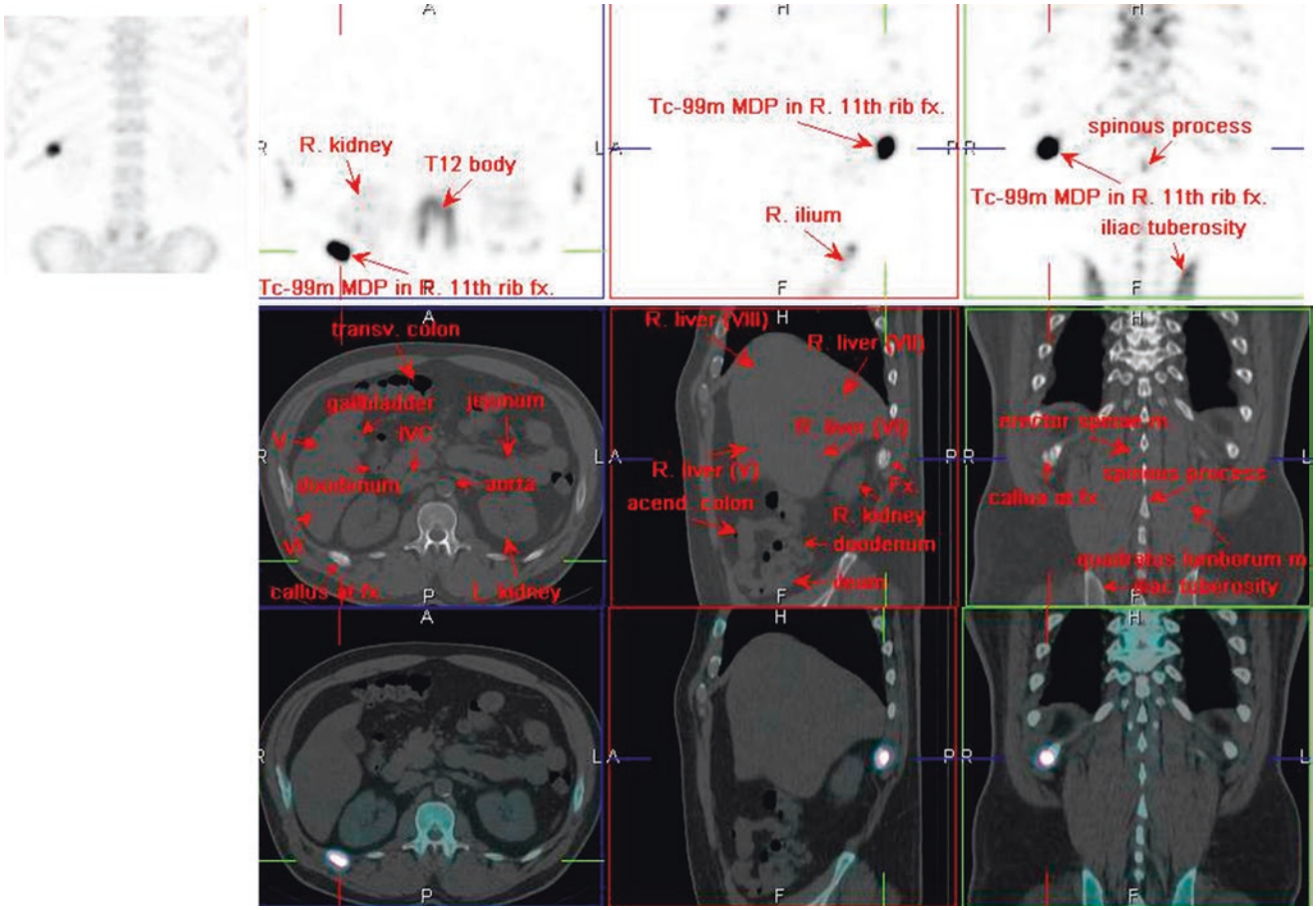

Fig. 51 ^{99m}Tc-MDP SPECT/CT

2.1.3 Case 3

A 65-year-old male patient with a history of lung cancer, who developed a backache following a car accident. ^{99m}Tc-MDP SPECT/CT showed a focal area of markedly increased activity in the spinous process of L4, corresponding to a fracture shown on CT. Slightly increased activity in the bilateral facet joints of L4 was also noted, caused by degenerative changes (Fig. 52) [51].

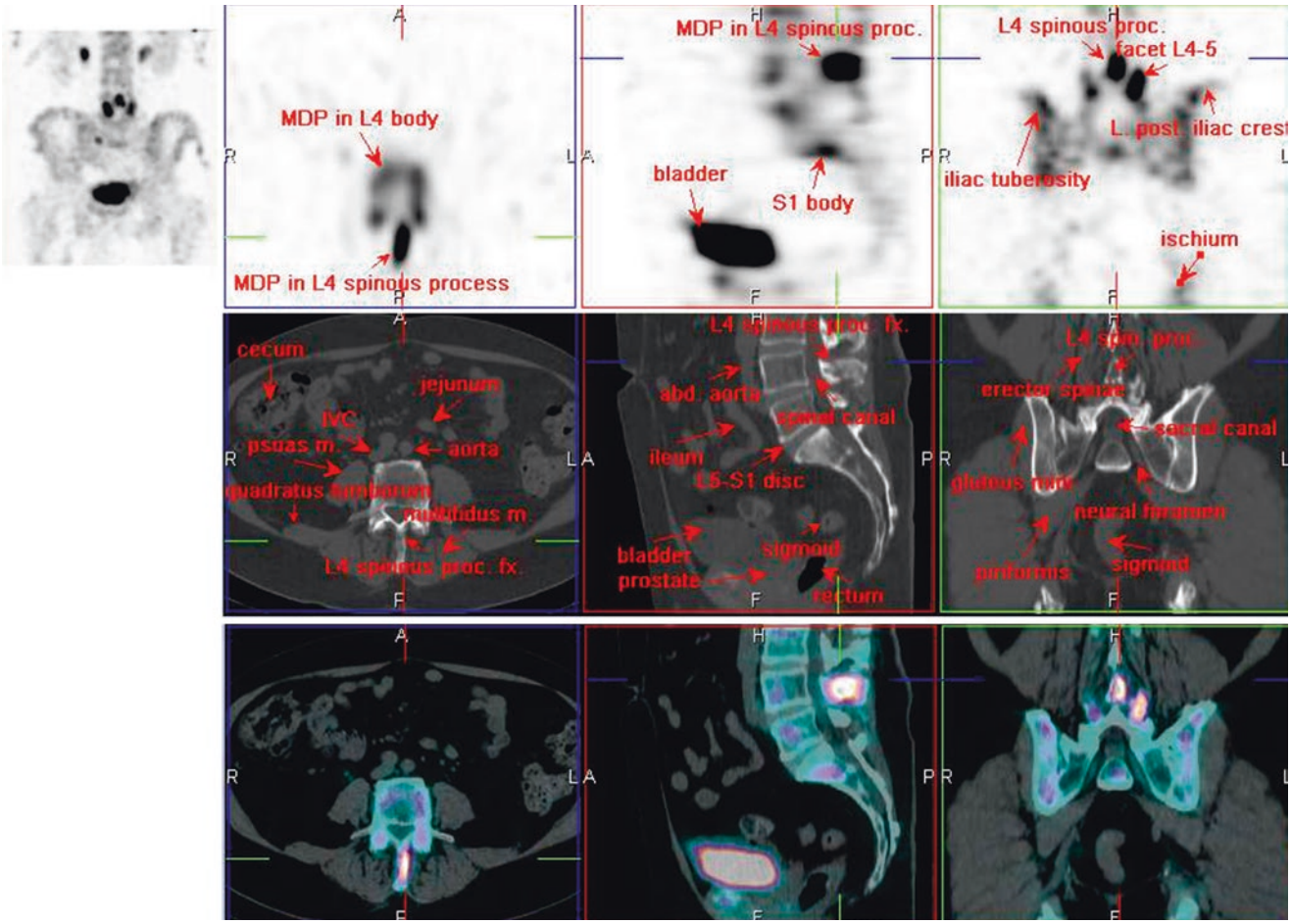

Fig. 52 ^{99m}Tc-MDP SPECT/CT

2.1.4 Case 4

A 61-year-old female patient with chronic bilateral shoulder pain and limitation was admitted for evaluation. ^{99m}Tc-MDP SPECT/CT was performed, finding diffuse increased uptake in the bilateral shoulder joint capsules and bony structures, which was consistent with adhesive capsulitis, more severe in the right shoulder (Figs. 53, 54, 55, and 56) [53].

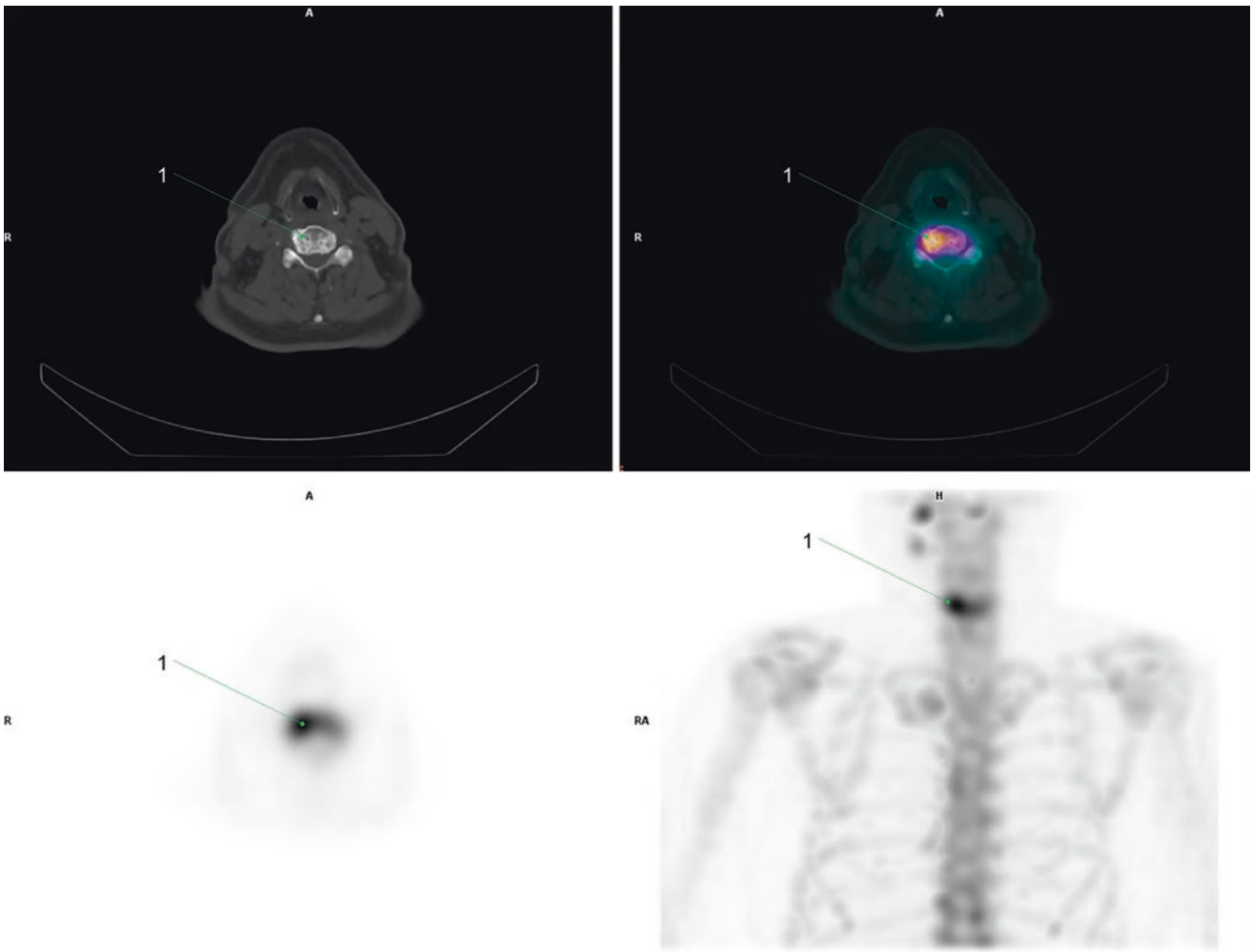

Fig. 53 1. Degenerative change in C5 spine

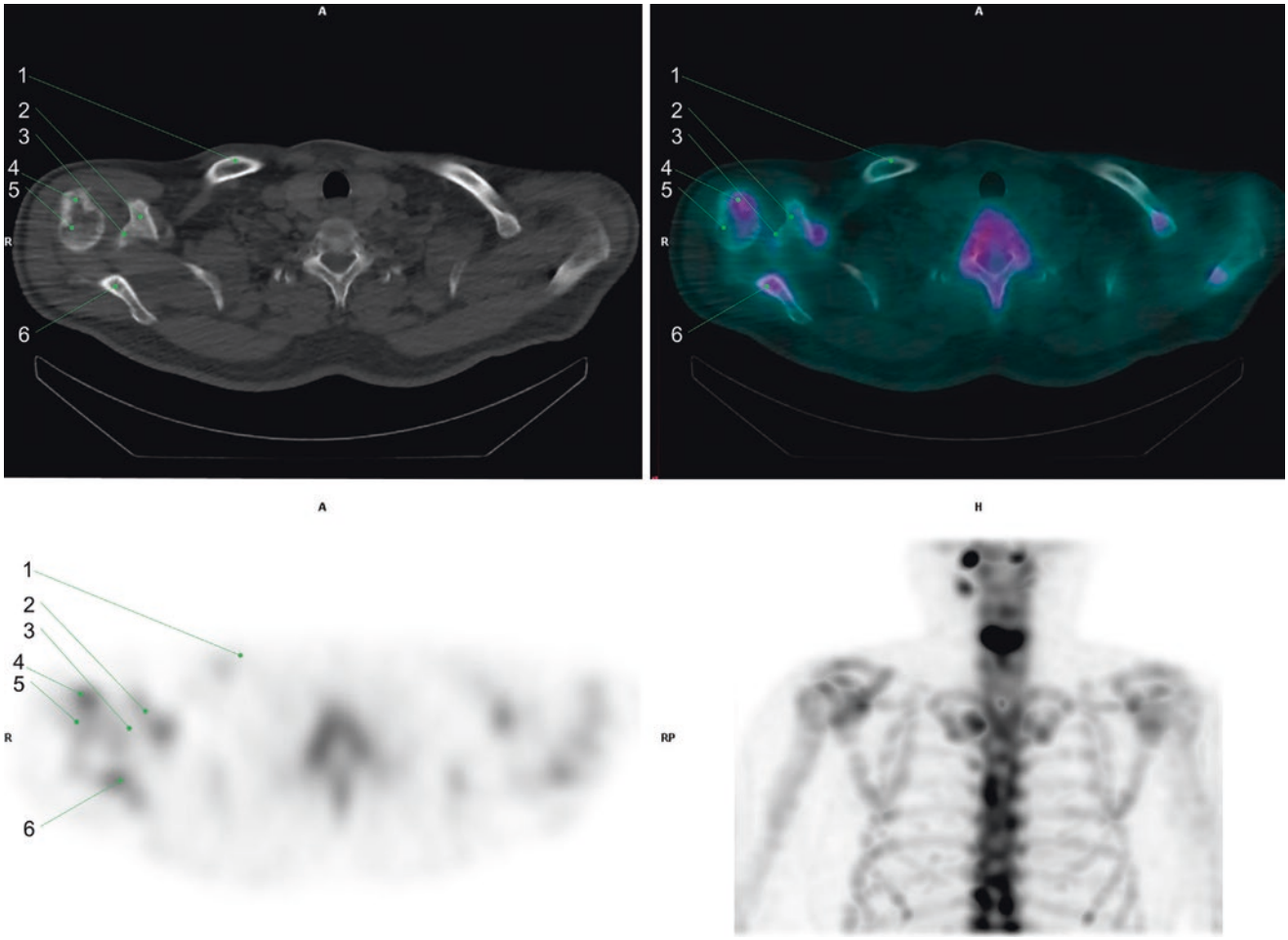

Fig. 54 1. Clavicle
2. Coracoid process
3. Supraglenoid tubercle
4. Greater tubercle of humerus
5. Humeral head
6. Scapula

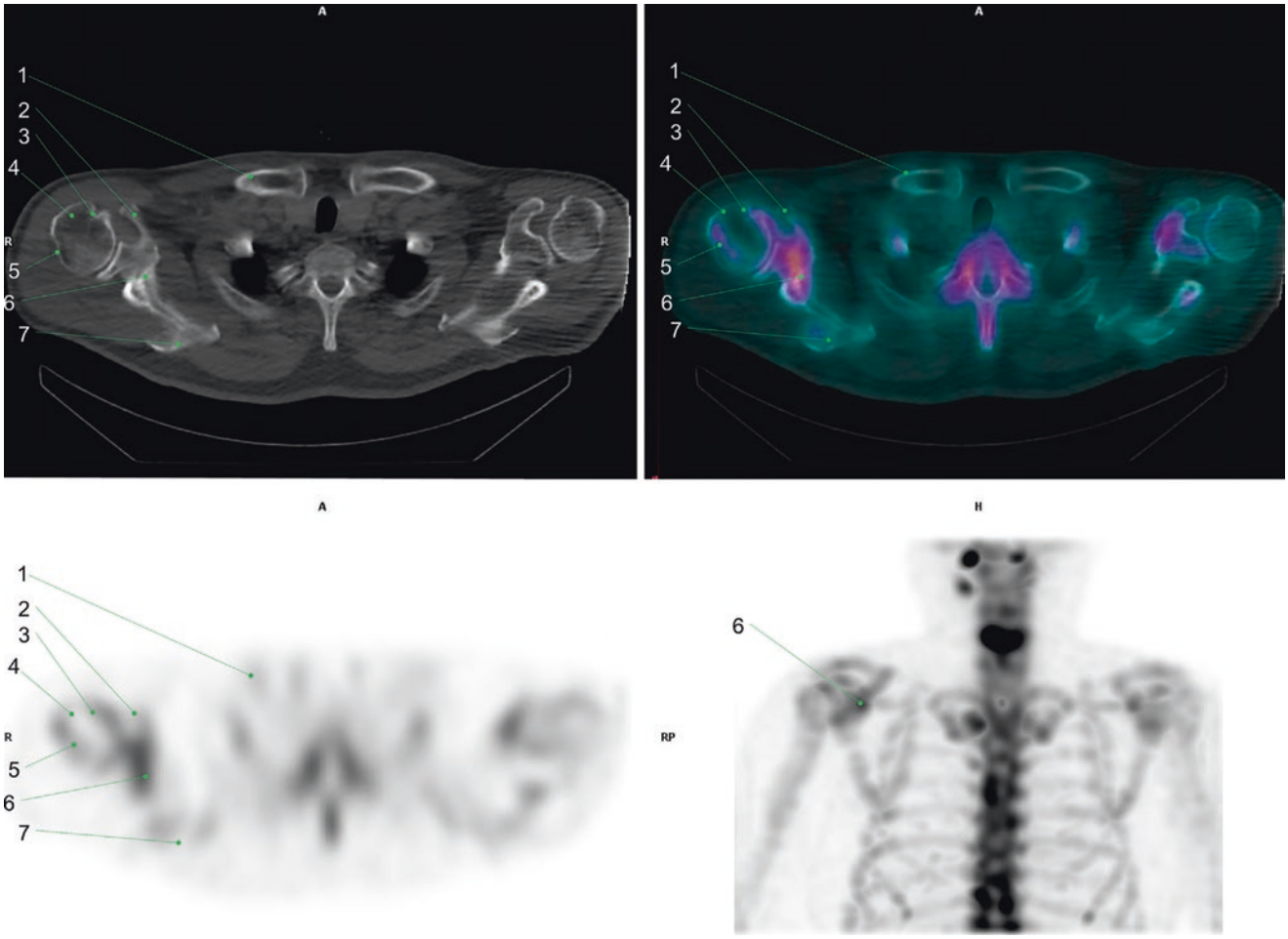

Fig. 55 1. Clavicle
2. Coracoid process
3. Lesser tubercle of humerus
4. Greater tubercle of humerus
5. Diffuse uptake in joint capsule of humeral head
6. Scapula
7. Acromion

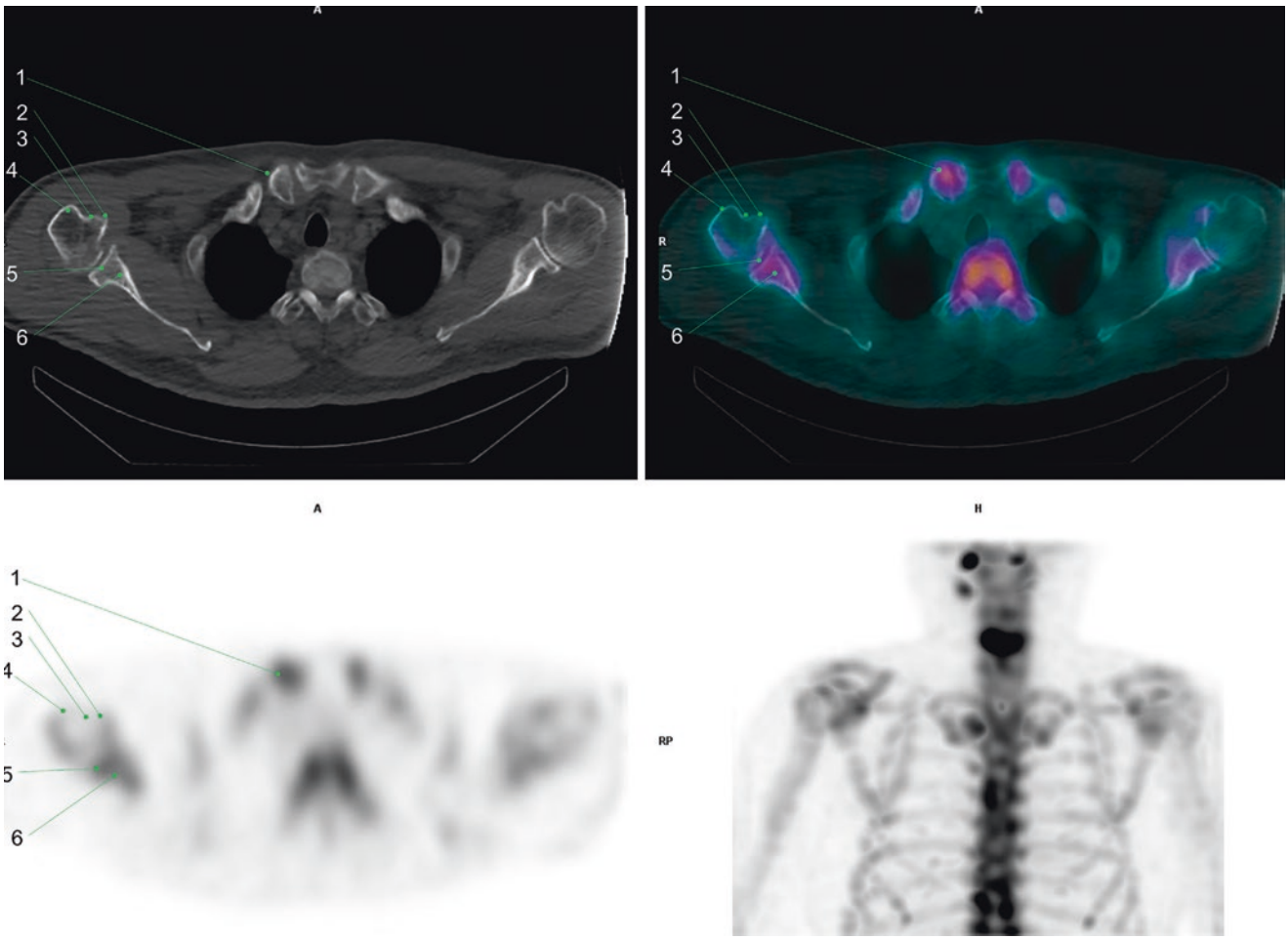

Fig. 56 1. Clavicle
2. Lesser tubercle
3. Intertubercular sulcus
4. Greater tubercle
5. Increased uptake in glenoid cavity
6. Scapula neck

2.1.5 Case 5

A 21-year-old male patient with bilateral temporomandibular joint pain. ^{99m}Tc-MDP SPECT/CT was performed, finding increased uptake in both temporomandibular joints (right > left), due to degenerative osteoarthritis (Fig. 57).

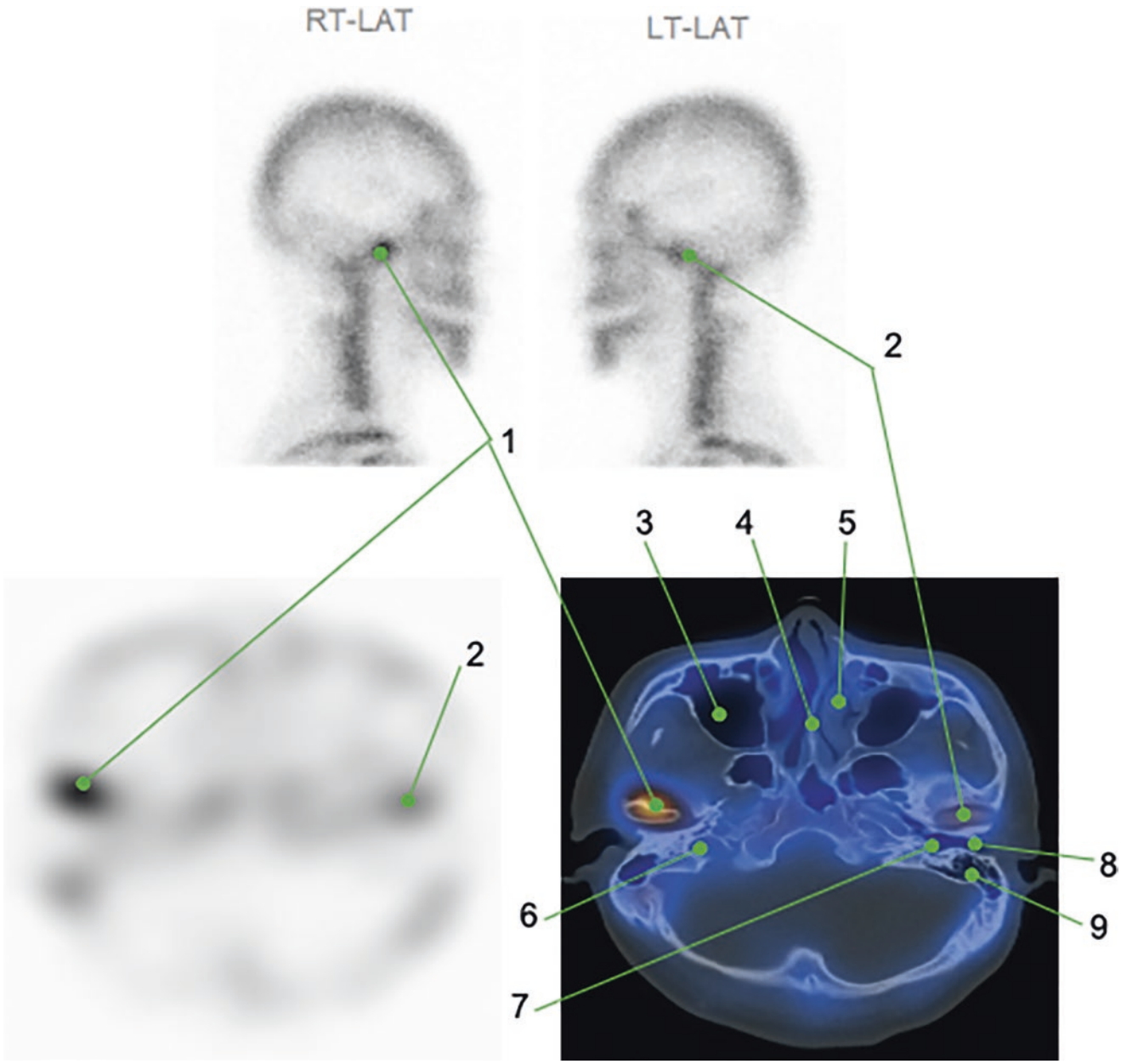

Fig. 57 1. Focal increased uptake in the right temporomandibular joint
2. Focal increased uptake in the left temporomandibular joint
3. Right maxillary sinus
4. Nasal septum
5. Left middle concha
6. Right jugular foramen
7. Left inner ear
8. Left external auditory canal
9. Left mastoid air cells

2.1.6 Case 6

A 48-year-old male patient with right knee varus deformity treated with high tibial osteotomy. In the immediate postoperative period, ^{99m}Tc-MDP SPECT/CT was performed *(top)*, finding, in addition to the normal changes of surgery, degenerative changes in the right knee with increased focal uptake in the femorotibial joint, more marked in the medial compartment, as well as in the patellofemoral joint. Three months after surgery, the patient attended with mild pain in the right knee. A new study was carried out *(bottom)* where degenerative changes showed improvement, but as a new finding, an increased uptake was observed in one of the surgical screws at the proximal tibia. Normal reactive postoperative changes were considered as the first option; however, a short-term follow-up was recommended to rule out other complications, which were later discarded (Fig. 58).

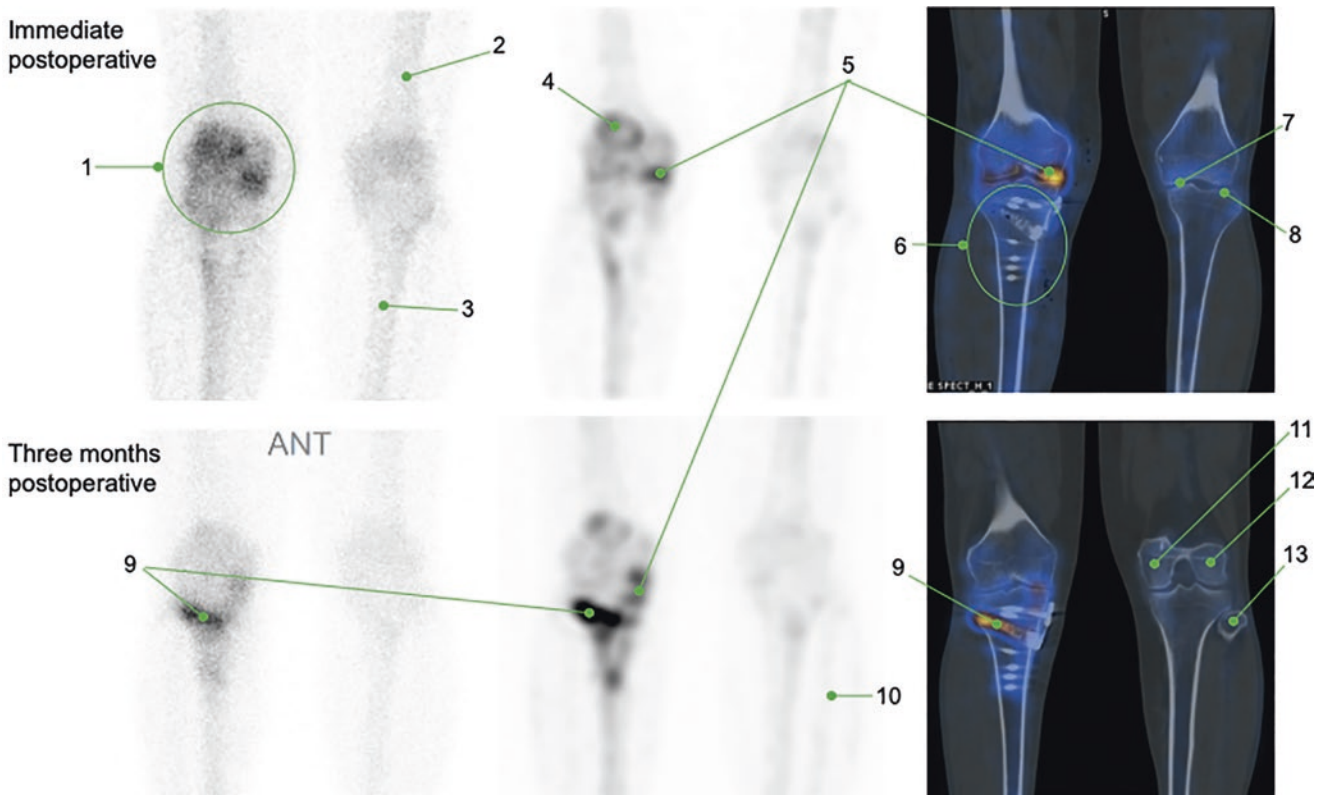

Fig. 58 1. Increased uptake in the right knee joint
2. Left femoral shaft
3. Left tibial shaft
4. Increased uptake in the right patellofemoral joint: degenerative changes
5. Increased uptake in the medial compartment of the right knee: degenerative changes
6. Surgical material (screws) in the right proximal tibia
7. Left femorotibial joint, medial compartment
8. Left femorotibial joint, lateral compartment
9. Increased uptake in the right proximal tibia at one of the surgical screws
10. Left fibula shaft
11. Left medial femoral condyle
12. Left lateral femoral condyle
13. Left fibula head

2.1.7 Case 7

A 16-year-old male patient with a history of leukemia, who developed left hip pain after completion of chemotherapy. ^{99m}Tc-MDP SPECT/CT showed a curvilinear moderately increased activity in the left femoral head at an ill-defined area of increased density on CT, caused by a healing microfracture with avascular necrosis (AVN). AVN is cellular death of bone components caused by interruption of the blood supply. It often leads to destruction of the joint articular surface. The classic sites are the head of the femur, the neck of the talus, and the waist of the scaphoid. AVN initially shows decreased radiotracer activity in the affected region, followed by a hyperemic phase with increased uptake (Fig. 59) [55].

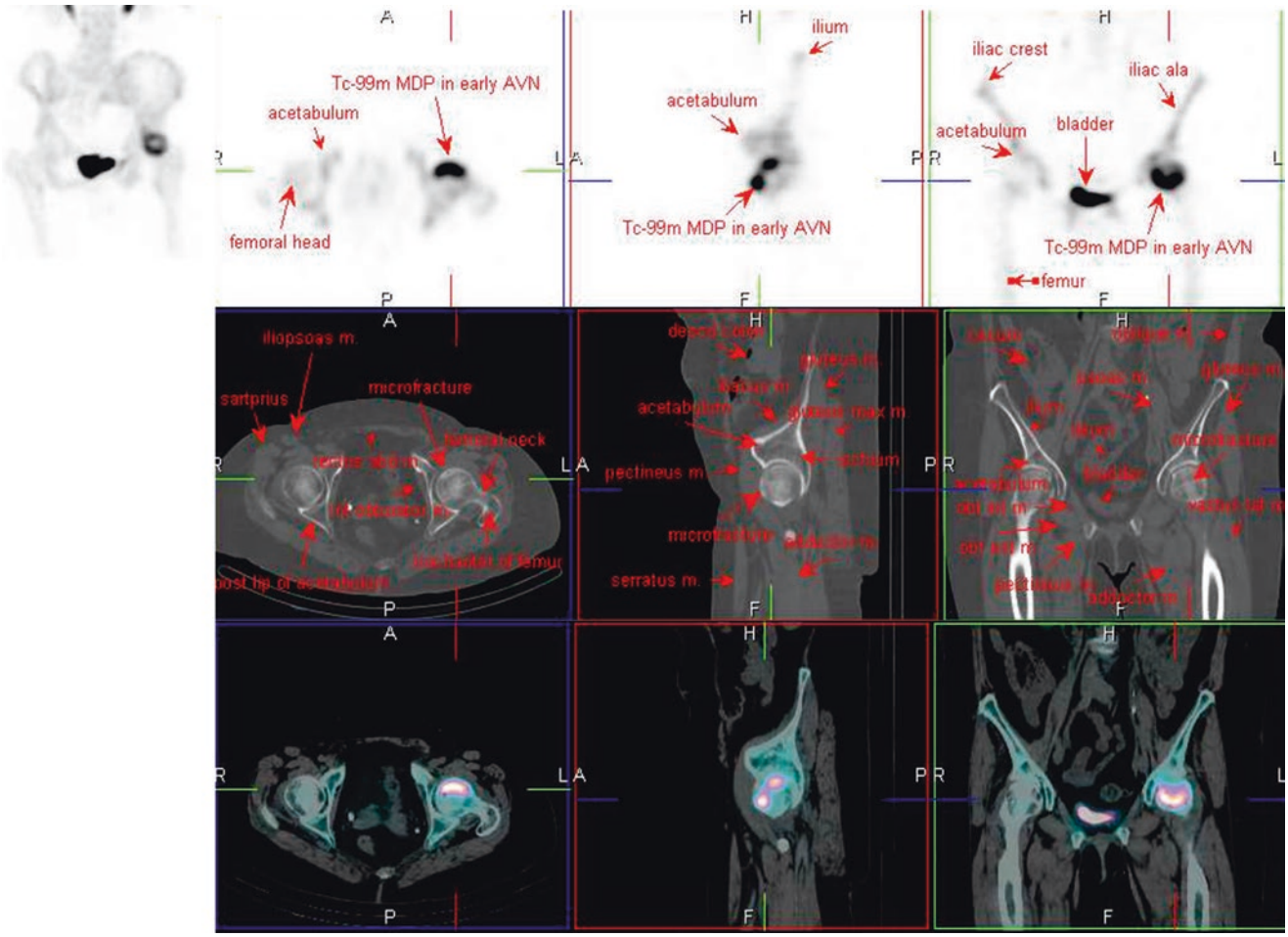

Fig. 59 ^{99m}Tc-MDP SPECT/CT

2.1.8 Case 8

A 20-year-old male patient with progressive low back pain, worsened by physical activity. ^{99m}Tc-MDP SPECT/CT was performed and showed increased uptake in the inferior aspect of bilateral sacroiliac joints, without morphologic changes. The findings were consistent with sacroiliitis (Fig. 60).

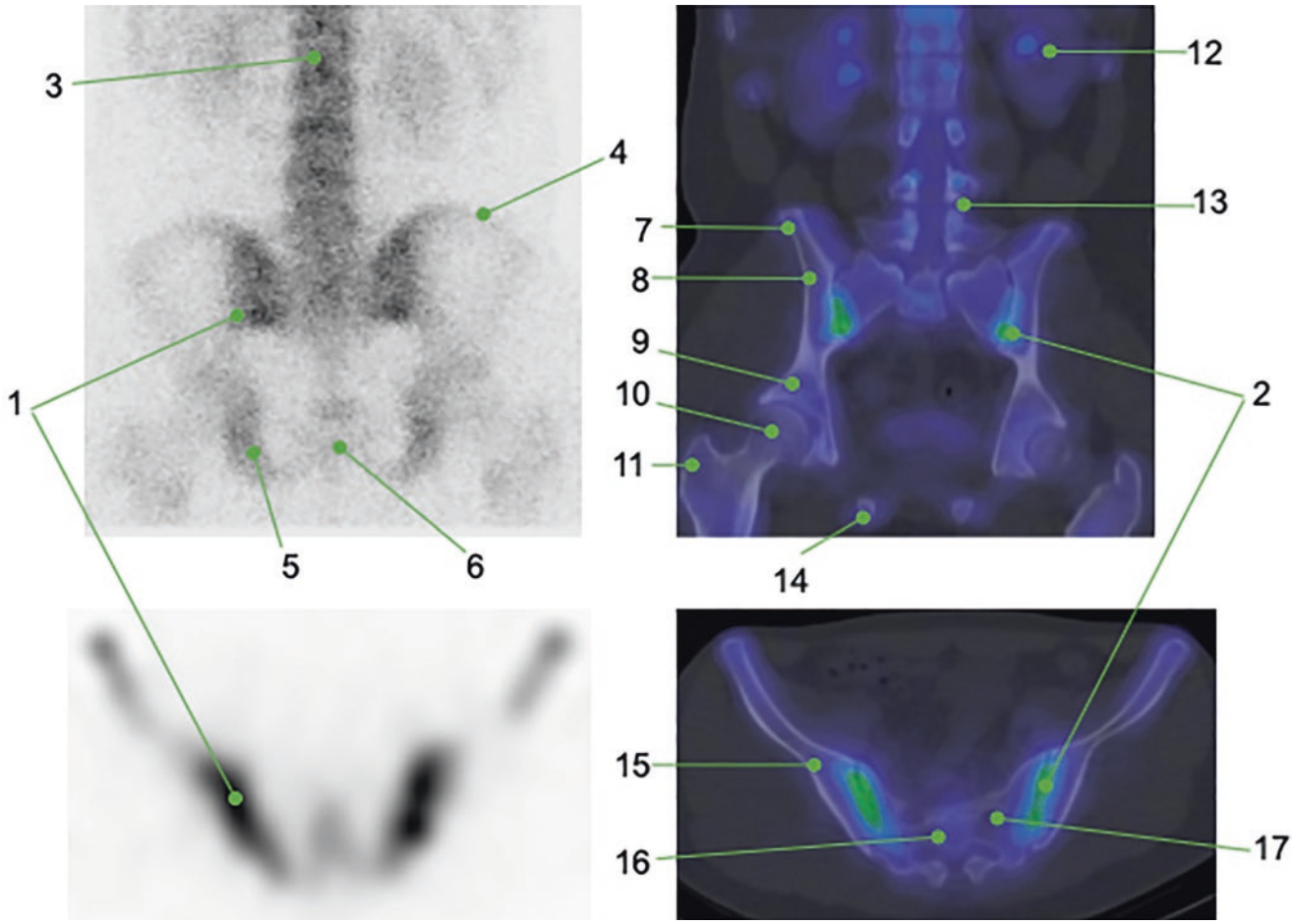

Fig. 60 1. Focal increased uptake in the right sacroiliac joint inferior aspect
2. Focal increased uptake in the left sacroiliac joint inferior aspect
3. Lumbar vertebral body, L2
4. Left iliac crest
5. Right ischium
6. Pubis
7. Right posterior superior iliac spine
8. Right ilium
9. Right acetabulum
10. Right femoral head
11. Right femur greater trochanter
12. Left kidney
13. Left L4-L5 facet joint
14. Right ischial tuberosity
15. Right iliac wing
16. Sacrum
17. Left sacral foramen

2.1.9 Case 9

A 27-year-old male patient with right foot pain. ^{99m}Tc-MDP SPECT/CT was performed finding focal increased uptake in the medial aspect of the midfoot, adjacent to the medial side of the navicular bone, at an accessory ossicle. These findings confirmed the diagnosis of accessory navicular syndrome (Fig. 61).

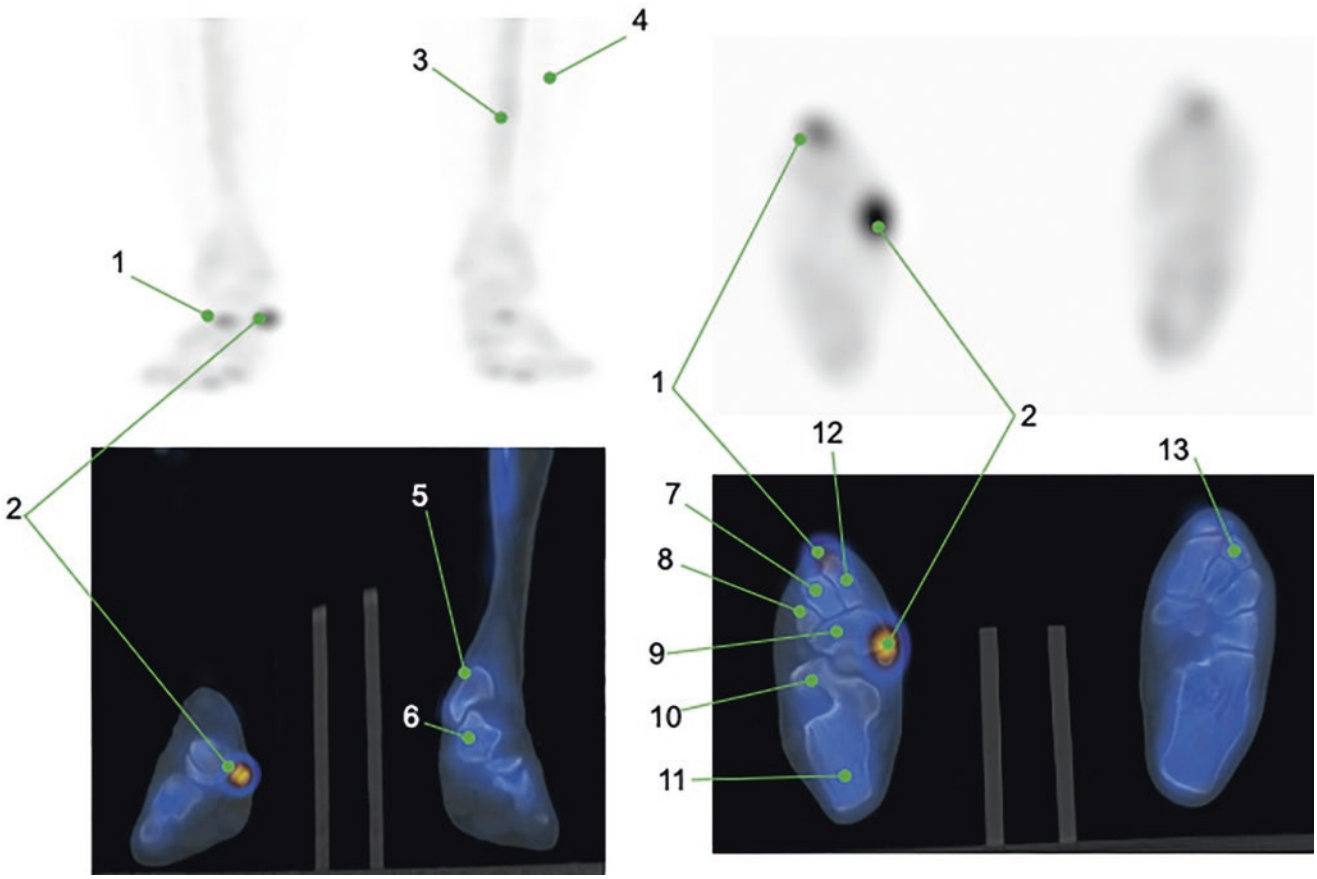

Fig. 61 1. Mild increased uptake in the right medial cuneiform-first metatarsal joint
2. Markedly increased uptake in the right midfoot at the accessory navicular bone
3. Left tibia shaft
4. Left fibula shaft
5. Left distal tibia, medial malleolus
6. Left talus bone
7. Right middle cuneiform (II)
8. Right lateral cuneiform (III)
9. Right navicular bone
10. Right sustentaculum tali
11. Right calcaneus bone
12. Right medial cuneiform (I)
13. Left proximal second metatarsal bone

2.2 Others

2.2.1 Gastrointestinal Bleeding

2.2.1.1. Case 1

A 10-year-old male patient with anaplastic large B-cell lymphoma was suffering from hematochezia caused by acute graft-versus-host disease (GVHD) after peripheral blood stem cell treatment. ^{99m}Tc-labeled red blood cell (^{99m}Tc-RBC) gastrointestinal bleeding SPECT/CT was done to find the bleeding source. A focal uptake was found in the third portion of the duodenum, corresponding to the acute bleeding site (Figs. 62, 63, 64, 65, 66, and 67) [56].

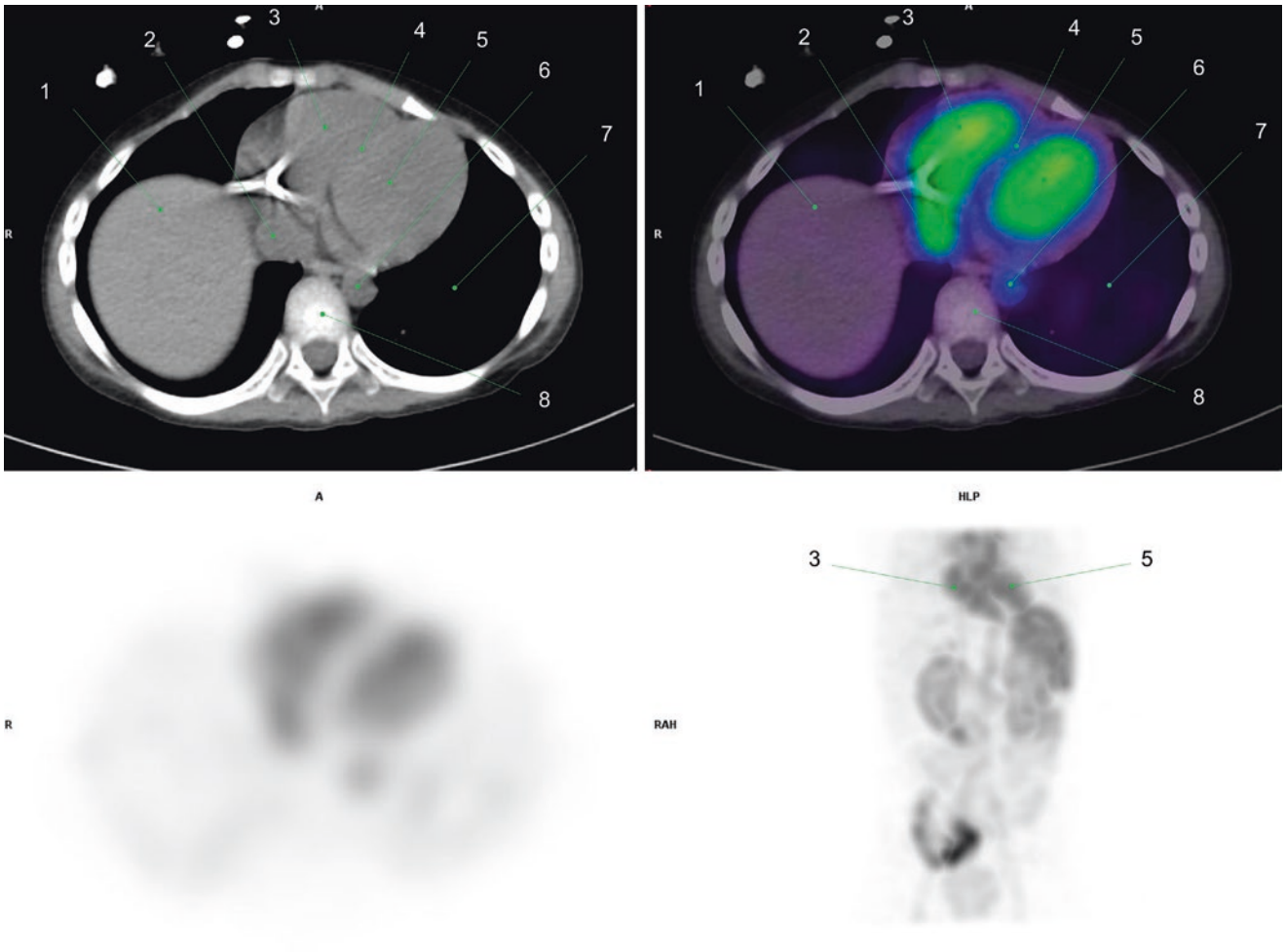

Fig. 62 1. Liver
2. Inferior vena cava
3. Right ventricle
4. Interventricular septum
5. Left ventricle
6. Aorta
7. Left lung
8. Vertebral body

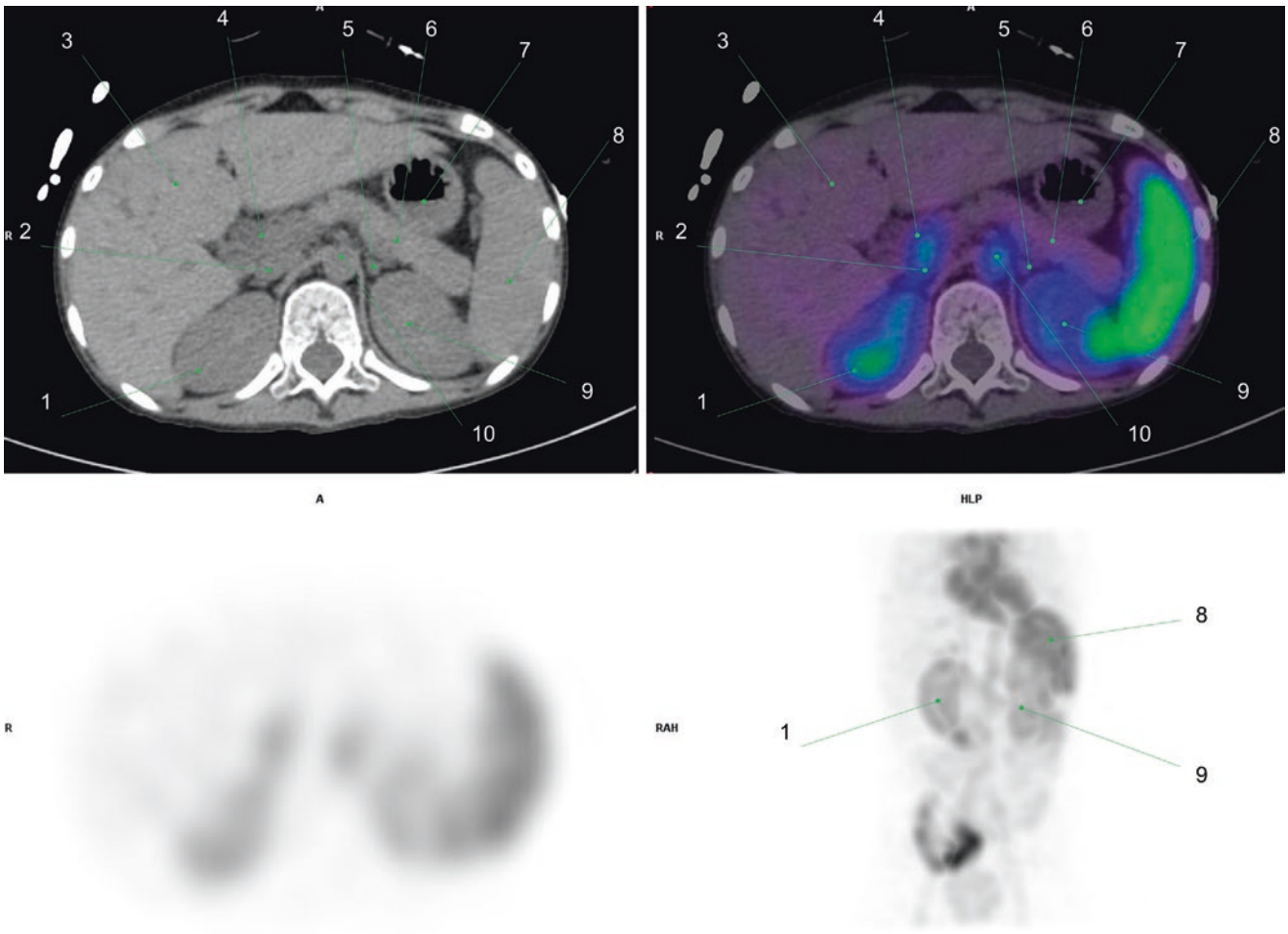

Fig. 63 1. Renal cortex
2. Inferior vena cava
3. Right lobe of liver
4. Head of pancreas
5. Left adrenal gland
6. Tail of pancreas
7. Body of stomach
8. Spleen
9. Renal pelvis
10. Abdominal aorta

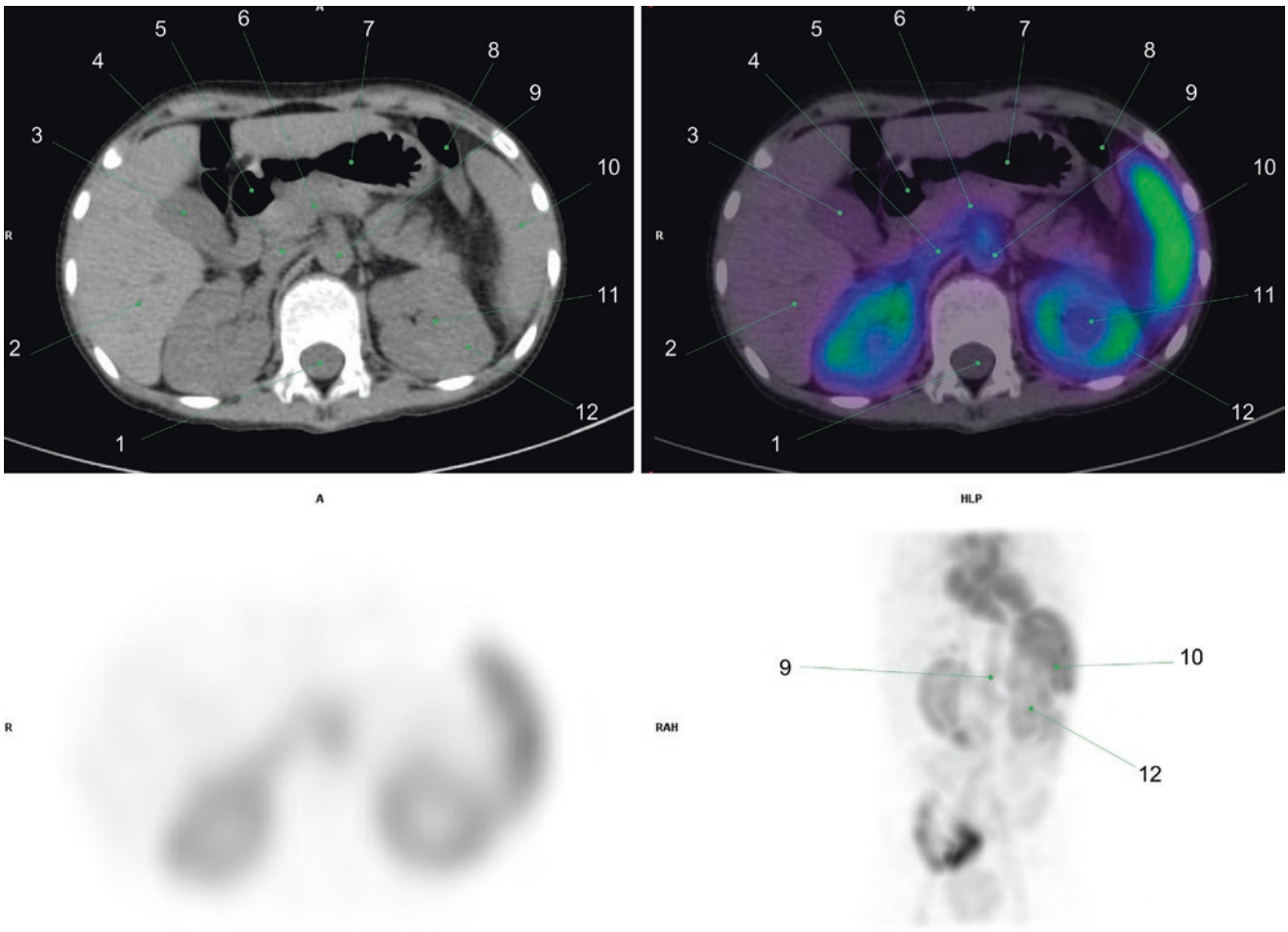

Fig. 64 1. Vertebral canal
2. Liver
3. Gallbladder
4. Inferior vena cava
5. Superior part (1st) of duodenum
6. Pancreatic head
7. Stomach lower body
8. Transverse colon
9. Abdominal aorta
10. Spleen
11. Renal pelvis
12. Renal cortex

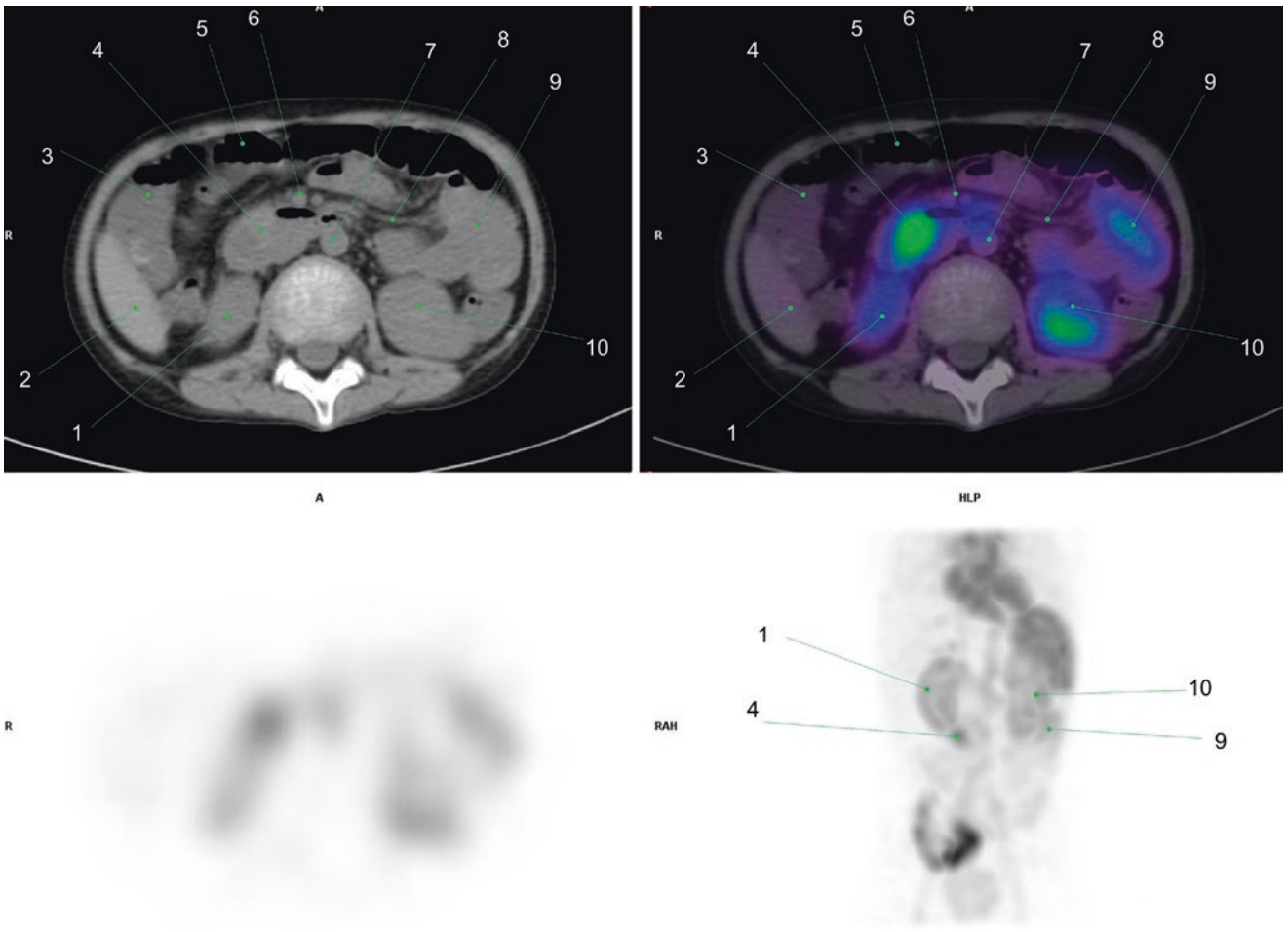

Fig. 65 1. Right kidney
2. Liver
3. Hepatic flexure of colon
4. Third portion of duodenum (Bleeding focus)
5. Transverse colon
6. Superior mesenteric vessels
7. Abdominal aorta
8. Mesenteric vessels
9. Ileum
10. Left kidney

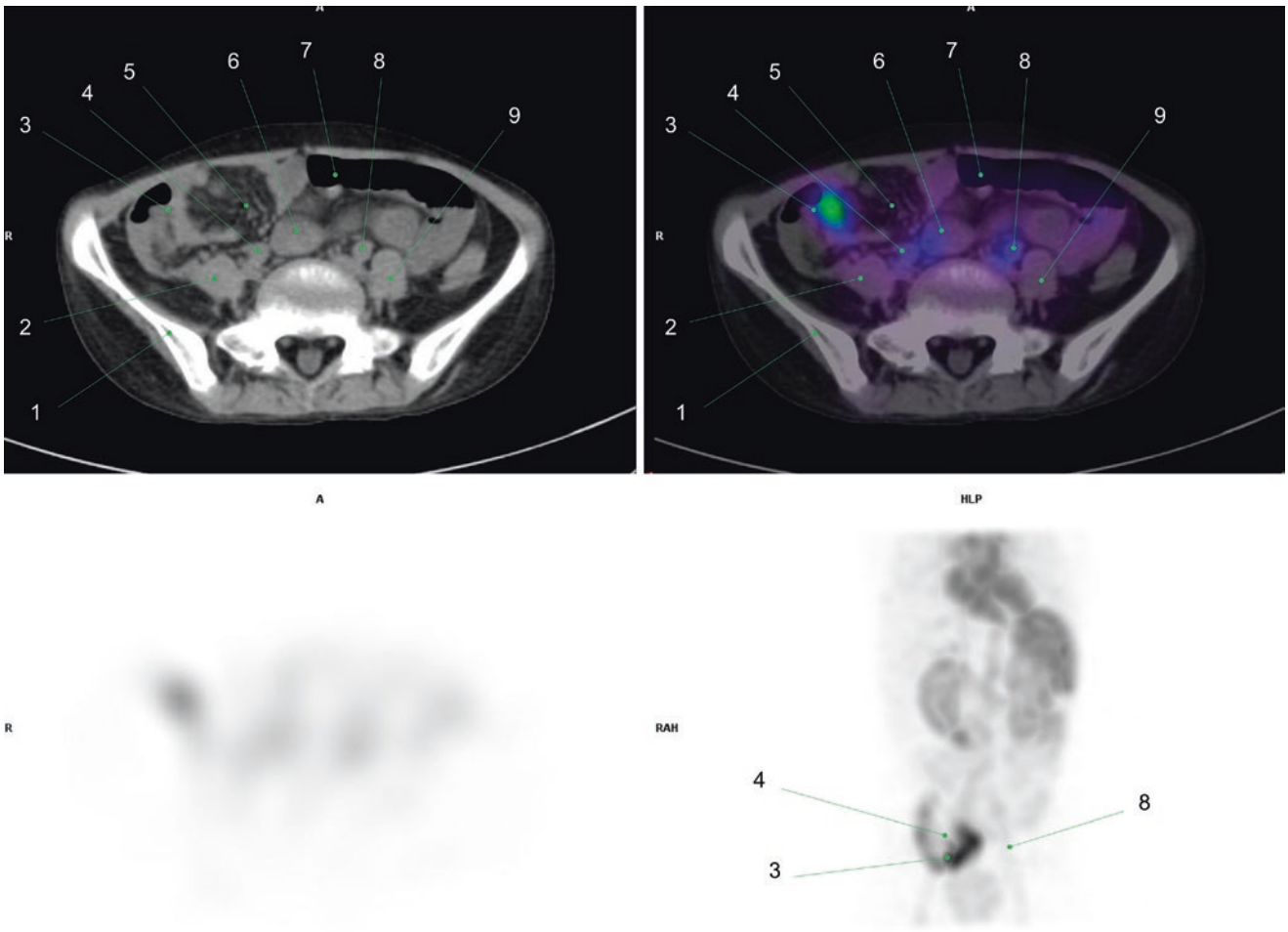

Fig. 66 1. Right ilium
2. Right psoas muscle
3. Ileocecal valve
4. Right common iliac vessels
5. Mesenteric vessels
6. Inferior vena cava
7. Transverse colon
8. Left common iliac vessels
9. Left psoas muscle

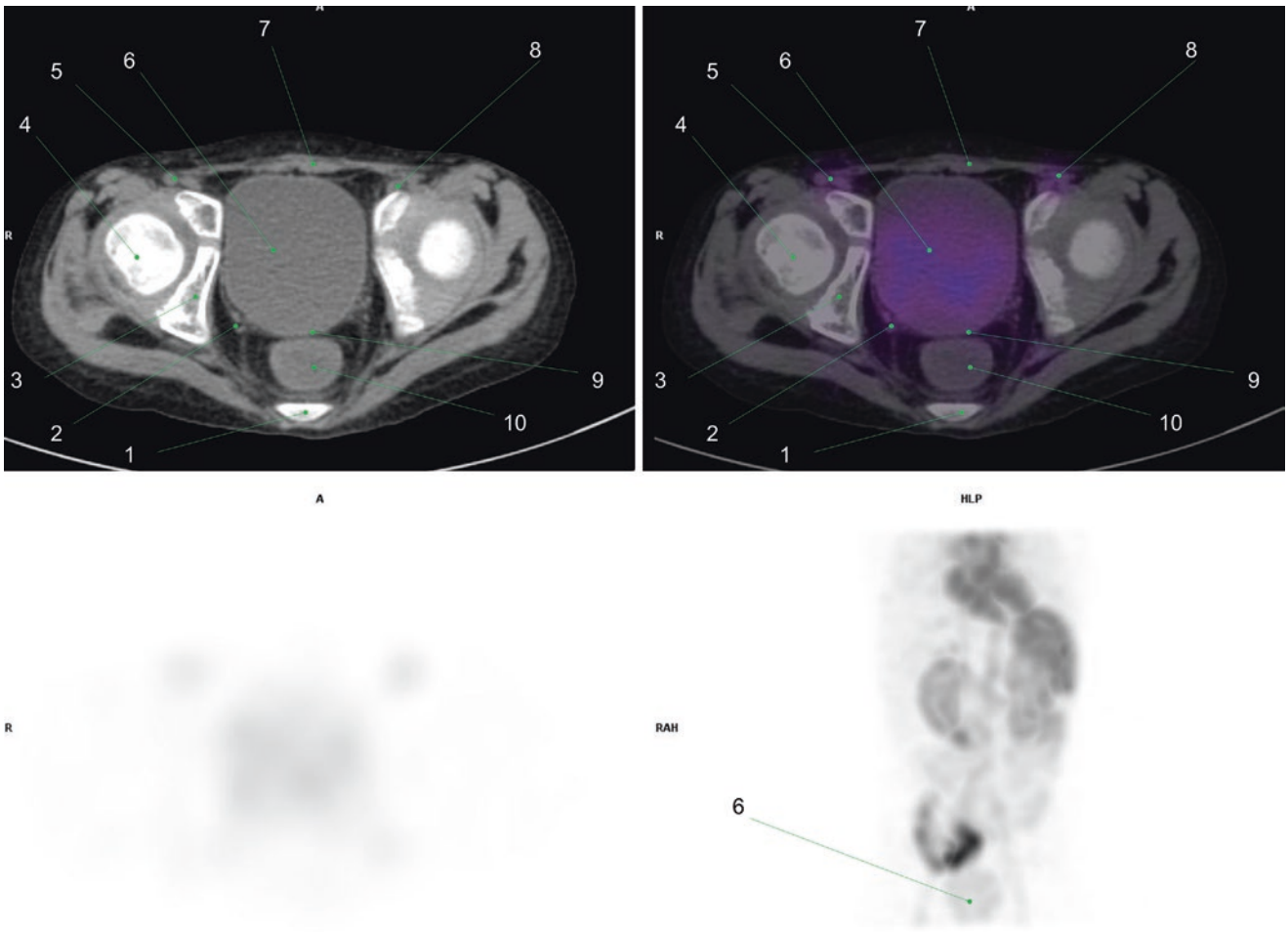

Fig. 67 1. Coccyx
2. Vesical vessels
3. Acetabulum
4. Right femoral head
5. Right external iliac vessels
6. Urinary bladder
7. Rectus abdominis
8. Left external iliac vessels
9. Rectovesical pouch
10. Rectum

2.2.1.2. Case 2

A 68-year-old male patient with a history of cystectomy for bladder cancer. He developed pain in the right lower abdomen and also noticed bloody stool. ^{99m}Tc-RBC SPECT/CT demonstrated a curvilinear moderately increased activity in the ileal conduit as well as the pouch and bag indicating active bleeding. ^{99m}Tc-RBC is useful for detecting active gastrointestinal bleeding and is prepared in vitro by mixing 1–3 mL of anticoagulated blood with stannous chloride and an oxidizing agent. The labeling procedure takes at least 20 minutes. Bleeding rates as low as 0.2 mL/min can be detected with a tagged red blood cell study compared to 1 mL/min for angiography. ^{99m}Tc-sulfur colloid requires a significant preparation time and is useful only for acute active bleeding with 2–3 minutes of vascular half-time. A positive study shows an activity that changes shape and position over time due to the peristalsis of intraluminal blood (Fig. 68) [57].

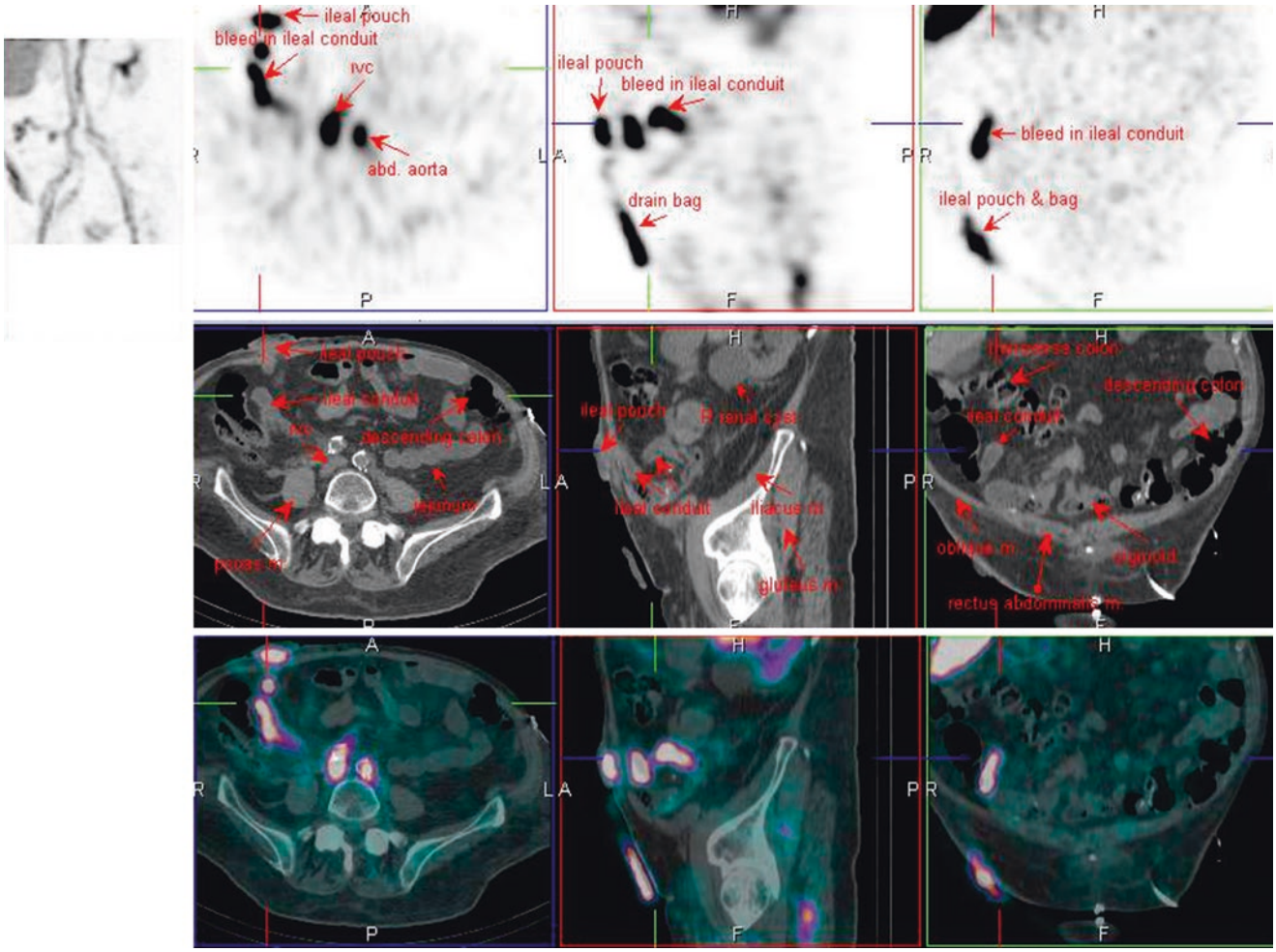

Fig. 68 ^{99m}Tc-RBC SPECT/CT

2.2.2 Abscess

2.2.2.1. Case 1

A 78-year-old female patient with a history of multiple myeloma, who attended for backache and fever. ^{111}In-WBC SPECT/CT showed a focal area of markedly increased activity in the left semispinalis muscle at the posterior lower neck adjacent to the spinous process of C6, corresponding to an ill-defined inflammatory collection. ^{111}In leukocyte, scan is helpful for detecting acute infection or inflammation. Its advantages compared to ^{99m}Tc-D, L-hexamethyl propyleneamine oxime (HMPAO) scan include the absence of interfering bowel and renal activity and the ability to perform delayed 24-hour imaging as well as simultaneous ^{99m}Tc-sulfur colloid or MDP scan. ^{67}Ga citrate scan is useful for detecting chronic infection or inflammation with lymphocytes or macrophages (Fig. 69) [58].

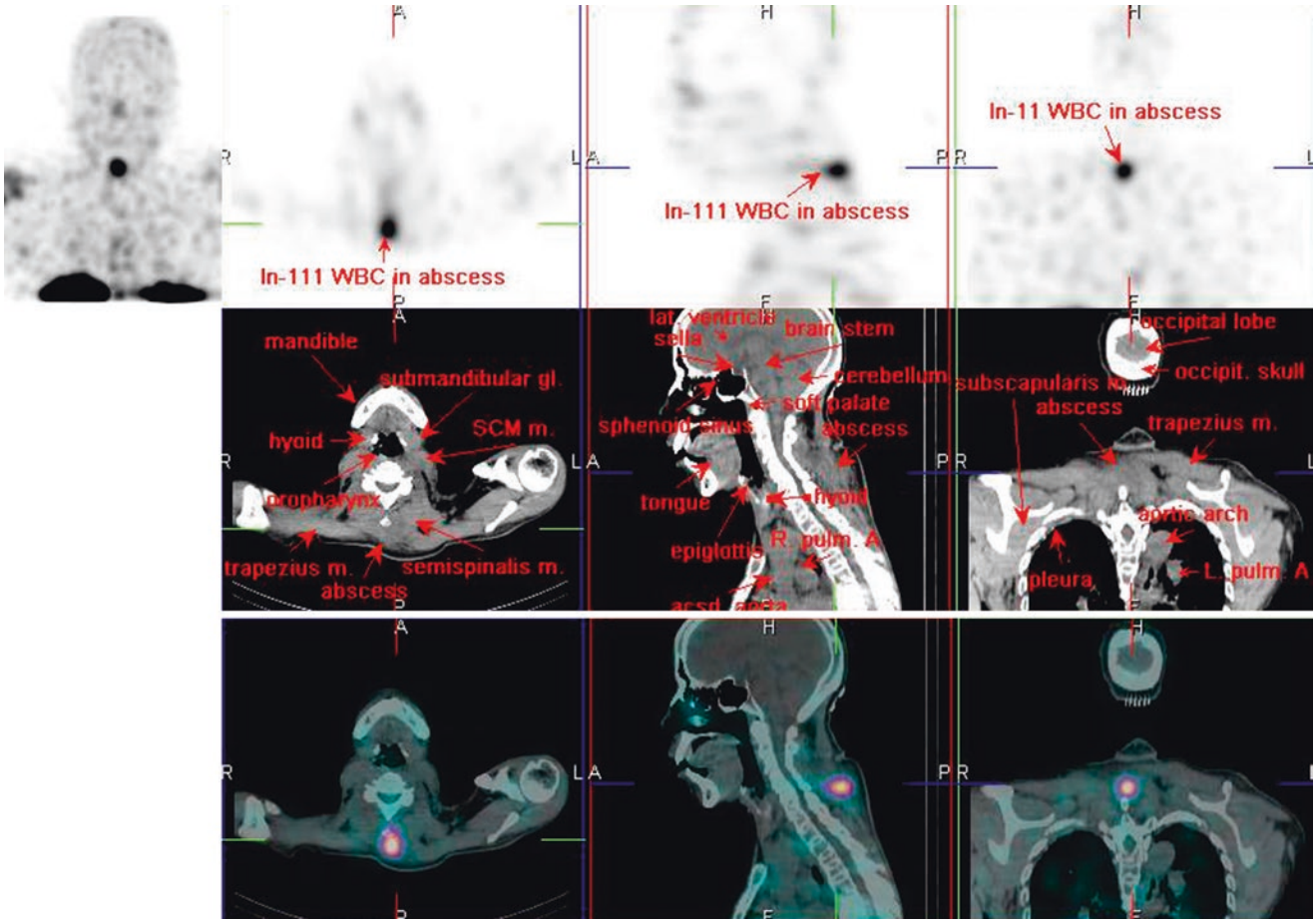

Fig. 69 ^{111}In-WBC SPECT/CT

2.2.3 Benign Thyroid Pathology

2.2.3.1. Case 1

A 57-year-old female patient with a new diagnosis of hypothyroidism.^{131}I SPECT/CT showed a focal area of moderately increased activity in the midline of the tongue base, corresponding to ectopic thyroid tissue in the thyroglossal duct. Ectopic thyroid refers to the presence of thyroid tissue in locations other than the normal anterior neck between the second and fourth tracheal cartilages. Lingual thyroid is the most common type (Fig. 70) [59].

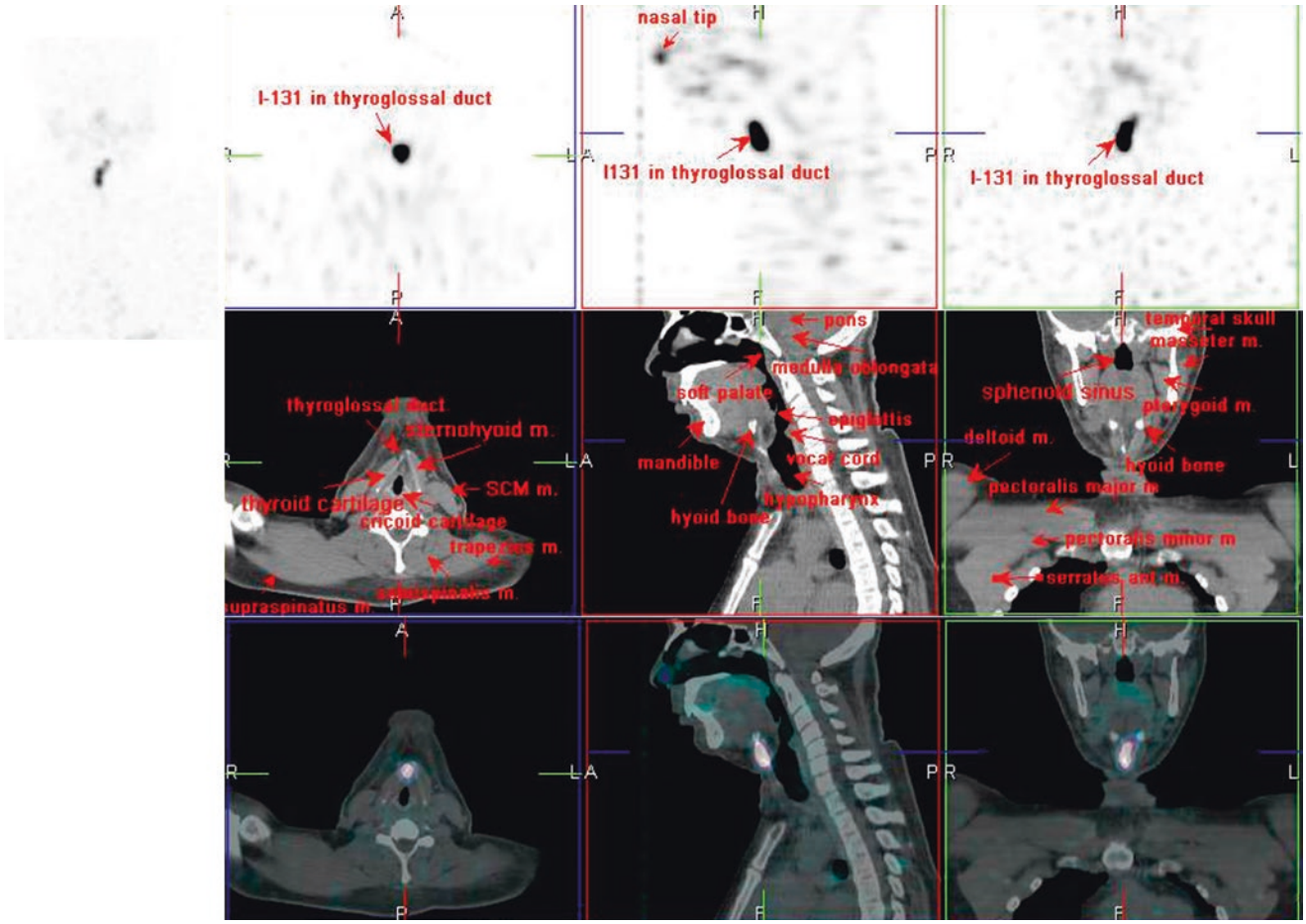

Fig. 70 ^{131}I SPECT/CT

2.2.3.2. Case 2

A 32-year-old female patient with neck pain and fever. Thyroid function studies showed low TSH with increased T3 and T4, so subacute thyroiditis was suspected. ^{99m}Tc-pertechnetate thyroid scan SPECT/CT was performed showing faintly visualized thyroid activity and decreased percentage of thyroid uptake (0.08%), so the diagnosis was confirmed (Fig. 71).

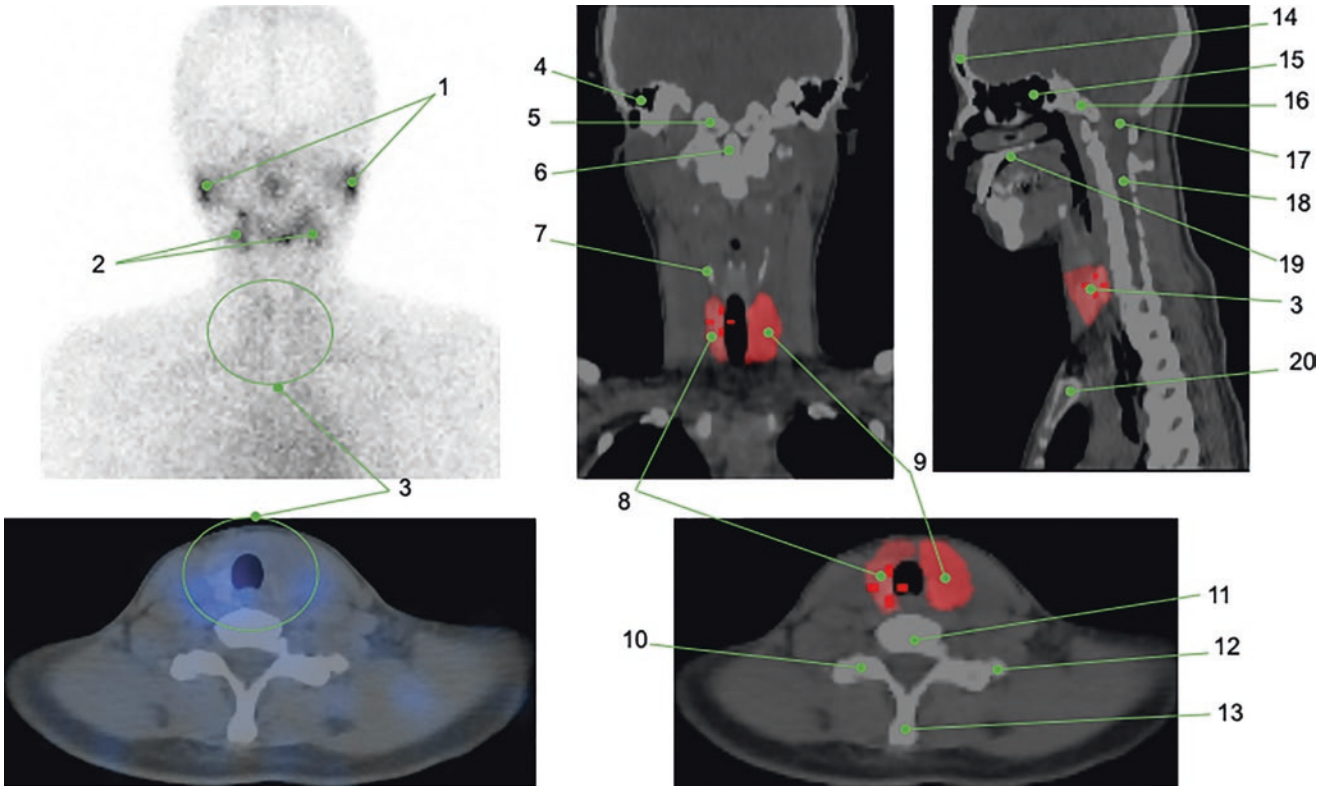

Fig. 71 1. Parotid glands
2. Submandibular glands
3. Faintly visualized thyroid gland
4. Right mastoid air cells
5. Right occipital condyle
6. Odontoid process
7. Thyroid cartilage, right superior aspect
8. Right thyroid lobe, normal size
9. Left thyroid lobe, enlarged
10. C5 right transverse process
11. C5 vertebral body
12. C5-C6 facet joint
13. C5 spinous process
14. Frontal sinus
15. Sphenoid sinus
16. Clivus
17. Foramen magnum
18. Cervical spinal canal
19. Hard palate
20. Sternum

2.2.3.3. Case 3

A 37-year-old female patient with known hyperthyroidism, Graves' disease, who attended her annual checkup. Thyroid function studies showed low TSH with increased T3 and T4, and increased TSH-R-Ab. ^{99m}Tc-pertechnetate thyroid scan SPECT/CT was performed showing diffuse enlargement of the thyroid gland with markedly increased percentage of thyroid uptake (26.32%) (Fig. 72).

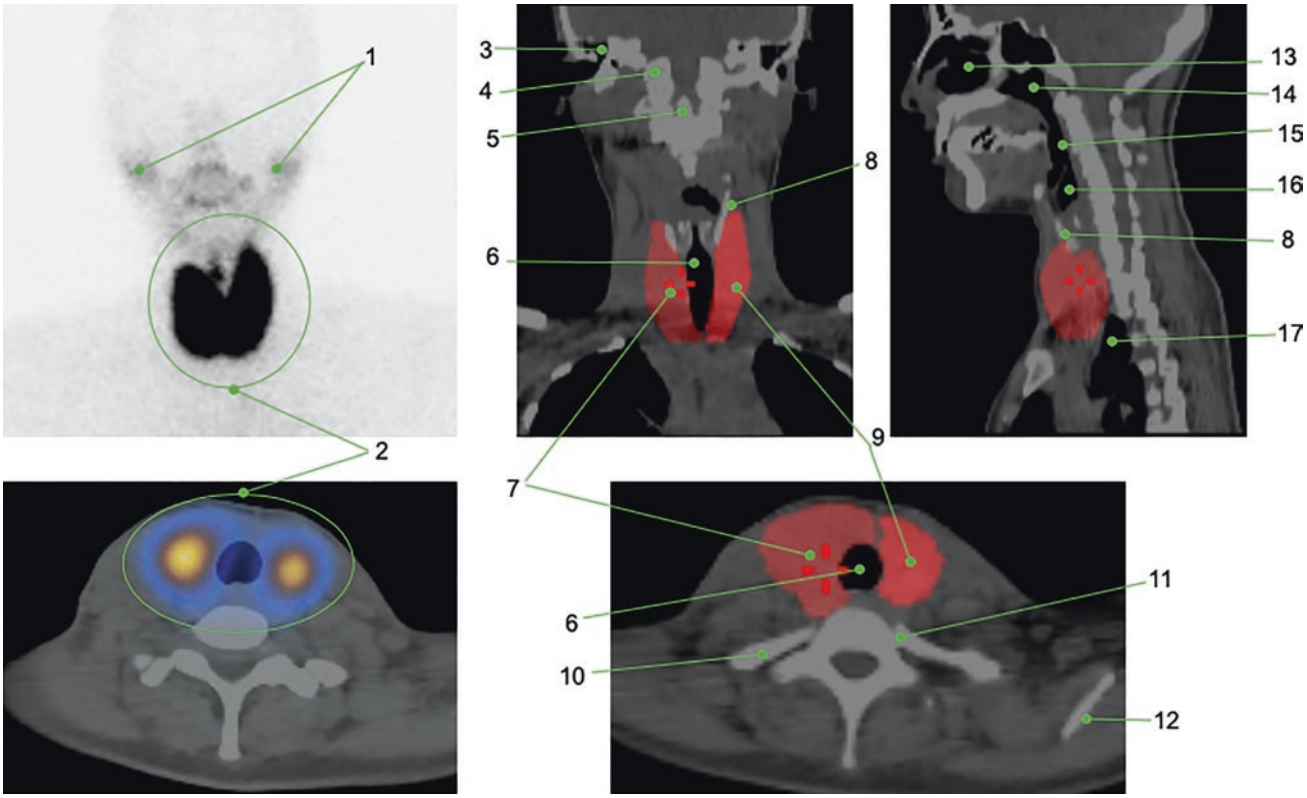

Fig. 72 1. Parotid glands
2. Diffusely enlarged thyroid gland with markedly increased uptake
3. Right mastoid air cells
4. Right occipital condyle
5. Odontoid process
6. Trachea
7. Right thyroid lobe, enlarged
8. Thyroid cartilage
9. Left thyroid lobe, enlarged
10. Right first rib
11. Left first costovertebral joint
12. Left scapula
13. Ethmoid air cells
14. Nasopharynx
15. Oropharynx
16. Larynx
17. Lung apex

2.2.4 Salivary Glands

2.2.4.1. Case 1

A 63-year-old female patient with nonspecific sicca. ^{99m}Tc-pertechnetate salivary gland scan SPECT/CT with quantitative analysis was performed and showed mild decreased uptake in bilateral parotid glands, with normal submandibular glands uptake, and normal bilateral function (Figs. 73 and 74).

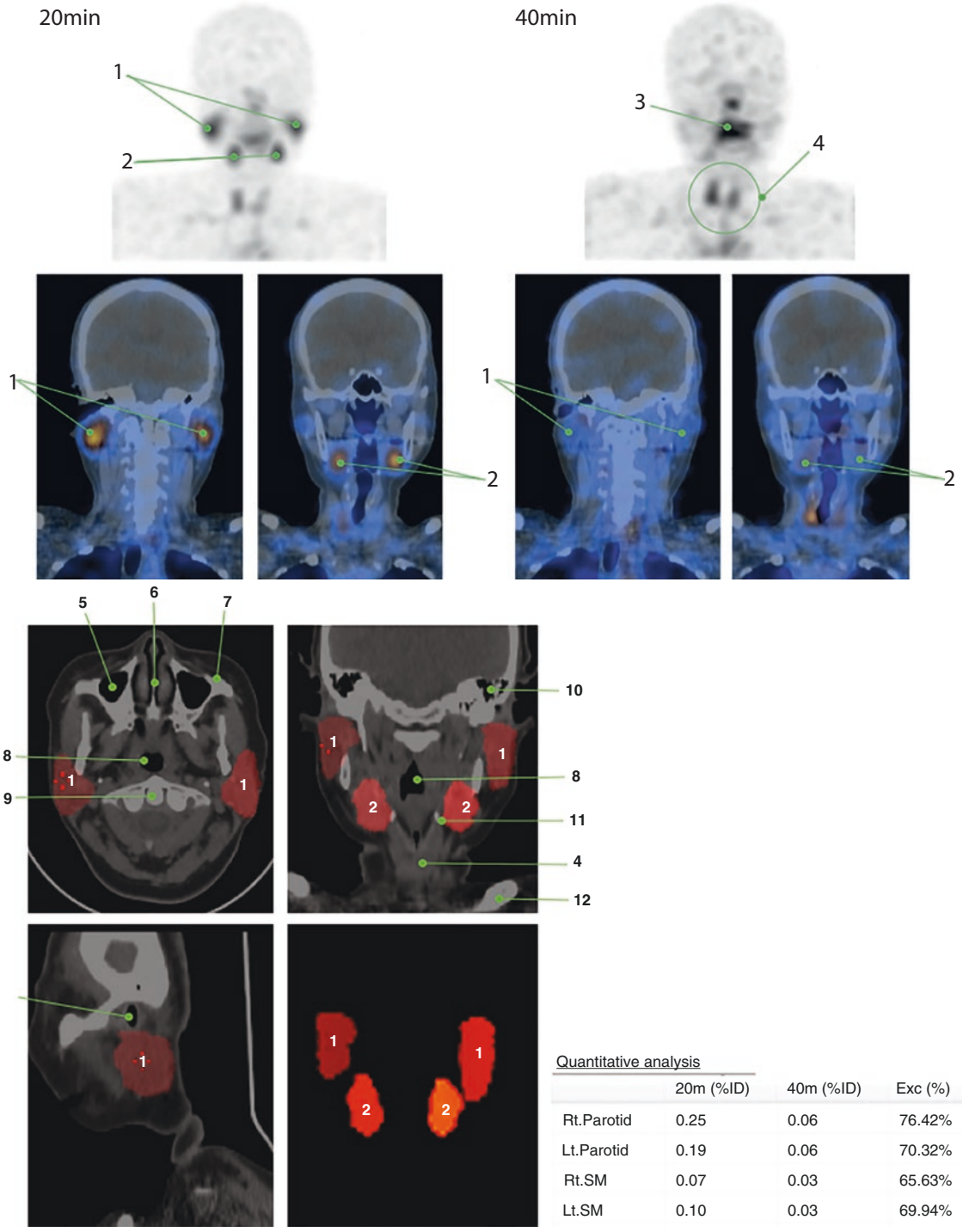

Quantitative analysis

	20m (%ID)	40m (%ID)	Exc (%)
Rt.Parotid	0.25	0.06	76.42%
Lt.Parotid	0.19	0.06	70.32%
Rt.SM	0.07	0.03	65.63%
Lt.SM	0.10	0.03	69.94%

Figs. 73 and 74 1. Parotid glands. The 20-minute scan shows bilateral mild decreased uptake, and the 40-minute scan shows complete excretion
2. Submandibular glands. The 20-minute scan shows normal bilateral uptake, and the 40-minute scan shows complete excretion
3. Radiotracer excretion in the oral cavity
4. Thyroid gland, normal uptake
5. Right maxillary sinus
6. Nasal septum
7. Left zygomatic arch
8. Trachea
9. Odontoid process
10. Left mastoid air cells
11. Left thyroid cartilage
12. Left clavicle

2.2.5 Cerebrospinal Fluid (CSF)

2.2.5.1. Case 1

A 66-year-old male patient with a history of head trauma. Moderate enlargement of ventricular size was found on CT, so after ventricular derivation, selected SPECT (*top*) and SPECT/CT (*bottom*) images of the head at 24 hours after injection of ^{111}In-DTPA into the L3-L4 spinal canal were obtained for evaluation. Images showed distribution in basal and Sylvian cisterns, without significant residual hydrocephalus or activity in the lateral ventricle, indicating non-communicating hydrocephalus (Fig. 75) [60].

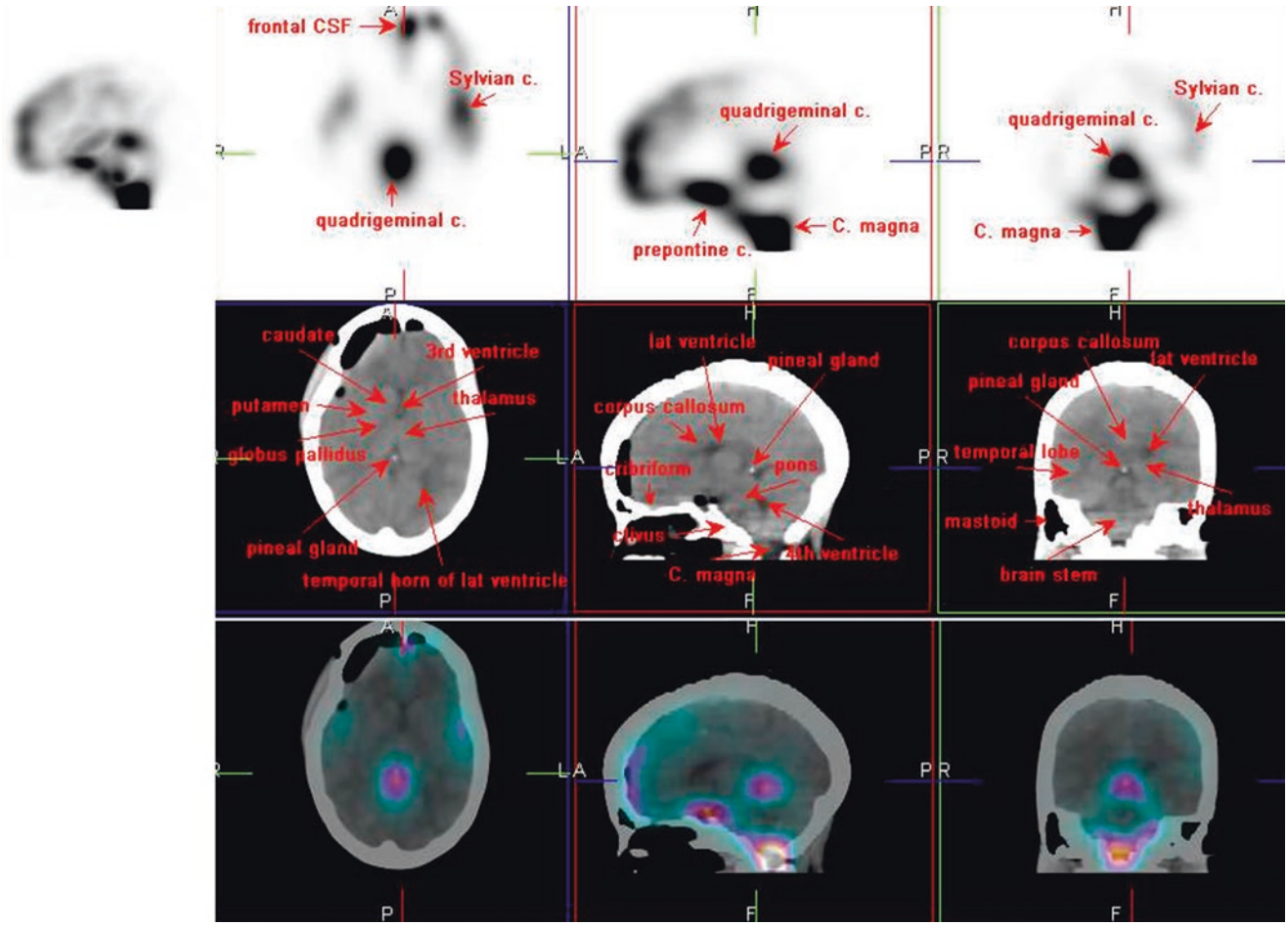

Fig. 75 ^{111}In-DTPA SPECT/CT

2.2.5.2. Case 2

A 72-year-old male patient with progressive gait disturbance, urinary incontinence, and dementia symptoms. Selected SPECT (*top*) and SPECT/CT (*bottom*) images of the head at 24 hours after injection of ^{111}In-DTPA into the L3-L4 spinal canal showed moderately increased activity in the lateral ventricles but no significant activity had migrated over to the convexity beyond the Sylvian cistern, indicating normal pressure hydrocephalus (Fig. 76).

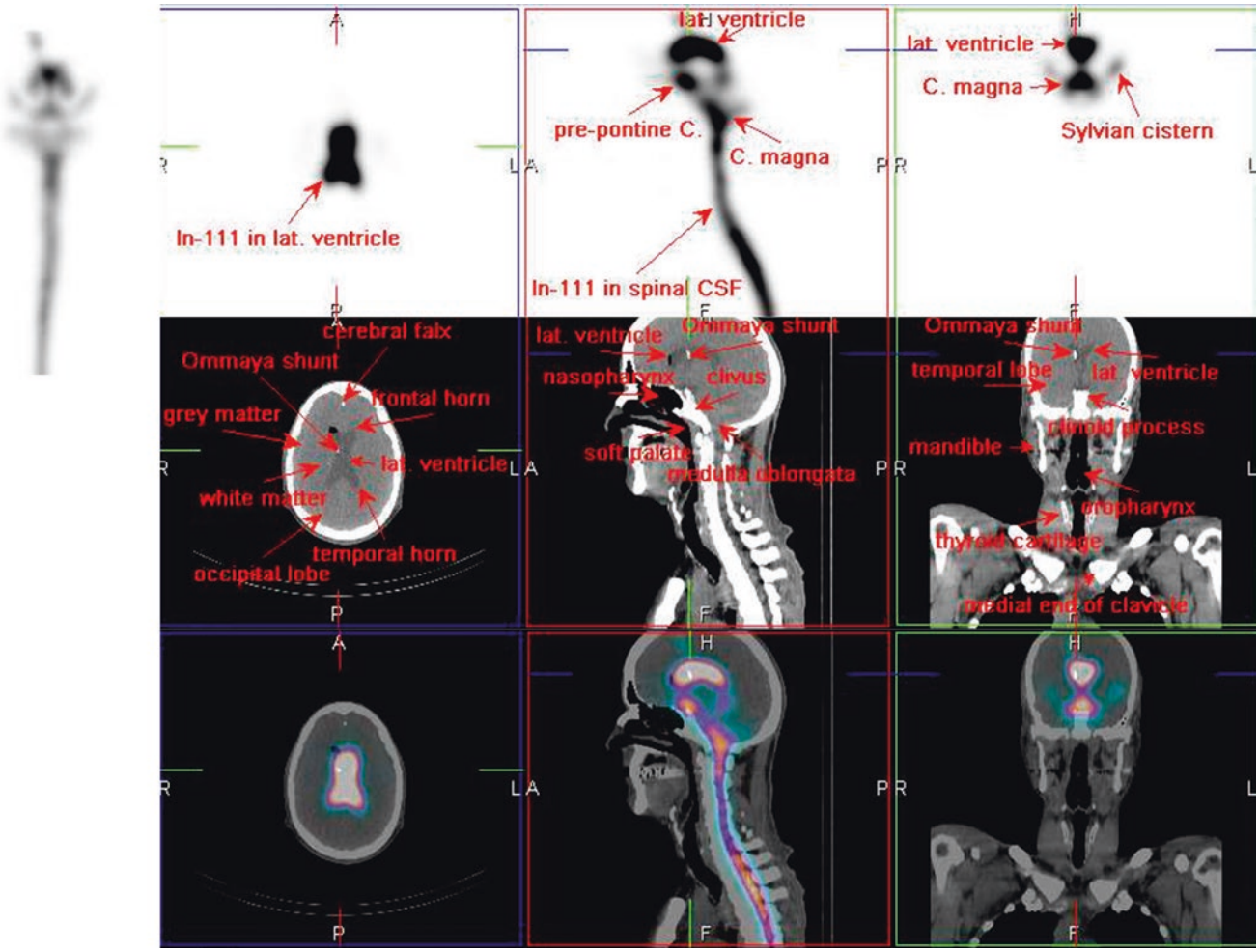

Fig. 76 ^{111}In-DTPA SPECT/CT

2.2.6 Central Venous Line Obstruction

2.2.6.1. Case 1

A 46-year-old male with a left central venous line complained of pain in the substernal area. A nuclear dynamic venous flow study using ^{99m}Tc-DTPA showed a focal area of increased activity in the distal left innominate vein, representing obstruction. Venous obstruction occurs when blood clots or vascular tissues develop and narrow the channel for flow. More than 40% of patients with a central venous line can develop a venous obstruction, and they may experience a swollen arm, neck pain, facial swelling, or shortness of breath (Fig. 77) [61].

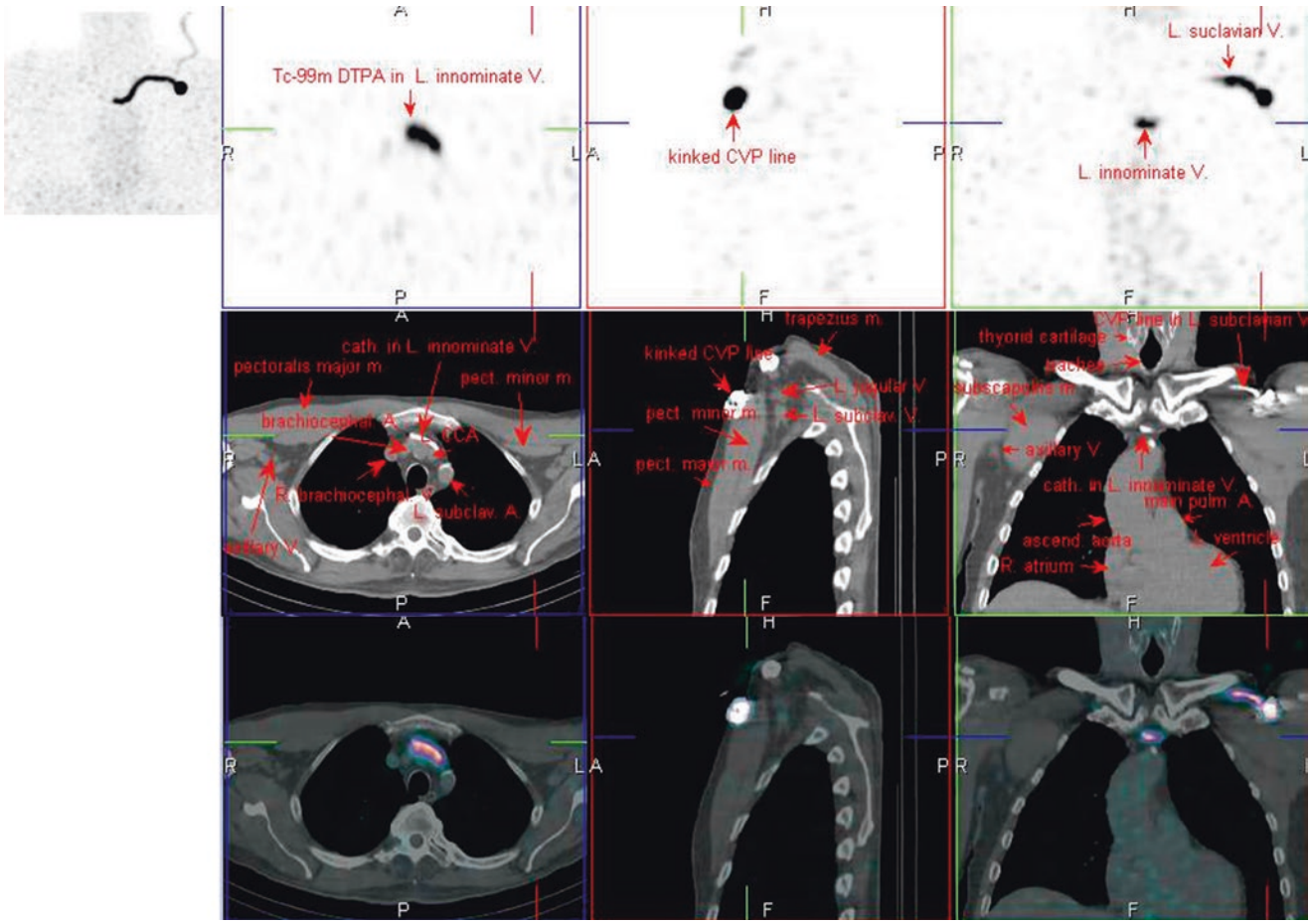

Fig. 77 ^{99m}Tc-DTPA SPECT/CT

2.2.7 Renal

2.2.7.1. Case 1

A 49-year-old male patient with right hydronephrosis due to renal pelvis stones. ^{99m}Tc-DTPA and SPECT/CT were performed for evaluation, finding decreased uptake in the right kidney with no significant effect in renal function. Calculated GFR (ml/min): left 48.58, right 42.36 (Fig. 78).

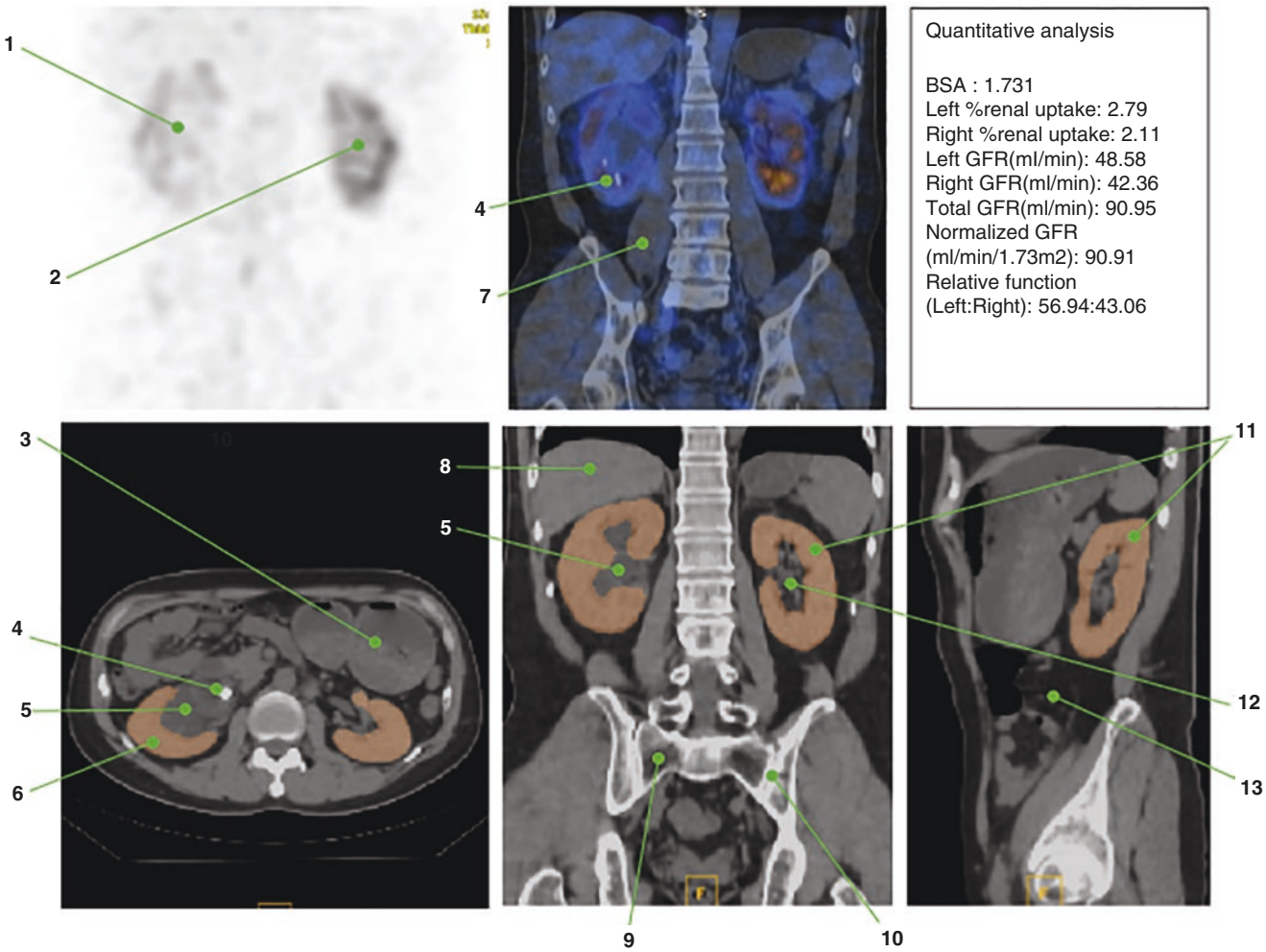

Fig. 78 1. Right kidney, decreased uptake
2. Left kidney, normal uptake
3. Stomach
4. Right renal pelvis stone
5. Right dilated renal pelvis: hydronephrosis
6. Right renal cortex, normal thickness
7. Right psoas muscle
8. Liver
9. Right sacral ala
10. Left sacroiliac joint
11. Left renal cortex
12. Left renal sinus
13. Descending colon

2.2.7.2. Case 2

A 72-year-old male patient with history of kidney transplant in 2015, who attended his annual checkup. ^{99m}Tc-DTPA and SPECT/CT were performed to find a normal functioning transplanted kidney with calculated GFR (ml/min) of 96.78. Native non-functioning kidneys showed atrophy in the right side and a large water bag kidney in the left side (Fig. 79).

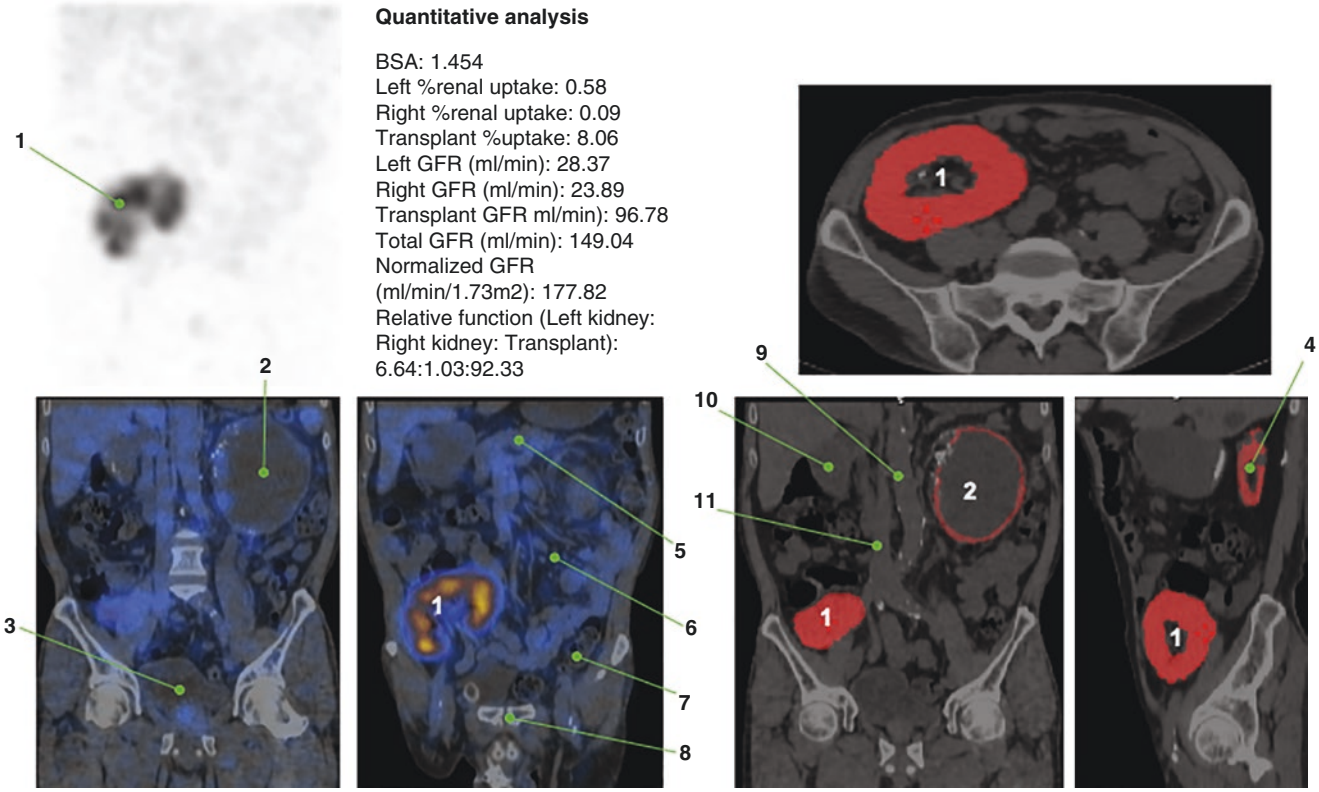

Fig. 79 1. Transplanted kidney in the right pelvis
2. Left, large, water bag kidney
3. Bladder
4. Atrophic right kidney
5. Pancreatic body
6. Small bowel mesentery
7. Distal descending colon
8. Pubic symphysis
9. Abdominal aorta
10. Gallbladder
11. Inferior vena cava

2.2.8 Lymphatic System

2.2.8.1. Case 1

A 44-year-old woman with a history of right breast cancer treated with total mastectomy and axillary lymph node dissection, who developed right arm lymphedema. ^{99m}Tc-ASC lymphoscintigraphy and SPECT/CT was performed and showed absence of main lymphatics in the right arm, as well as absence of lymph nodes and positive dermal backflow (DBF) until the elbow level. In the left arm, normal lymphatic vessels and lymph nodes were observed (Fig. 80).

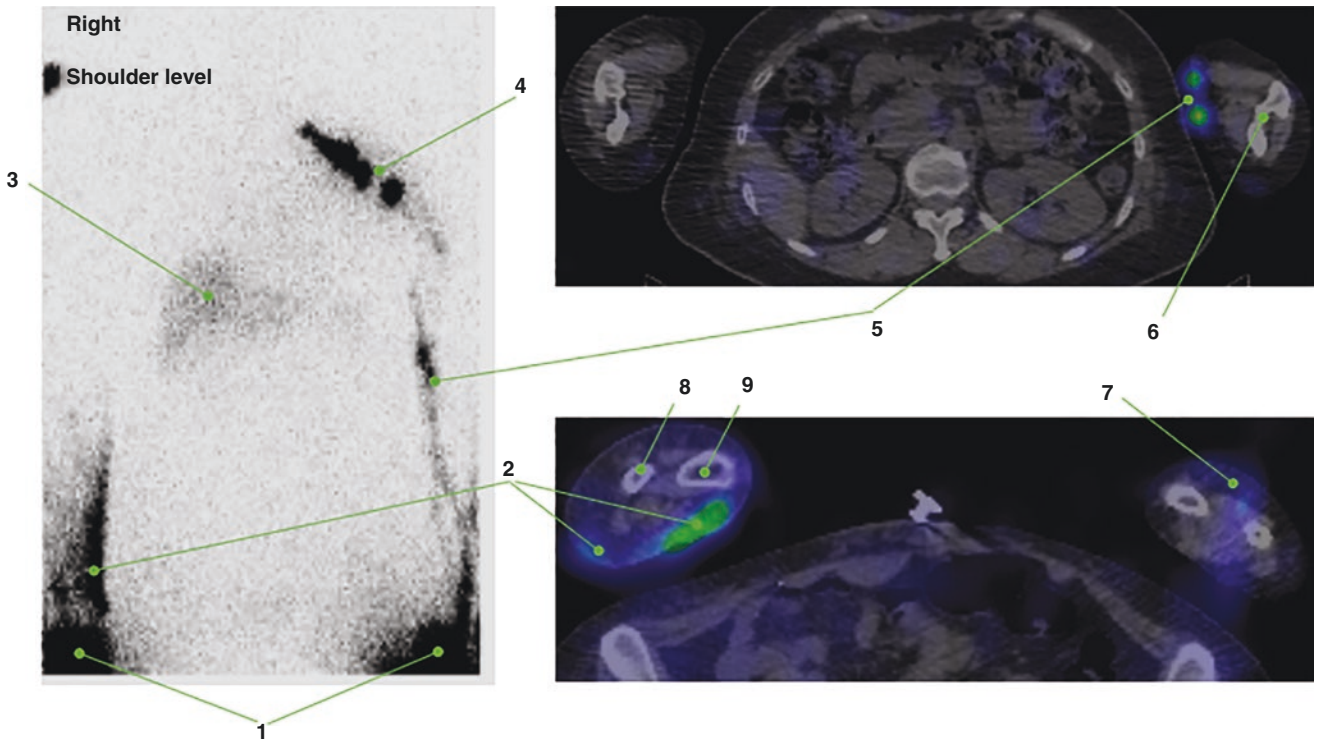

Fig. 80 1. Injection site at both hands
2. Dermal backflow in the right arm
3. Mild increased activity in the liver
4. Left axillary lymph nodes
5. Normal main lymphatics in the left arm
6. Left distal humerus
7. Left arm subcutaneous tissue, normal appearance
8. Right ulna
9. Right radius

2.2.8.2. Case 2

A 45-year-old male patient with confirmed diagnosis of left preauricular melanoma. Selected SPECT (*top*) and SPECT/CT (*bottom*) images of the neck, including the lower head, after intradermal injection of ^{99m}Tc filtered sulfur colloidal particles around the tumor, demonstrated focal areas of slightly increased activity in the left upper jugular lymphatic chain (level IIB), indicating sentinel lymph nodes. The sentinel lymph node is hypothetically the first lymph node or group of nodes to drain the cancer. It is postulated that sentinel lymph nodes are the target organs primarily reached by metastasizing cancer cells from the tumor. The spread of some forms of cancer usually follows an orderly progression (Fig. 81) [62].

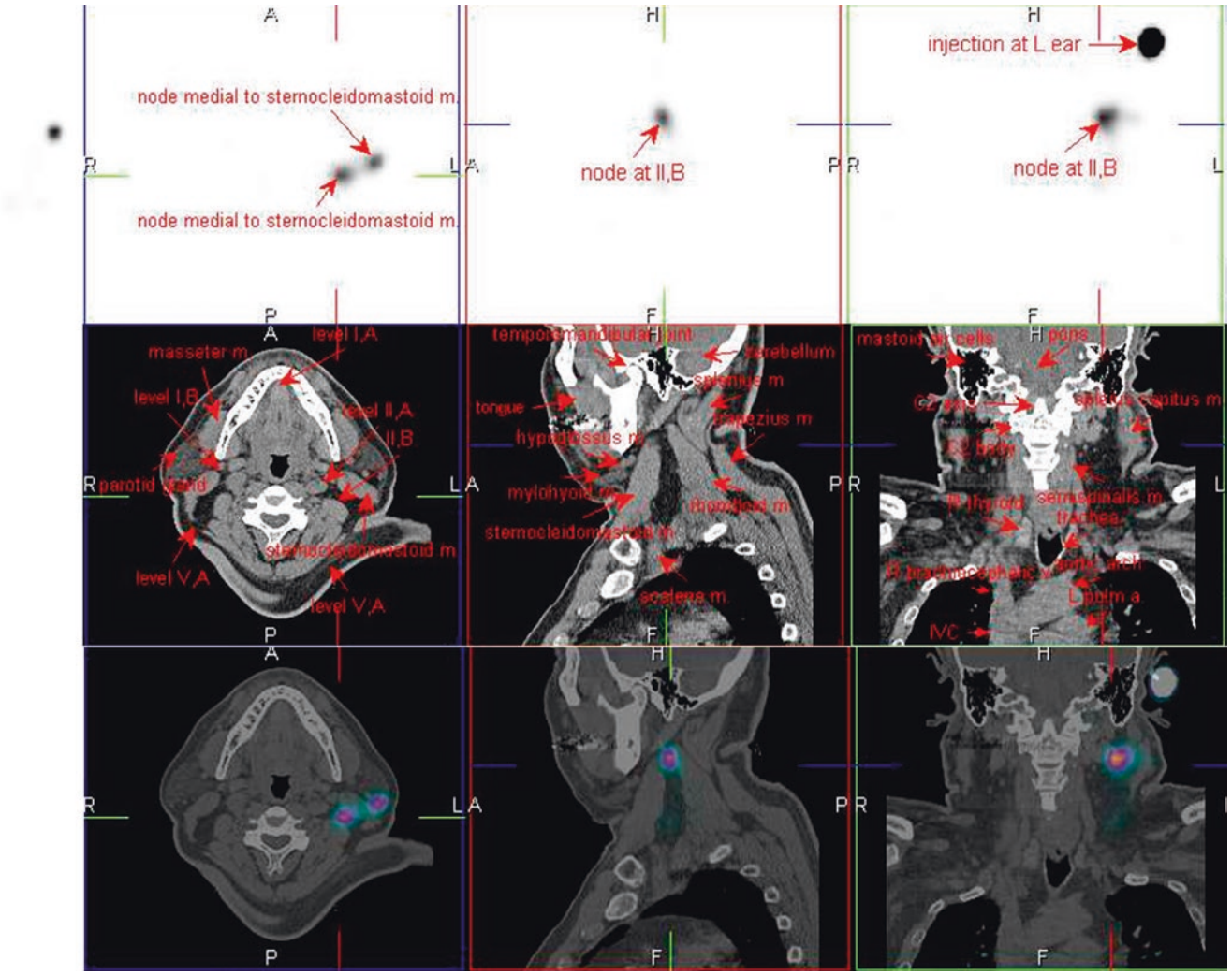

Fig. 81 ^{99m}Tc-filtered sulfur colloid SPECT/CT

2.2.8.3. Case 3

A 59-year-old female patient with uterine cervical cancer. SPECT (*top*) and SPECT/CT (*bottom*) images of the pelvis after subcutaneous injection of ^{99m}Tc-filtered sulfur colloid particles around the area were performed. Images showed moderate increased activity in the left external iliac lymph node and slightly increased activity in the left inguinal superficial lymph node, indicating sentinel lymph nodes (Fig. 82).

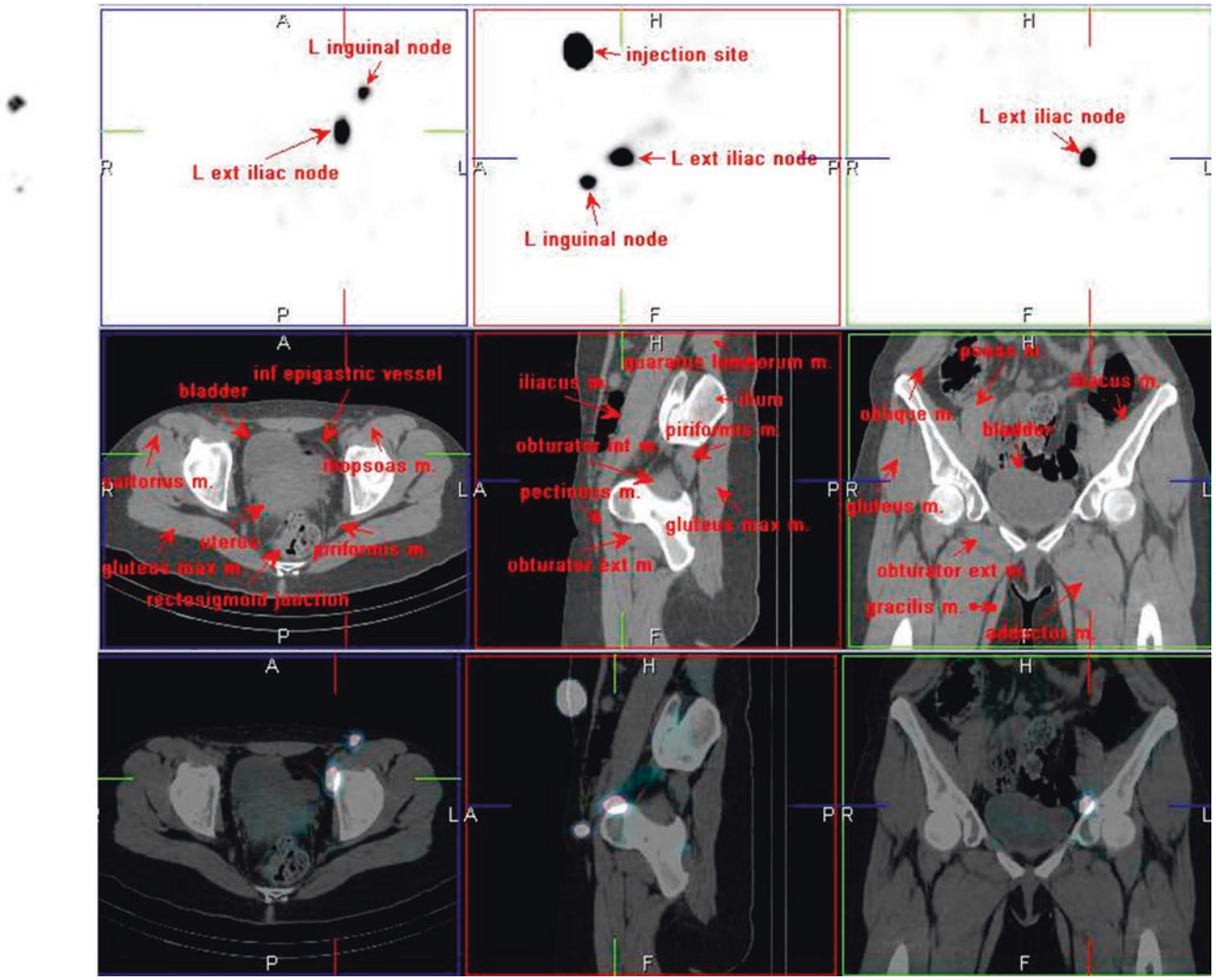

Fig. 82 ^{99m}Tc-filtered sulfur colloid SPECT/CT

2.2.8.4. Case 4

A 53-year-old female patient with recent diagnosis of melanoma in the right anterior chest wall. Selected SPECT (*top*) and SPECT/CT (*bottom*) images of the chest after intradermal injection of ^{99m}Tc-filtered sulfur colloid showed a focal area of slightly increased activity in the right superficial axillary lymph node (level I), indicating a sentinel lymph node (Fig. 83).

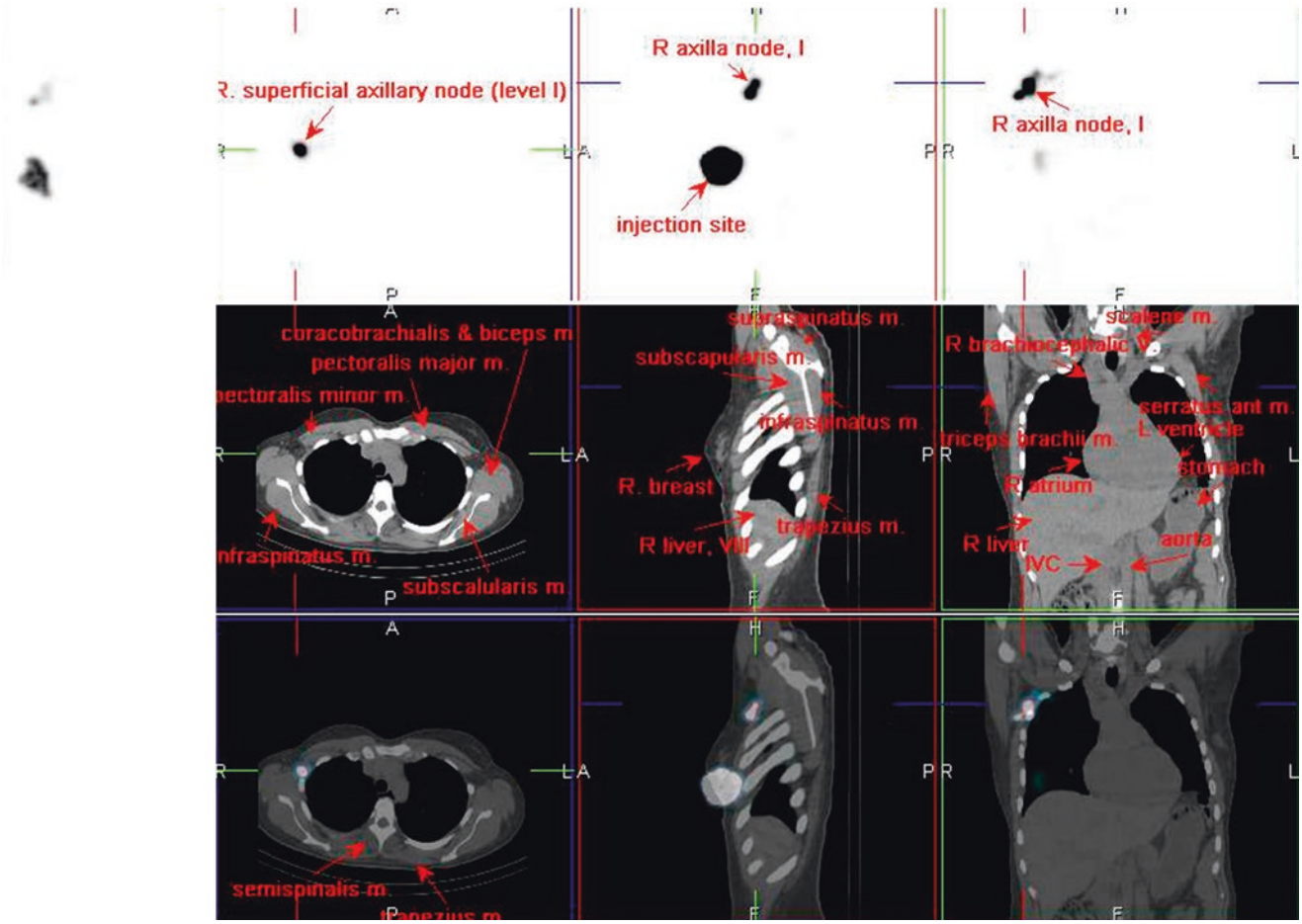

Fig. 83 ^{99m}Tc-filtered sulfur colloid SPECT/CT

2.2.8.5. Case 5

A 64-year-old male patient with a squamous cell carcinoma in the right tongue base. Selected SPECT *(top)* and SPECT/CT (*bottom*) images of the neck, including the lower head, after subcutaneous injection of ^{99m}Tc Lymphoseek showed a focal area of slightly increased activity in the right carotid space, indicating a sentinel lymph node. Lymphoseek is a radioactive diagnostic agent for lymphatic mapping and guiding sentinel lymph node biopsy (Fig. 84) [63].

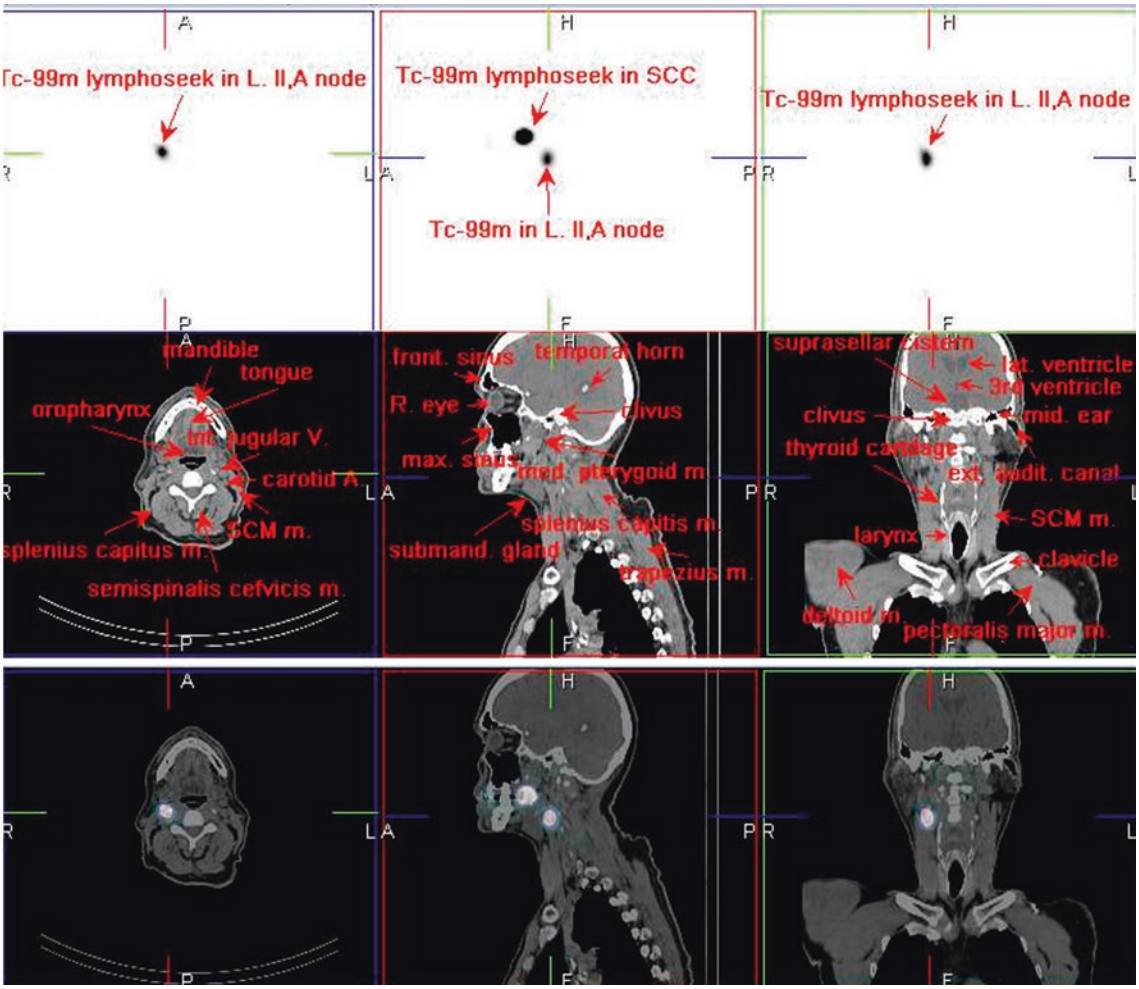

Fig. 84 ^{99m}Tc-lymphoseek SPECT/CT

2.2.9 Lung (V/Q)

2.2.9.1. Case 1

A 58-year-old male patient with non–small cell lung cancer, adenocarcinoma. ^{99m}Tc-MAA SPECT/CT was performed, finding a non-uniform distribution of the particles, indicating moderately decreased perfusion in the right upper, middle, and lower lobes. There was complete absence of particles within the tumor. ^{99m}Tc-MAA SPECT/CT is frequently performed for the presurgical evaluation of patients with lung cancer to determine the extent of surgery (Figs. 85, 86, and 87) [64, 65].

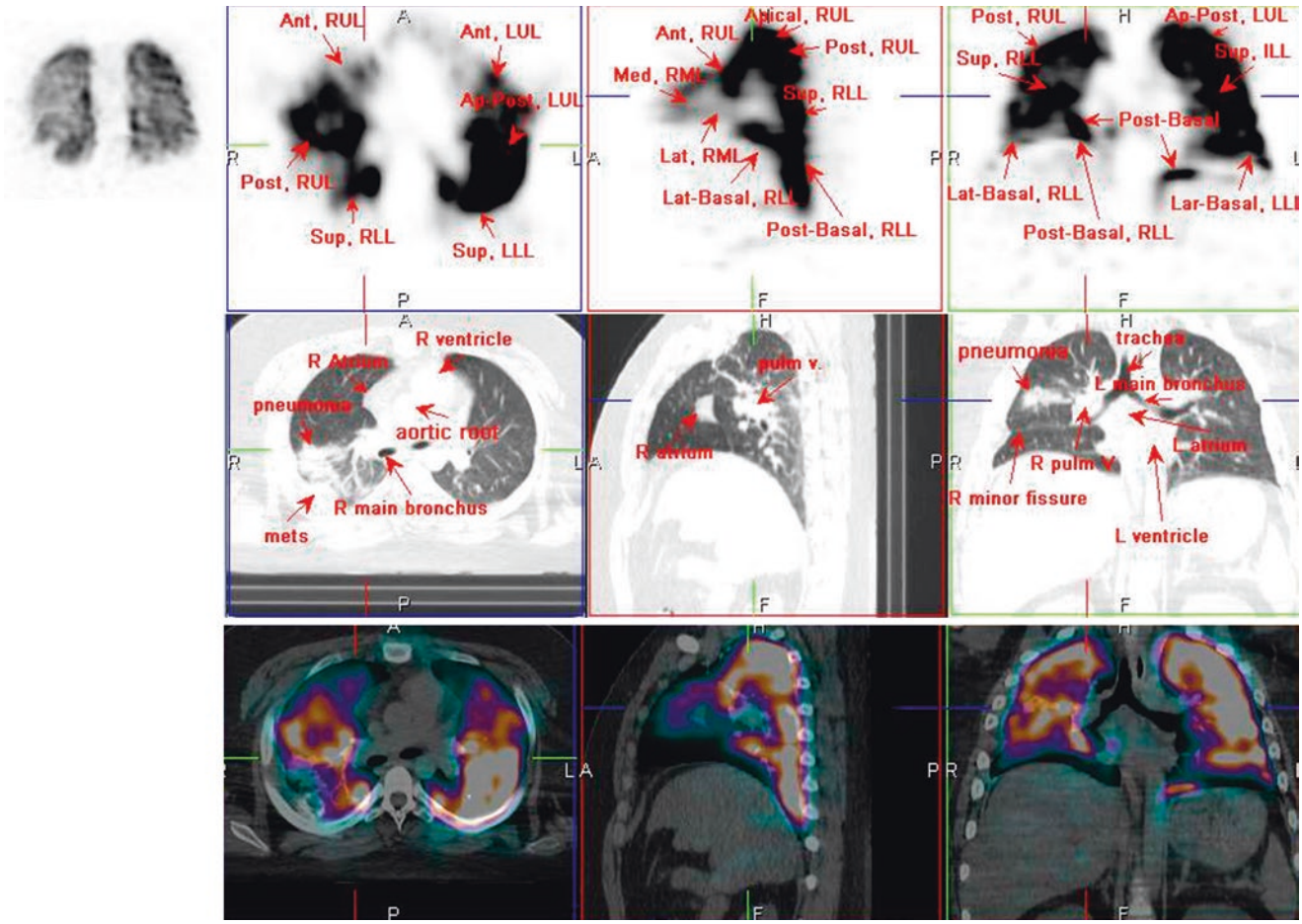

Fig. 85 ^{99m}Tc-MAA SPECT/CT

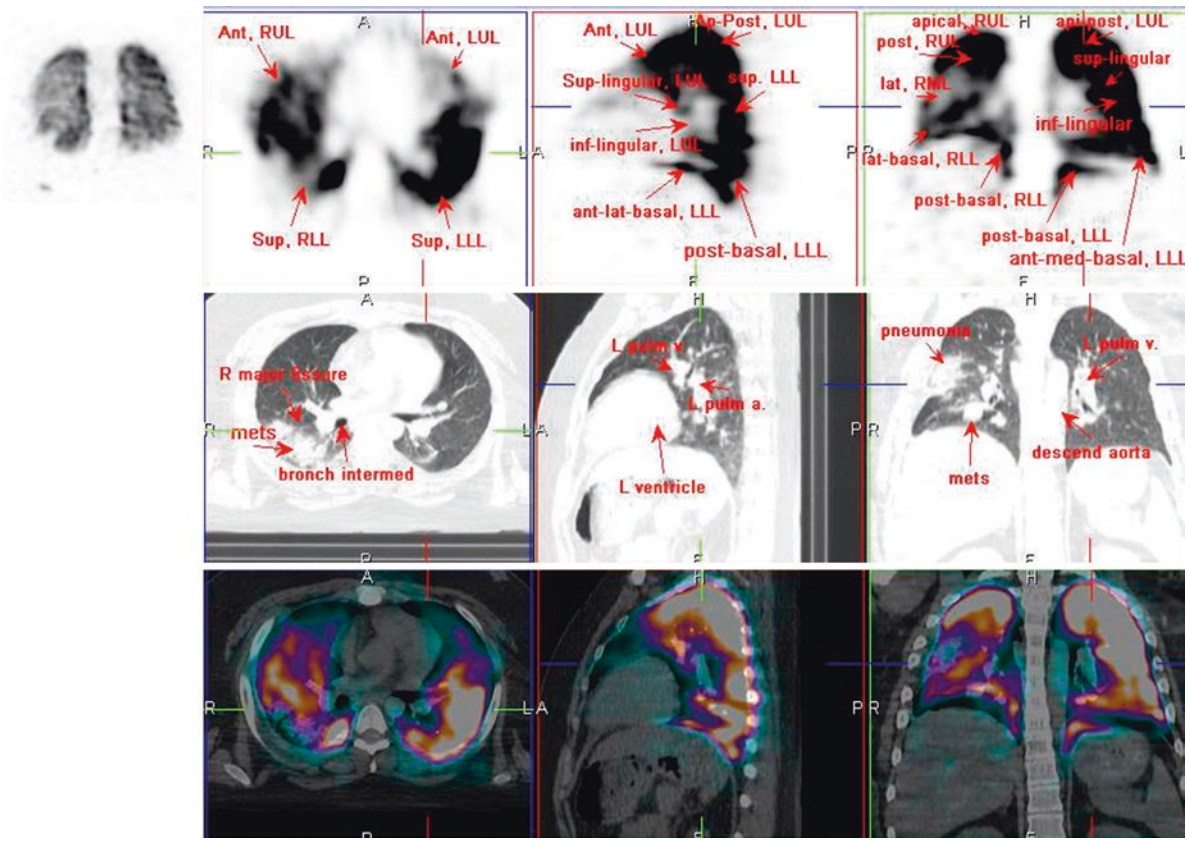

Fig. 86 ^{99m}Tc-MAA SPECT/CT

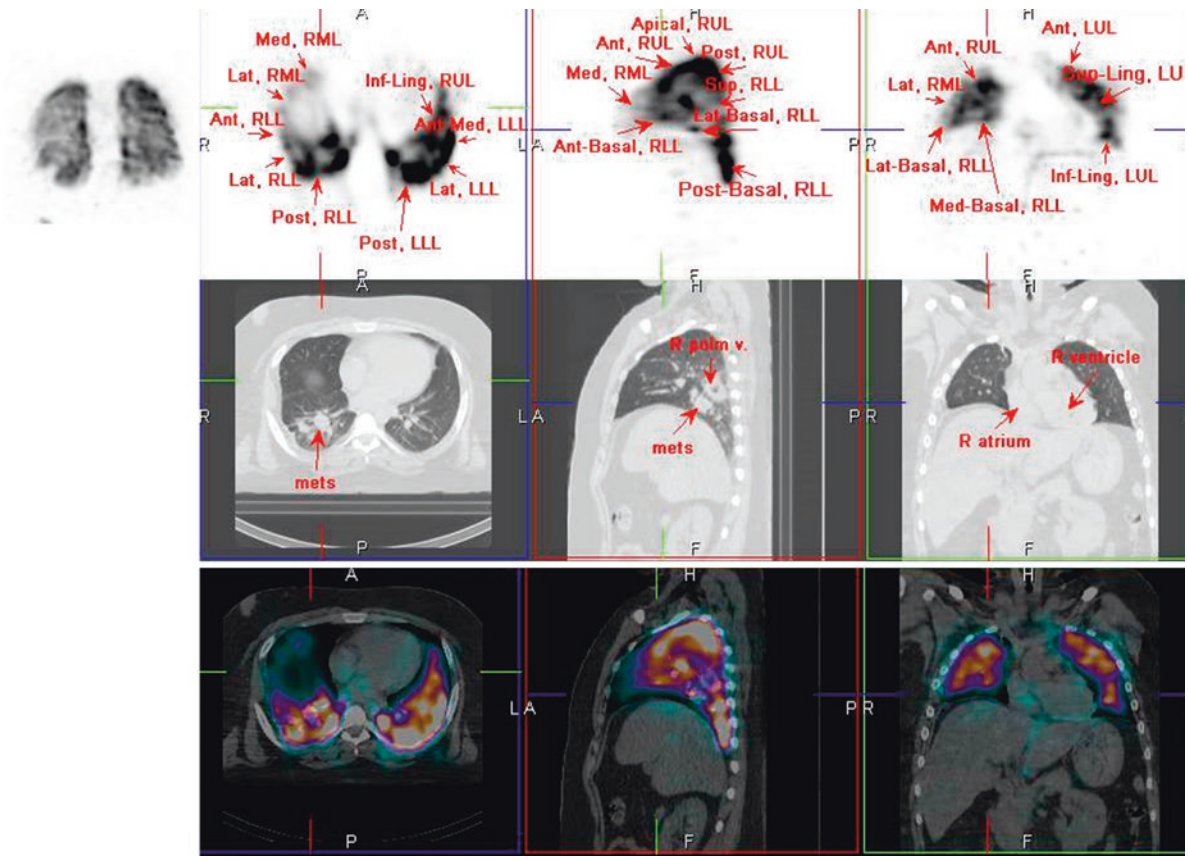

Fig. 87 ^{99m}Tc-MAA SPECT/CT

2.2.9.2. Case 2

A 26-year-old female patient with a history of recurrent respiratory papillomatosis, who developed a lung squamous cell carcinoma. Presurgical lung perfusion scan with SPECT/CT was performed to determine lung function and extent of surgery. Images showed a spiculated dense nodule in the right lower lobe, corresponding to the primary tumor, as well as complete perfusion defect in the whole lobe, probably due to obstruction (Fig. 88).

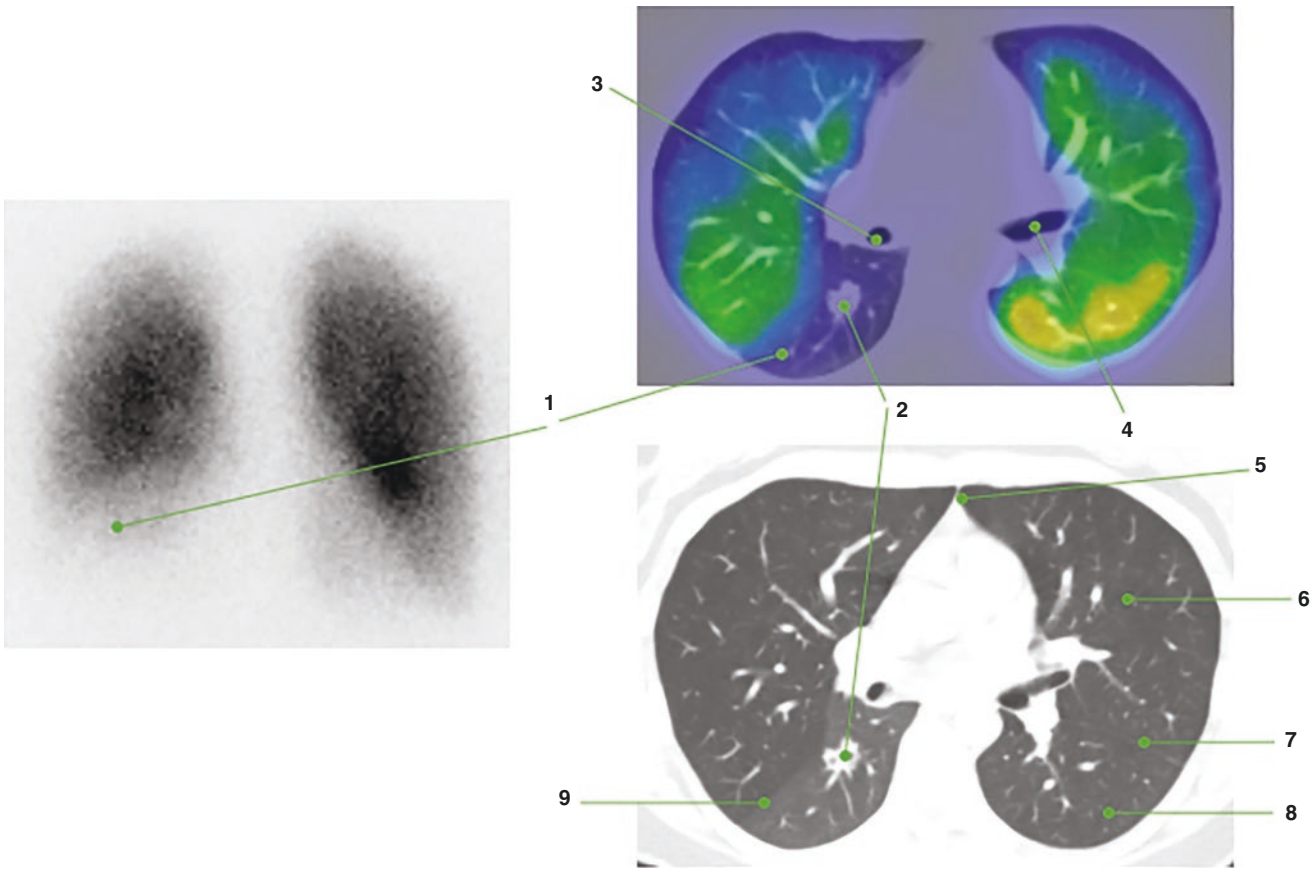

Fig. 88 1. Perfusion defect in the right lower lobe
2. Spiculated dense nodule in the right lower lobe: primary squamous cell carcinoma
3. Right main bronchus
4. Left main bronchus
5. Anterior junction line
6. Left upper lobe
7. Left major fissure
8. Left lower lobe
9. Right major fissure

2.2.10 Accessory Spleen

2.2.10.1. Case 1

A 50-year-old male patient attended a routine checkup and abdominal CT was performed finding an enhancing mass adjacent to the pancreatic tail. ^{99m}Tc-denatured RBC spleen scan was done for differential diagnosis, finding focal increased uptake in the nodular lesion at the pancreatic tail, which corresponded to an accessory spleen (Figs. 89, 90, 91, and 92) [66].

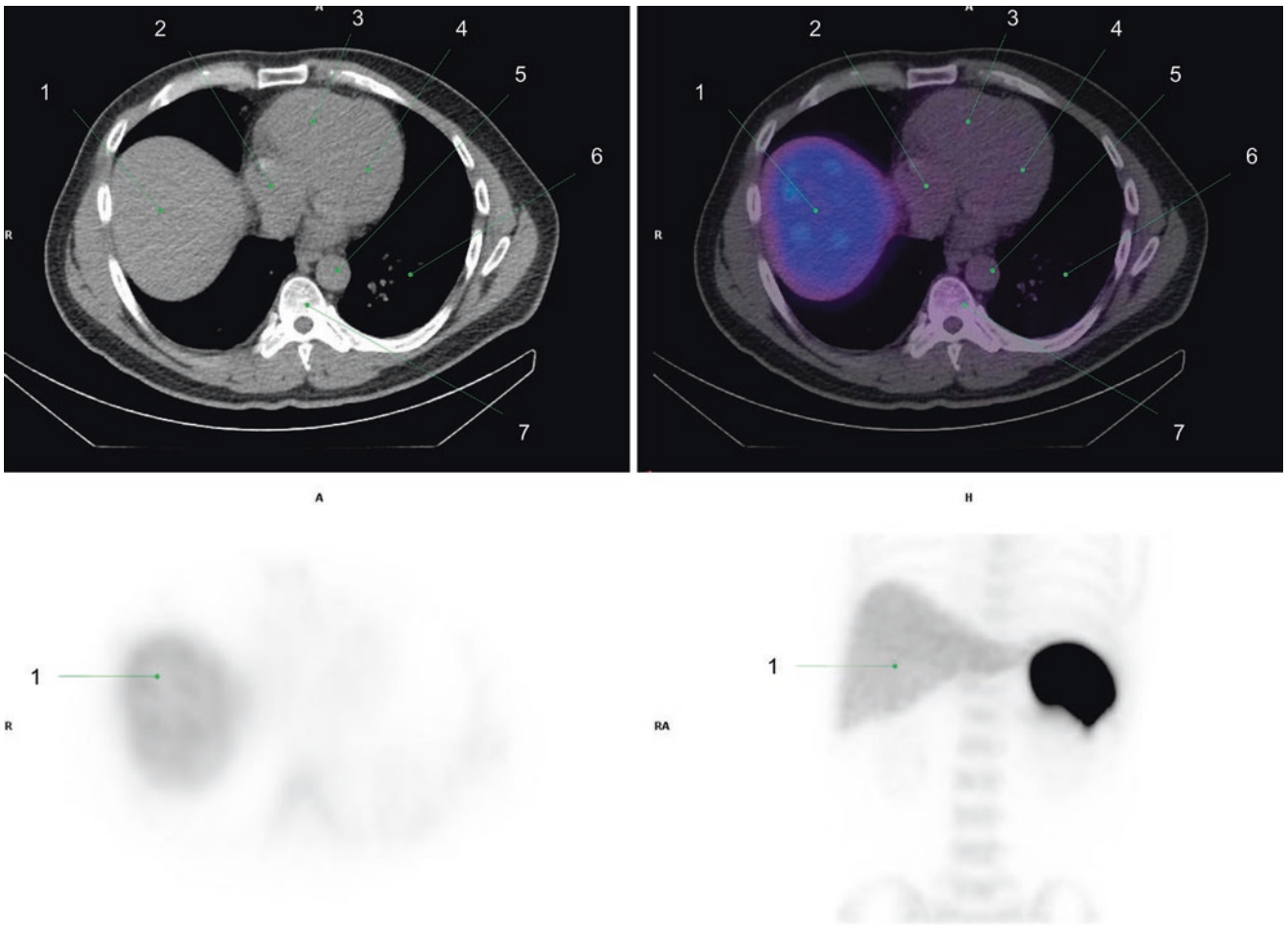

Fig. 89 1. Liver dome
2. Right atrium of the heart
3. Right ventricle
4. Left ventricle
5. Descending aorta
6. Lung parenchyma
7. Vertebral body

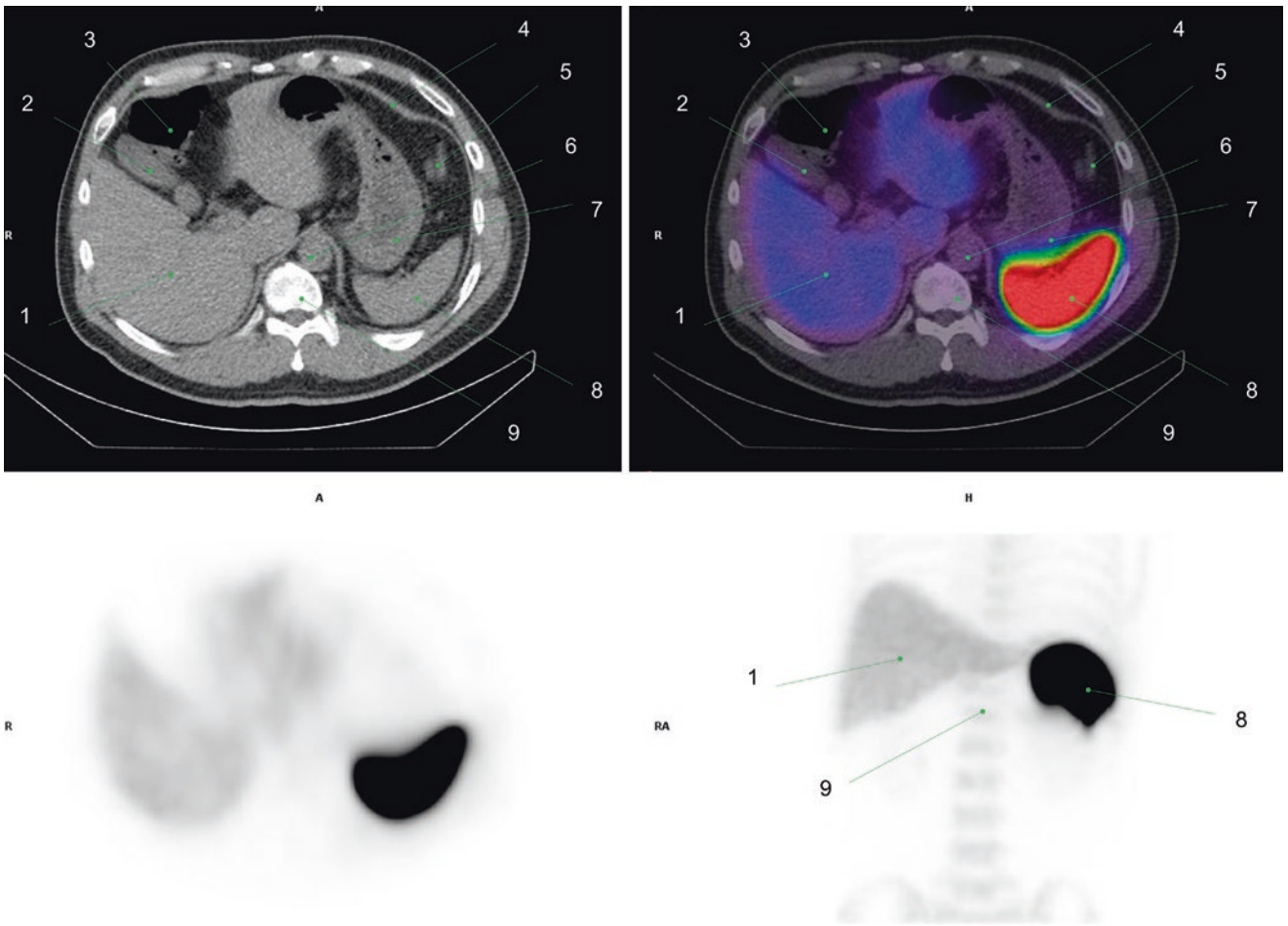

Fig. 90 1. Liver
2. Gallbladder
3. Hepatic flexure of transverse colon
4. Left diaphragm
5. Left gastroepiploic vessels
6. Spleen
7. Vertebral body

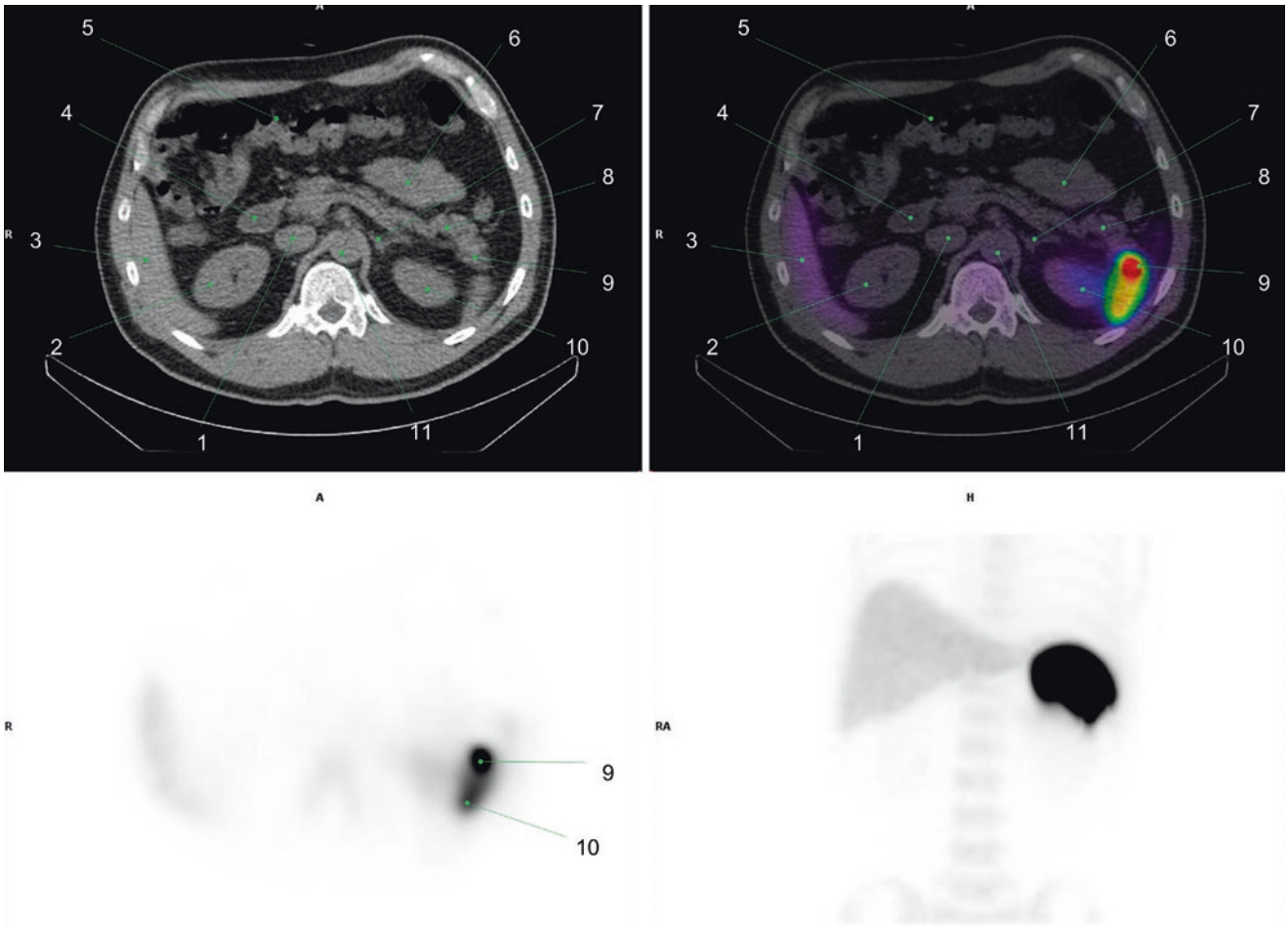

Fig. 91 1. Inferior vena cava
2. Right kidney
3. Liver tip
4. Second portion of duodenum
5. Transverse colon
6. Small bowels
7. Left adrenal gland
8. Tail of the pancreas
9. Intrapancreatic accessory spleen
10. Spleen
11. Descending aorta

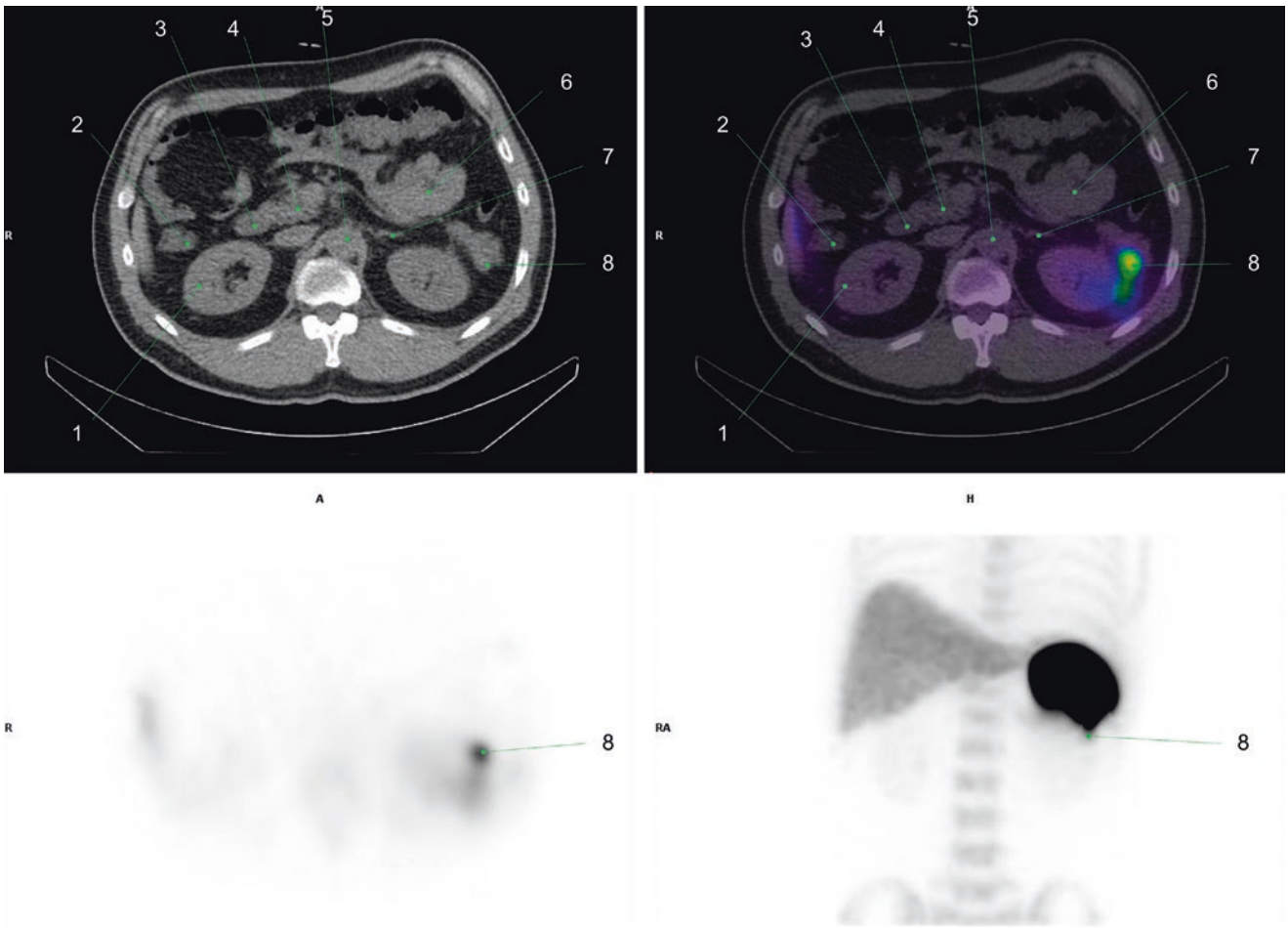

Fig. 92 1. Right kidney
2. Ascending colon
3. Duodenum
4. Uncinate process of the pancreas
5. Descending aorta
6. Small bowels
7. Left adrenal gland
8. Intrapancreatic accessory spleen

2.2.11 Adrenal Hyperplasia

2.2.11.1. Case 1

A 52-year-old male patient with right flank pain and abnormal adrenal function tests. So ^{123}I-MIBG SPECT/CT was performed for further evaluation. Images showed moderately increased activity in both adrenal glands, corresponding to adrenal hyperplasia. Also, a right renal mass was observed on CT, which was later confirmed to be a renal cell carcinoma (Fig. 93).

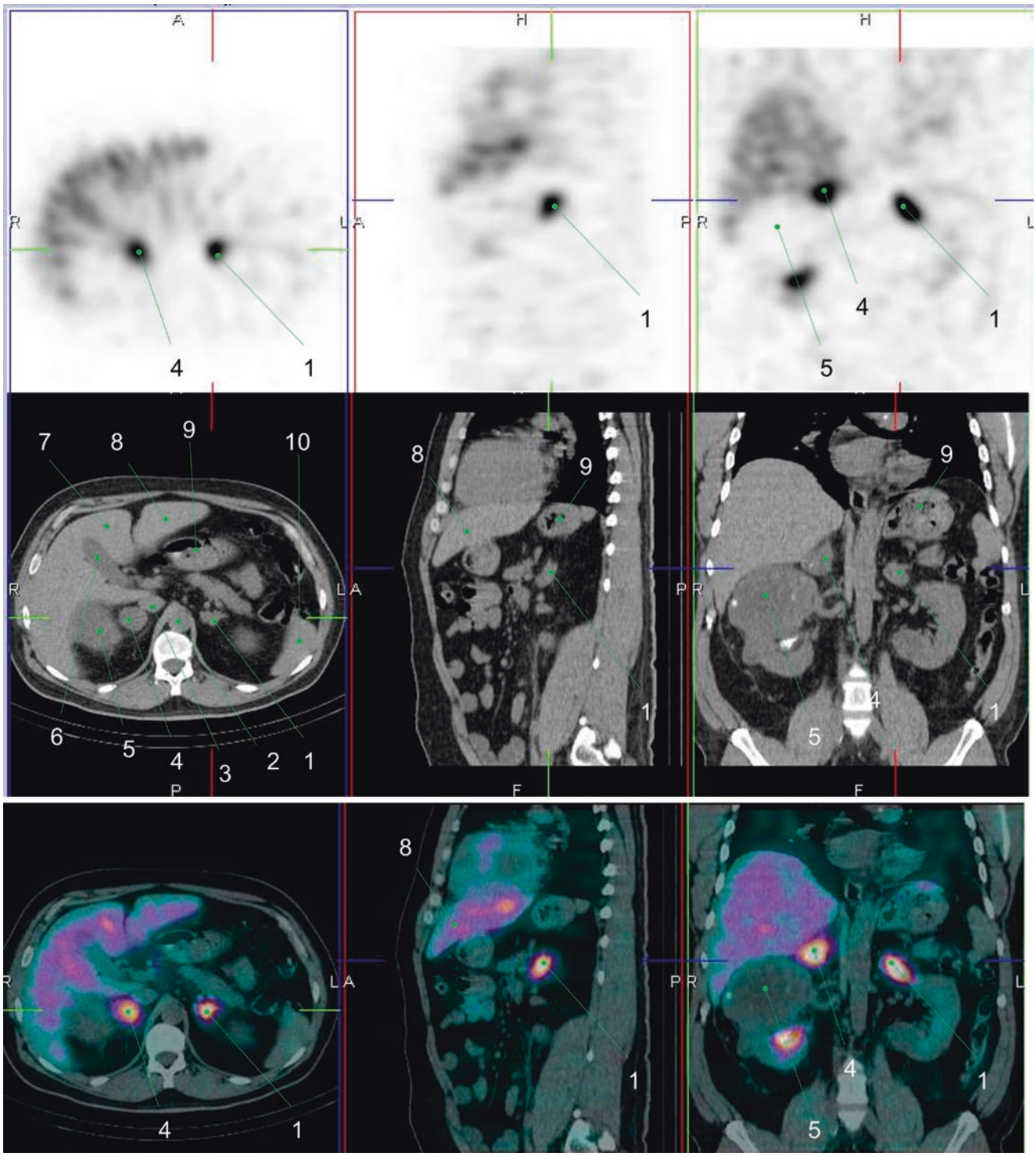

Fig. 93 1. Left adrenal gland hyperplasia
2. Abdominal aorta
3. Inferior vena cava
4. Right adrenal gland hyperplasia
5. Renal cell carcinoma in right kidney
6. Gallbladder
7. Liver, S4
8. Liver, left lobe
9. Stomach
10. Spleen

2.2.12 Heart

2.2.12.1. Case 1

An 84-year-old male patient with a history of asymptomatic coronary atherosclerosis, who attended a routine checkup and referred occasional chest pain. Laboratory studies were carried out finding increased troponin and proBNP, as well as increased free light chain of lambda and kappa (18.66 and 21.16, respectively). ^{99m}Tc-HMDP heart planar scan with SPECT/CT was performed and images showed significant heart uptake, which suggested transthyretin-related (TTR) amyloidosis, later confirmed with biopsy (Fig. 94) [67].

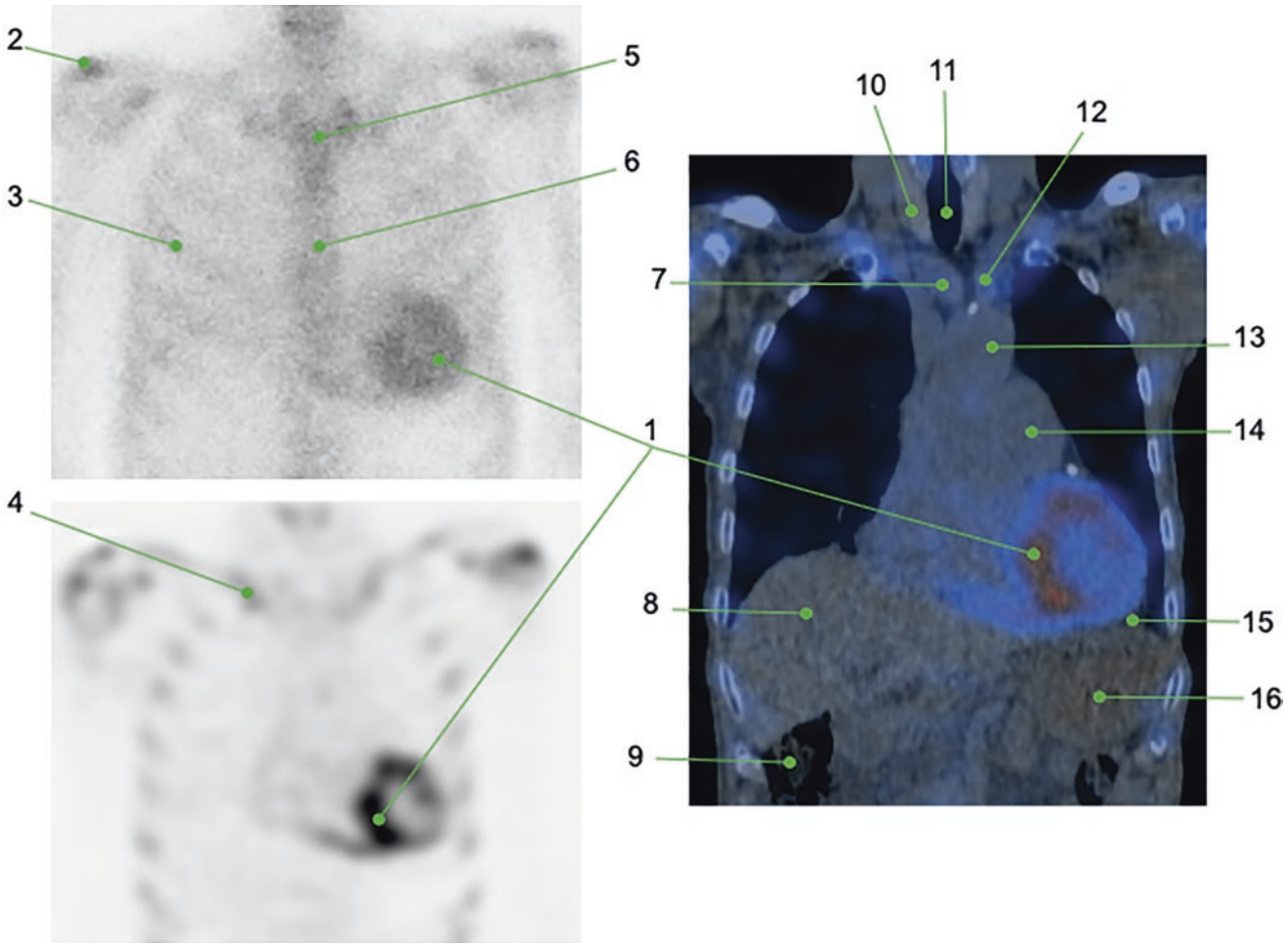

Fig. 94 1. Markedly increased uptake in the left ventricular wall: amyloidosis involvement
2. Focal increased uptake in the right acromioclavicular joint: degenerative changes
3. Right fourth rib anterior arc
4. Right sternoclavicular joint
5. Sternum manubrium
6. Sternum body
7. Right brachiocephalic artery
8. Liver
9. Hepatic angle of the colon
10. Right thyroid lobe
11. Trachea
12. Left common carotid artery
13. Aortic arch
14. Left atrium
15. Left cardio phrenic recess
16. Stomach

2.2.13 Brain

2.2.13.1. Case 1

A 35-year-old asymptomatic man with diagnosis of Moyamoya disease who attended a periodic checkup. ^{99m}Tc-HMPAO brain perfusion SPECT was performed. Basal study showed adequate perfusion in all vascular territories bilaterally. In post-acetazolamide study, perfusion is maintained and/or increased, which indicates that the vascular reserve is preserved. Anterior cerebral artery (ACA), middle cerebral artery (MCA), internal carotid artery (ICA = ACA + MCA), and posterior cerebral artery (PCA) (Fig. 95) [68].

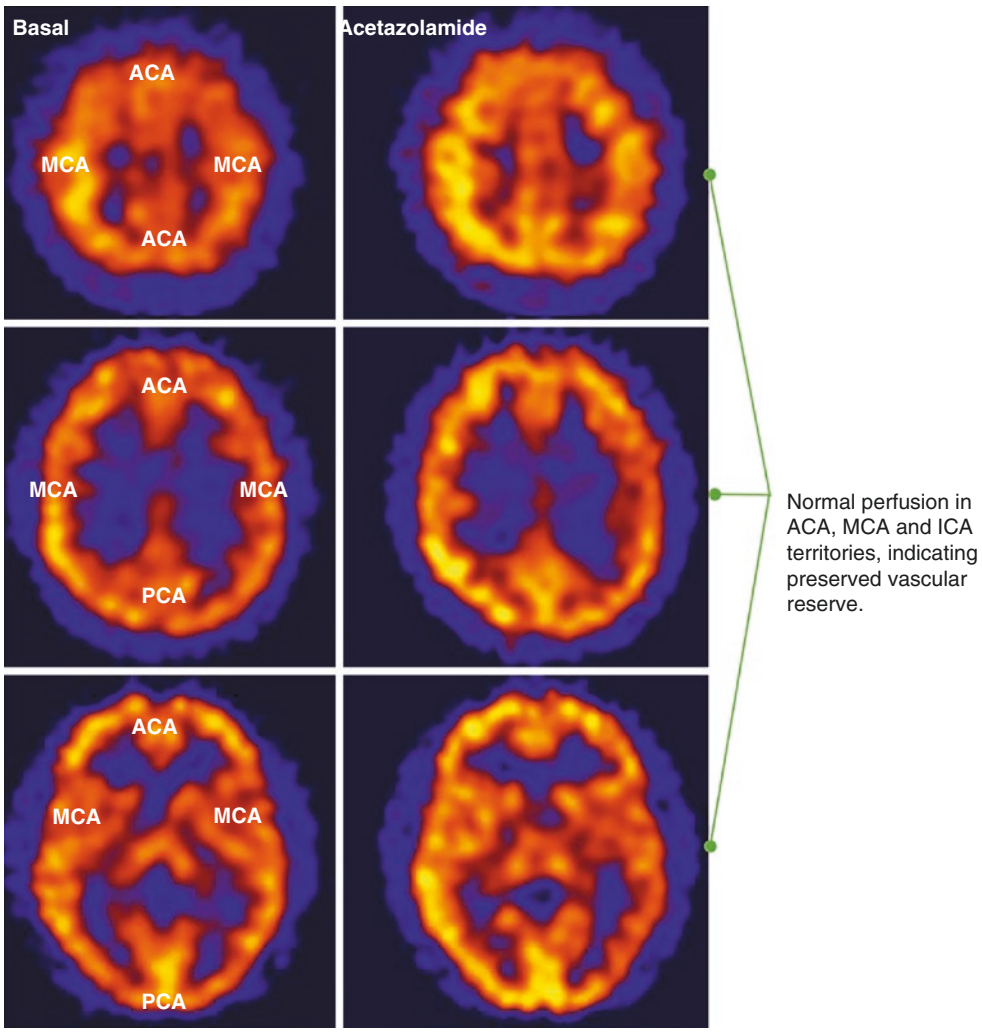

Fig. 95 ^{99m}Tc-HMPAO brain perfusion SPECT

2.2.13.2. Case 2

An 84-year-old woman with a diagnosis of severe atherosclerotic carotid stenosis of both extracranial internal carotid arteries. ^{99m}Tc-HMPAO brain perfusion SPECT was performed to determine if there was surgical indication. Basal study showed adequate perfusion in all territories. However, the post-acetazolamide study showed decreased perfusion in the left ICA (ACA + MCA) territory, indicating that the vascular reserve is compromised because the stenosis has progressed to the point of consuming compensatory capacity. These findings indicate that the patient would benefit from surgical intervention to prevent and/or reduce the risk of stroke (Fig. 96) [68].

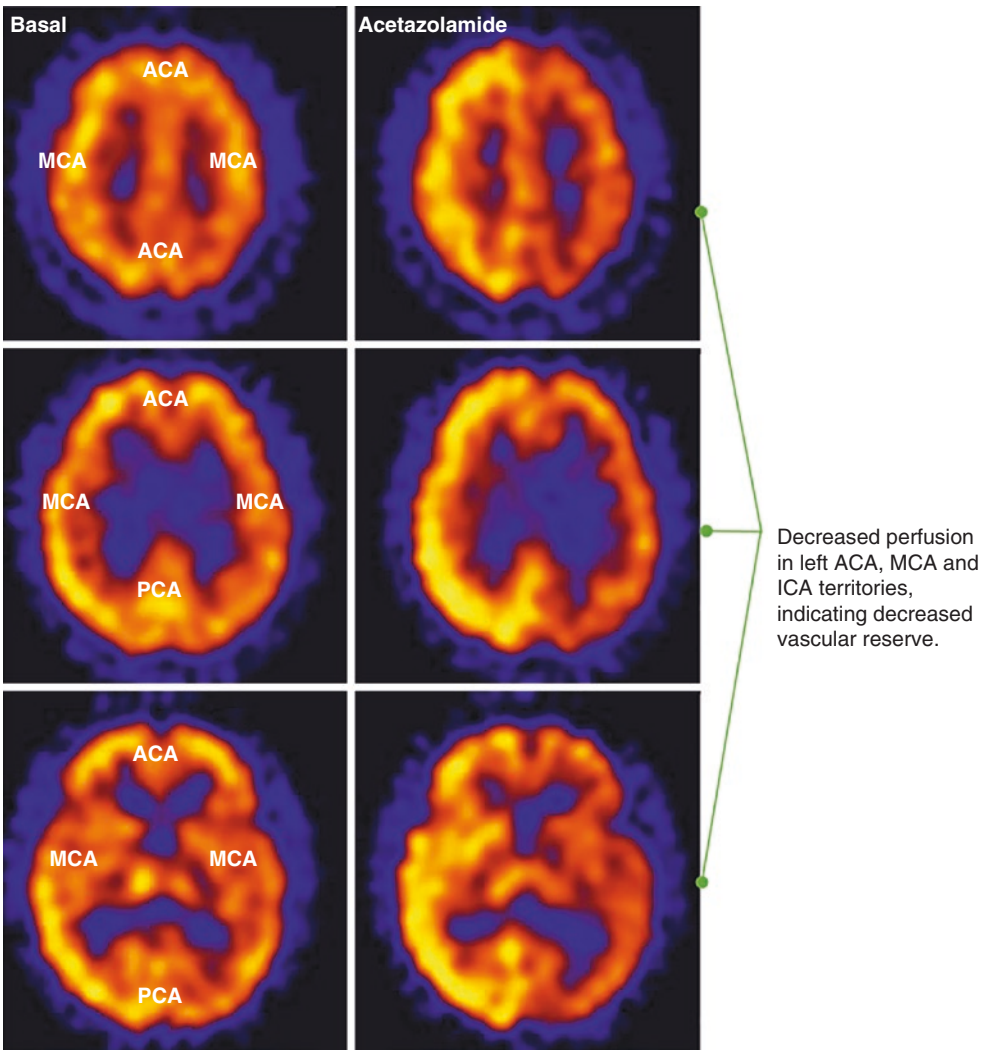

Fig. 96 ^{99m}Tc-HMPAO brain perfusion SPECT

Acknowledgments *The authors gratefully acknowledge Dr. Dong Soo Lee and Dr. Keon Wook Kang for their contributions to this chapter as it appeared in the previous edition.*

References

1. Van den Wyngaert T, Elvas F, De Schepper S, Kennedy JA, Israel O. SPECT / CT - standing on the shoulders of giants, it is time to reach for the sky! J Nucl Med. 2020:jnumed.119.236943.
2. Kinclab V, Drozdová A, Vašina J, Panovský R, Kamínek M. Cadmium – zinc – telluride SPECT scanners – new perspectives in nuclear cardiology. Cor Vasa. 2015;57(3):214–8.
3. Alenazy AB, Wells RG, Ruddy TD. New solid-state cadmium-zinc-telluride technology for cardiac single photon emission computed tomographic myocardial perfusion imaging. Expert Rev Med Devices. 2017;14(3):213–22.
4. Garcia TR, Kivenson A, Malonson S, Kudrolli H. Enhanced molecular breast image quality through improved CZT detector performance. IEEE Nuclear Science Symposium and Medical Imaging Conference (NSS / MIC) 2014, pp 1–3.
5. Mariani G, Bruselli L, Kuwert T, Kim EE, Flotats A, Israel O, et al. A review of clinical uses of SPECT / CT. Eur J Nucl Med Mol Imaging. 2010;37(10):1959–85.
6. Roarke MC, Nguyen BD, Pockaj BA. Applications of SPECT / CT in nuclear radiology. AJR. 2008;191:W135–50.
7. Ichikawa H, Miwa K, Okuda K, Shibutani T, Kato T, Nagaki A, et al. Current state of bone scintigraphy protocols and practice in Japan. Asia Oceania J Nucl Med Biol. 2020;8(2):116–22.
8. Kapoor M, Kasi A. Octreotide scan. In: StatPearls [Internet]. Treasure Island: StatPearls Publishing; 2021. 2021 Jan–. PMID: 32644756.
9. Donohoe KJ, Aloff J, Avram AM, Bennet KG, Giovanella L, Greenspan B. Appropriate use criteria for nuclear medicine in the evaluation and treatment of differentiated thyroid cancer. J Nucl Med. 2020;61(3):375–96.
10. Gandhi SJ, Babu S, Subramanyam P, Shanmuga Sundaram P. Tc-99m macro aggregated albumin scintigraphy - indications other than pulmonary embolism: a pictorial essay. Indian J Nucl Med. 2013;28(3):152–62.
11. Garin E, Rolland Y, Boucher E, Ardisson V, Laffont S, Boudjema K, et al. First experience of hepatic radioembolization using microspheres labelled with yttrium-90 (TheraSphere): practical aspects concerning its implementation. Eur J Nucl Med Mol Imaging. 2010;37(3):453–61.
12. Ahn BC. Macroaggregated albumin (MAA) injected in hepatic artery visualized in a recanalized paraumbilical vein. Clin Nucl Med. 2012;37(9):874.
13. Gulec SA, Mesoloras G, Dezarn WA, McNeillie P, Kennedy AS. Safety and efficacy of Y-90 microsphere treatment in patients with primary and metastatic liver cancer: the tumor selectivity of the treatment as a function of tumor to liver flow ratio. J Transl Med. 2007;5:15.
14. Panzuto F, Boninsegna L, Fazio N, Campana D, Pia Brizzi M, Capurso G, et al. Metastatic and locally advanced pancreatic endocrine carcinomas: analysis of factors associated with disease progression. J Clin Oncol. 2011;29(17):2372–7.
15. Berglund AS, Hulthen UL, Manheim P, Thorsson O, Wollmer P, Tornquist C. Metaiodobenzylguanidine (MIBG) scintigraphy and computed tomography (CT) in clinical practice. Primary and secondary evaluation for localization of pheochromocytomas. J Intern Med. 2001;249(3):247–51.
16. Lebtahi R, Le Cloirec J, Houzard C, Daou D, Sobhani I, Sassolas G, et al. Detection of neuroendocrine tumors: 99mTc-P829 scintigraphy compared with 111In-pentetreotide scintigraphy. J Nucl Med. 2002;43(7):889–95.
17. Zini L, Porpiglia F, Fassnacht M. Contemporary management of adrenocortical carcinoma. Eur Urol. 2011;60(5):1055–65.
18. Rufini V, Calcagni ML, Baum RP. Imaging of neuroendocrine tumors. Semin Nucl Med. 2006;36(3):228–47.
19. Bushnell DL, Baum RP. Standard imaging techniques for neuroendocrine tumors. Endocrinol Metab Clin N Am. 2011;40(1):153–62, ix.
20. Bombardieri E, Ambrosini V, Aktolun C, Baum RP, Bischof-Delaloye A, Del Vecchio S, et al. 111In-pentetreotide scintigraphy: procedure guidelines for tumour imaging. Eur J Nucl Med Mol Imaging. 2010;37(7):1441–8.
21. Pepe G, Moncayo R, Bombardieri E, Chiti A. Somatostatin receptor SPECT. Eur J Nucl Med Mol Imaging. 2012;39(Suppl 1):S41–51.
22. Ilias I, Divgi C, Pacak K. Current role of metaiodobenzylguanidine in the diagnosis of pheochromocytoma and medullary thyroid cancer. Semin Nucl Med. 2011;41(5):364–8.
23. van der Harst E, de Herder WW, Bruining HA, Bonjer HJ, de Krijger RR, Lamberts SW, et al. [(123)I]metaiodobenzylguanidine and [(111)In]octreotide uptake in benign and malignant pheochromocytomas. J Clin Endocrinol Metab. 2001;86(2):685–93.
24. Bombardieri E, Giammarile F, Aktolun C, Baum RP, Bischof Delaloye A, Maffioli L, et al. 131I/123I-metaiodobenzylguanidine (mIBG) scintigraphy: procedure guidelines for tumour imaging. Eur J Nucl Med Mol Imaging. 2010;37(12):2436–46.
25. Perri M, Erba P, Volterrani D, Lazzeri E, Boni G, Grosso M, et al. Octreo-SPECT/CT imaging for accurate detection and localization of suspected neuroendocrine tumors. Q J Nucl Med Mol Imaging. 2008;52(4):323–33.
26. Wong KK, Wynn EA, Myles J, Ackermann RJ, Frey KA, Avram AM. Comparison of single time-point [111-In] pentetreotide SPECT/CT with dual time-point imaging of neuroendocrine tumors. Clin Nucl Med. 2011;36(1):25–31.
27. Klimstra DS, Modlin IR, Coppola D, Lloyd RV, Suster S. The pathologic classification of neuroendocrine tumors: a review of nomenclature, grading, and staging systems. Pancreas. 2010;39(6):707–12.
28. Oberg K, Castellano D. Current knowledge on diagnosis and staging of neuroendocrine tumors. Cancer Metastasis Rev. 2011;30(Suppl 1):3–7.
29. Rufini V, Treglia G, Castaldi P, Perotti G, Calcagni ML, Corsello SM, et al. Comparison of 123I-MIBG SPECT-CT and 18F-DOPA PET-CT in the evaluation of patients with known or suspected recurrent paraganglioma. Nucl Med Commun. 2011;32(7):575–82.
30. Maroun J, Kocha W, Kvols L, Bjarnason G, Chen E, Germond C, et al. Guidelines for the diagnosis and management of carcinoid tumours. Part 1: the gastrointestinal tract. A statement from a Canadian National Carcinoid Expert Group. Curr Oncol. 2006;13(2):67–76.
31. Modlin IM, Oberg K, Chung DC, Jensen RT, de Herder WW, Thakker RV, et al. Gastroenteropancreatic neuroendocrine tumours. Lancet Oncol. 2008;9(1):61–72.
32. Gustafsson BI, Kidd M, Chan A, Malfertheiner MV, Modlin IM. Bronchopulmonary neuroendocrine tumors. Cancer. 2008;113(1):5–21.
33. Tan EH, Tan CH. Imaging of gastroenteropancreatic neuroendocrine tumors. World J Clin Oncol. 2011;2(1):28–43.
34. Kaemmerer D, Posorski N, von Eggeling F, Ernst G, Horsch D, Baum RP, et al. The search for the primary tumor in metastasized gastroenteropancreatic neuroendocrine neoplasm. Clin Exp Metastasis. 2014;31(7):817–27.
35. Elaini AB, Shetty SK, Chapman VM, Sahani DV, Boland GW, Sweeney AT, et al. Improved detection and characterization of adrenal disease with PET-CT. Radiographics. 2007;27(3):755–67.

36. McNicol AM. Update on tumours of the adrenal cortex, pheochromocytoma and extra-adrenal paraganglioma. Histopathology. 2011;58(2):155–68.
37. Jeong SY, Lee SW, Kim HW, Song BI, Ahn BC, Lee J. Clinical applications of SPECT/CT after first I-131 ablation in patients with differentiated thyroid cancer. Clin Endocrinol. 2014;81(3):445–51.
38. Yamamoto Y, Nishiyama Y, Monden T, Matsumura Y, Satoh K, Ohkawa M. Clinical usefulness of fusion of 131I SPECT and CT images in patients with differentiated thyroid carcinoma. J Nucl Med. 2003;44(12):1905–10.
39. Griggs WS, Divgi C. Radioiodine imaging and treatment in thyroid disorders. Neuroimaging Clin N Am. 2008;18(3):505–15.
40. Gayed IW, Kim EE, Broussard WF, Evans D, Lee J, Broemeling LD, et al. The value of 99mTc-sestamibi SPECT/CT over conventional SPECT in the evaluation of parathyroid adenomas or hyperplasia. J Nucl Med. 2005;46(2):248–52.
41. Im HJ, Lee IK, Paeng JC, Lee KE, Cheon GJ, Kang KW, et al. Functional evaluation of parathyroid adenoma using 99mTc-MIBI parathyroid SPECT/CT: correlation with functional markers and disease severity. Nucl Med Commun. 2014;35(6):649–54.
42. Mariani G, Gulec SA, Rubello D, Boni G, Puccini M, Pelizzo MR, et al. Preoperative localization and radioguided parathyroid surgery. J Nucl Med. 2003;44(9):1443–58.
43. Qureshi NR, Gleeson FV. Imaging of pleural disease. Clin Chest Med. 2006;27(2):193–213.
44. Sugarbaker DJ, Wolf AS. Surgery for malignant pleural mesothelioma. Expert Rev Respir Med. 2010;4(3):363–72.
45. Kendi AT, Kara S, Altinok D, Keskil S. Sinonasal ossifying fibroma with fluid-fluid levels on MR images. AJNR Am J Neuroradiol. 2003;24(8):1639–41.
46. Even-Sapir E, Metser U, Mishani E, Lievshitz G, Lehman H, Leibovitch I. The detection of bone metastases in patients with high-risk prostate cancer: 99mTc-MDP planar bone scintigraphy, single- and multi-field-of-view SPECT, 18F-fluoride PET, and 18F-fluoride PET/CT. J Nucl Med. 2006;47(2):287–97.
47. Maris JM, Hogarty MD, Bagatell R, Cohn SL. Neuroblastoma. Lancet. 2007;369(9579):2106–20.
48. Fish JD, Grupp SA. Stem cell transplantation for neuroblastoma. Bone Marrow Transplant. 2008;41(2):159–65.
49. Wertman M, Milgrom C, Agar G, Milgrom Y, Yalom N, Finestone AS. Comparison of knee SPECT and MRI in evaluating meniscus injuries in soldiers. Isr Med Assoc J. 2014;16(11):703–6.
50. Palestro CJ, Love C, Schneider R. The evolution of nuclear medicine and the musculoskeletal system. Radiol Clin N Am. 2009;47(3):505–32.
51. Van der Wall H, Lee A, Magee M, Frater C, Wijesinghe H, Kannangara S. Radionuclide bone scintigraphy in sports injuries. Semin Nucl Med. 2010;40(1):16–30.
52. Grant FD, Fahey FH, Packard AB, Davis RT, Alavi A, Treves ST. Skeletal PET with 18F-fluoride: applying new technology to an old tracer. J Nucl Med. 2008;49(1):68–78.
53. Huellner MW, Strobel K. Clinical applications of SPECT/CT in imaging the extremities. Eur J Nucl Med Mol Imaging. 2014;41(Suppl 1):S50–8.
54. Ryan PJ, Evans PA, Gibson T, Fogelman I. Chronic low back pain: comparison of bone SPECT with radiography and CT. Radiology. 1992;182(3):849–54.
55. DiGiovanni CW, Patel A, Calfee R, Nickisch F. Osteonecrosis in the foot. J Am Acad Orthop Surg. 2007;15(4):208–17.
56. Bentley DE, Richardson JD. The role of tagged red blood cell imaging in the localization of gastrointestinal bleeding. Arch Surg. 1991;126(7):821–4.
57. Howarth DM. The role of nuclear medicine in the detection of acute gastrointestinal bleeding. Semin Nucl Med. 2006;36(2):133–46.
58. Leder KS, Barlam TF. A case of paraspinal abscess and discitis due to Peptostreptococcus micros. Clin Infect Dis. 2000;30(3):622–3.
59. Ibrahim NA, Fadeyibi IO. Ectopic thyroid: etiology, pathology and management. Hormones (Athens). 2011;10(4):261–9.
60. Marmarou A, Young HF, Aygok GA. Estimated incidence of normal pressure hydrocephalus and shunt outcome in patients residing in assisted-living and extended-care facilities. Neurosurg Focus. 2007;22(4):E1.
61. Joffe HV, Goldhaber SZ. Upper-extremity deep vein thrombosis. Circulation. 2002;106(14):1874–80.
62. Leijte JA, Valdes Olmos RA, Nieweg OE, Horenblas S. Anatomical mapping of lymphatic drainage in penile carcinoma with SPECT-CT: implications for the extent of inguinal lymph node dissection. Eur Urol. 2008;54(4):885–90.
63. Sondak VK, King DW, Zager JS, Schneebaum S, Kim J, Leong SP, et al. Combined analysis of phase III trials evaluating [(99)mTc] tilmanocept and vital blue dye for identification of sentinel lymph nodes in clinically node-negative cutaneous melanoma. Ann Surg Oncol. 2013;20(2):680–8.
64. Hartman TE. Radiologic evaluation of the solitary pulmonary nodule. Radiol Clin N Am. 2005;43(3):459–65.
65. Kligerman SJ, Groshong S, Brown KK, Lynch DA. Nonspecific interstitial pneumonia: radiologic, clinical, and pathologic considerations. Radiographics. 2009;29(1):73–87.
66. Kim SH, Lee JM, Han JK, Lee JY, Kim KW, Cho KC, et al. Intrapancreatic accessory spleen: findings on MR imaging, CT, US and scintigraphy, and the pathologic analysis. Korean J Radiol. 2008;9(2):162–74.
67. Li W, Uppal D, Wang YC, et al. Nuclear imaging for the diagnosis of cardiac amyloidosis in 2021. Diagnostics (Basel). 2021;11(6):996.
68. Wong TH, Shagera QA, Ryoo HG, Ha S, Lee DS. Basal and acetazolamide brain perfusion SPECT in internal carotid artery stenosis. Nucl Med Mol Imaging. 2020;54(1):9–27.